Advanced methods for 3-D forest characterization and mapping from lidar remote sensing data

A Dissertation
Presented in Partial Fulfillment of the Requirements for the
Degree of Doctorate of Philosophy
with a
Major in Natural Resources
in the
College of Graduate Studies
University of Idaho
by

Carlos Alberto Silva

Major Professor: Lee A. Vierling, Ph.D.
Committee Members: Andrew T. Hudak, Ph.D.; Jan U.H. Eitel, Ph.D.;
Nicholas Crookston, M.Sc., Hon.D.; Luigi Boschetti, Ph.D.; Michael Keller, Ph.D.
Department Administrator: Lee A. Vierling, Ph.D.

May 2018

Authorization to Submit Dissertation

This dissertation of Carlos Alberto Silva, submitted for the degree of Doctorate of Philosophy with a Major in Natural Resources and titled "Advanced methods for 3-D forest characterization and mapping from lidar remote sensing data," has been reviewed in final form. Permission, as indicated by the signatures and dates below, is now granted to submit final copies to the College of Graduate Studies for approval

Major Professor: _____ Date:_____
Lee A. Vierling, Ph.D.

Committee Members: _____ Date:_____
Andrew T. Hudak, Ph.D.

_____ Date:_____
Jan U.H. Eitel, Ph.D.

_____ Date:_____
Nicholas Crookston, M.Sc., Hon.D.

_____ Date:_____
Luigi Boschetti, Ph.D.

_____ Date:_____
Michael Keller, Ph.D.

Department _____ Date:_____
Administrator: Lee A. Vierling, Ph.D.

Abstract

Accurate and spatially explicit measurements of forest attributes are critical for sustainable forest management and for ecological and environmental protection. Airborne Light Detection and Ranging (lidar) systems have become the dominant remote sensing technique for forest inventory, mainly because this technology can quickly provide highly accurate and spatially detailed information about forest attributes across entire landscapes. This dissertation is focused on developing and assessing novel and advanced methods for three dimensional (3-D) forest characterization. Specifically, I map canopy structural attributes of individual trees, as well as forests at the plot and landscape levels in both natural and industrial plantation forests using lidar remote sensing data.

Chapter 1 develops a novel framework to automatically detect individual trees and evaluates the efficacy of *k*-nearest neighbor (*k*-NN) imputation models for estimating tree attributes in longleaf pine (*Pinus palustris* Mill.) forests. Although basal area estimation accuracy was poor because of the longleaf pine growth habit, individual tree locations, height and volume were estimated with high accuracy, especially in low-canopy-cover conditions. The root mean square distance (RMSD) for tree-level height, basal area, and volume were 2.96%, 58.62%, and 8.19%, respectively.

Chapter 2 presents a methodology for predicting stem total and assortment volumes in industrial loblolly pine (*Pinus taeda* L.) forest plantations using lidar data as inputs to random forest models. When compared to reference forest inventory data, the accuracy of plot-level forest total and assortment volumes was high; the root mean square error (RMSE) of total, commercial and pulp volume estimates were 7.83%, 7.71% and 8.63%, respectively.

Chapter 3 evaluates the impacts of airborne lidar pulse density on estimating aboveground biomass (AGB) stocks and changes in a selectively logged tropical forest. Estimates of AGB change at the plot level were only slightly affected by pulse density. However, at the landscape level we observed differences in estimated AGB change of >20 $Mg \cdot ha^{-1}$ when pulse density decreased from 12 to 0.2 $pulses \cdot m^{-2}$. The effects of pulse density were more pronounced in areas of steep slope, but when the DTM from high pulse

density in 2014 was used to derive the forest height from both years, the effects on forest height and subsequent AGB stocks and change estimates did not exceed 20 $Mg \cdot ha^{-1}$.

Chapter 4 presents a comparison of airborne small-footprint (SF) and large-footprint (LF) lidar retrievals of ground elevation, vegetation height and biomass across a successional tropical forest gradient in central Gabon. The comparison of the two sensors shows that LF lidar waveforms are equivalent to simulated waveforms from SF lidar for retrieving ground elevation (RMSE=0.5 m, bias=0.29 m) and maximum forest height (RMSE=2.99 m; bias=0.24 m). Comparison of gridded LF lidar height with ground plots showed that an unbiased estimate of aboveground biomass at 1-ha can be achieved with a sufficient number of large footprints (> 3).

Lastly, Appendix A presents an open source R package for airborne lidar visualization and processing for forestry applications.

Acknowledgements

First and foremost, I would like to express my appreciation to my major advisors, Dr. Lee A. Vierling and Dr. Andrew T. Hudak for their assistance, encouragement, and insights throughout this journey. They pushed me when I needed it, but also gave me the freedom to explore my own research questions. Second, I am grateful to Dr. Nicholas Croonkston, for his kind support and valuable thoughts, which inspired me to advance my knowledge of statistics and R programming language.

I extend my gratitude to Dr. Jan U.H. Eitel, Dr. Luigi Boschetti and Dr. Michael Keller for their input and assistance as committee members. They all helped increase the level of research into a product I am proud of.

I would like to thank Dr. Sassan Saatchi at NASA's Jet Propulsion Laboratory (JPL) for his fruitful advice and unending encouragement. Gratitude is extended to all my friends at JPL, especially Dr. Mariano Garcia for his friendship and assistance with some of the data processing and statistical analysis used in this research.

A debt of thanks is owed to the University of Idaho (UI) and USDA Forest Service Rocky Mountain Research Station (RMRS) in Moscow, Idaho. I am grateful to all my friends from UI and RMRS for their friendship and support, especially Deanna Huffman and Benjamin Bright.

I wish to thank the National Council of Technological and Scientific Development—CNPq in Brazil for its financial support during these years (Science Without Borders Program - Process 249802/2013-9). I also thank the following organizations for partially funding this work: USDA Forest Service Rocky Mountain Research Station, the Strategic Environmental Research and Development Program (#RC-2243), and Jet Propulsion Laboratory, California Institute of Technology, National Aeronautics and Space Administration (NASA). Thanks to Klabin, a paper and pulp company in Brazil and the Brazilian Corporation for Agricultural Research (EMBRAPA) for providing the field and lidar data used in part of this reseach.

Last but not least, this research would not have been possible without the moral support, generosity, encouragement and love of my family. I am grateful, especially, to my wife Carine Klauberg Silva, for her unwavering support, patience, and understanding.

Dedication

For my wife Carine Klauberg Silva, my son Joaquim Klauberg Silva, my mother Sueli Silva and my sister Paula Fernanda Silva

Table of Contents

List of Figures

List of Tables

Introduction to the Dissertation

Accurate and spatially explicit measurement of forest structural attributes are required in other to effectively protect, monitor and manage forest ecosystems. Field measurements are considered the most accurate approach for measuring forest attributes, however, measuring forest structural attributes in either natural or plantation forests in the field is an extremely time consuming and labor-intensive task, especially in large or remote areas where access is limited, and a huge number of field plots are needed to characterize the forest variation.

Remote sensing technologies have been widely utilized to characterize forest structure at both local and global scales. For instance, in the past two decades, lidar (light detection and ranging) remote sensing has emerged as a technology well-suited to providing accurate estimates of forest attributes including height, volume, basal area and biomass both in natural and industrial plantation forest ecosystems (e.g., Næsset 1997; Drake et al. 2002; Lefsky et al., 2002; Hudak et al. 2006, Silva et al. 2014). However, even though lidar can quickly provide forest attributes across extensive landscapes, it is still mostly used for research purposes, mainly due to the high cost of data acquision and lack of optimized and accessible tools and methods for processing and modeling lidar data for forestry applications. Moreover, accurate prediction of forest attributes from lidar is highly dependent on methods. For instance, when lidar data and statistical models are not well implemented, inappropriate models are created, and forest attributes are estimated with high uncertainty levels, which consequently leads to serious problems for forest managers. This can create management uncertainty especially in industrial forest plantations where forest structural attributes are typically inventoried annually to support forest management decisions relating to silvicultural treatments, harvest planning, growing stock estimation and sustainability. Therefore, to overcome these limitations and make lidar technology practicable, operational and accessible to managers and researchers, both in governmental and no-governmental agencies, further development of novel, efficient and optimized methods for lidar data processing and modeling for forest applications are still required. This is particularly true in developing nations such as Brazil, where applications of lidar are in the early stages.

Enhanced understanding of forest structure via lidar remote sensing can be gained through improved tools and optimized frameworks. The research presented in this dissertation is therefore focused upon further development of strategies to promote conservation and sustainable management of natural and indisutral plantation forests. Specifically, the main goal of this dissertation is to develop and assess novel and advanced methods for 3-D forest characterization, and to map forest attributes at individual tree, plot and landscape levels from lidar remote sensing data. The dissertation, divided into six sections and an appendix, presents four specific case studies (Chapters 1-4) of lidar applications. Specifically, the first and last sections are the Introduction and Conclusion of the dissertation while Chapters 1-4 represent the main body of the dissertation. Chapters 1-4 use several lidar datasets, coupled with individual tree and plot level spatially explicit datasets, to demonstrate the usefulness of lidar remote sensing for effictively predicting and mapping forest attributes in natural and industrial plantation forests located across large spatial extents.

Chapter 1 develops and evaluates a novel framework to automatically detect individual trees and estimate tree attributes, such as tree height, diameter at breast height and volume in longleaf pine (*Pinus palustris* Mill.) forests using lidar and *k*-nearest neighbor (*k*-NN) imputation. Longleaf pine forests are fire-dependent, and accurate characterization of the forest at the individual-tree level not only enhances conventional and lidar area-based forest inventory, but also extends its applications into disciplines where greater detail is valued, such as in fire behavior and ecology. The data used in this chapter was provided by the Joseph W. Jones Ecological Research Center in southwestern Georgia, USA.

Chapter 2 presents a methodology for predicting stem total and assortment volumes in loblolly pine (*Pinus taeda* L.) forest plantations from lidar data using random forest models. Although random forest has been used in conjunction with lidar data to estimate many stand-level forest attributes, to date their efficacy for predicting assortment volumes in industrial forest plantations is largely untested. The methodology and products presented in Chapter 2 will be used by forest manangers and will play an important role in helping them to increase efficiency in monitoring and managing wood and pulp production in forest

plantations. The data used in this chapter were provided by Klabin, a pulp and paper company from Brazil.

Chapter 3 evaluates the impacts of airborne lidar pulse density on estimating aboveground biomass (AGB) stocks and changes in a selectively logged tropical forest. While airborne lidar can facilitate timely and accurate estimates of forest structure in tropical forest, trade-offs still exist between lidar pulse density and accuracy. For instance, it is unclear how much the lidar pulse density can be reduced and still maintain an adequate level of accuracy for AGB change estimation in tropical forests. The data used in Chapter 3 were provided by USAID and managed by the US Forest Service and the Brazilian Corporation for Agricultural Research (EMBRAPA) under the Sustainable Landscapes Brazil program.

Chapter 4 presents a comparison of airborne small-footprint (SF) and large-footprint (LF) lidar retrievals of ground elevation, vegetation height and biomass across a successional tropical forest gradient in central Gabon. The lidar data used in Chapter 4 were collected as part of the NASA and European Space Agency (ESA) AfriSAR campaign with the goal of verifying the performance of future spaceborne lidar (GEDI) and radar sensors such as ESA's BIOMASS mission and NASA-ISRO Synthetic Aperture Radar (NISAR) systems for ecosystem studies in quantifying vertical forest structure and AGB.

In addition to Chapters 1-4, Appendix A of this dissertation presents an open source R package (rLiDAR) for reading, processing and visualizing lidar data (Silva et al. 2015).

Chapters 1-3 were published in scientific journals prior to the preparation of this dissertation. Chapter 1 was published by the *Canadian Journal of Remote Sensing* with Dr. Andew Hudak, Dr. Lee Vierling, Dr. Louise Loudermilk, Dr. Joseph J. O'Brien; Dr. Kevin Hiers, Dr. Steve Jack; Dr. Carlos Gonzalez-Benecke; Dr. Heezin Lee; Dr. Michael Falkowski and Dr. Anahita Khosravipour as co-authors (Silva et al. 2016). Chapter 2 was published by *Forests* with Dr. Carine Klauberg, Dr. Andew Hudak, Dr. Lee Vierling, Dr. Wan Shafrina Wan Mohd Jaafar; Mr. Midhun Mohan, Dr. Mariano Garcia, Dr. Antonio Ferraz, Dr. Sassan Saatchi and Dr. Adrian Cardil as co-authors (Silva et al. 2017a). Chapter 3 was published by *Remote Sensing* with Dr. Andew Hudak, Dr. Lee Vierling, Dr. Carine Klauberg, Dr. Mariano Garcia, Dr. Antornio Ferraz, Dr. Michael Keller, Dr. Jan Eitel and

Dr. Sassan Saatchi as co-authors (Silva et al. 2017b). Errors identified in the publication proof stage of the above chapters were corrected in this dissertation. Chapter 4 has been submitted to IEEE Journal of Selected Topics in Applied Earth Observations and Remote Sensing with Dr. Sassan Saatchi, Dr. Mariano Garcia, Dr. Nicholas Labrière, Dr. Carine Klauberg, Dr. Victorya Meyer, Dr. Kathryn Brun-Jeffery; Dr. Katharine Abernethy, Dr. Lee White, Dr. Simon Lewis and Dr. Andrew Hudak as co-authors.

References

Drake, J.B.; Dubayah, R.O.; Knox, R.G.; Clark, D.B.; Blair, J.B. Sensitivity of large-footprint lidar to canopy structure and biomass in a neotropical rainforest. (2002)**.** *Remote Sens. Environ.*, *81*, 378–392, doi:10.1016/S0034-4257(02)00013-5.

Hudak, Andrew T.; Bright, Benjamin, C.; Satterberg, Kevin L. (2015). RxCADRE 2008, 2011, and 2012: Lidar data and derived raster products. Fort Collins, CO: Forest Service Research Data Archive. Updated 08 September 2016. https://doi.org/10.2737/RDS-2015-0010

Hudak, A.T., Crookston, N.L., Evans, J.S., Falkowski, M.J., Smith, A.M.S., and Gessler, P. (2006). Regression modeling and mapping of coniferous forest basal area and tree density from discrete-return LiDAR and multispectral satellite data. Canadian Journal of Remote Sensing, 32, 126–38.

Lefsky, M. A., Cohen, W. B., Parker, G. G., Harding, D. J. (2002).Lidar remote sensing for ecosystem studies. Bioscience, 52, 19-30

Næsset, E. (1997) Estimating timber volume of forest stands using airborne laser scanner data. Remote Sens. Environ., 61(2), 246-253, doi:10.1016/s0034-4257(97)00041-2.

Silva, C.A.; Klauberg, C.; Carvalho, S.D.P.C.; Hudak, A.T. (2014). Mapping aboveground carbon stocks using Liar data in *Eucalyptus* spp. plantations in the state of São Paulo, Brazil. *Sci. For.*, *42*, 591–604.

Silva, C.A.; Hudak, A.T.; Vierling, L.A.; Loudermilk, E.L.; O'Brien, J.J.; Hiers, J.K.; Jack, S.B.; Gonzalez-Benecke, C.A.; Lee, H.; Falkowski, M.J. (2016). Imputation of

individual longleaf pine forest attributes from field and LiDAR data. *Can. J. Remote Sens. 42*, 554–573, doi:10.1080/07038992.2016.1196582.

Silva, C.A.; Klauberg, C.; Hudak, A.T.; Vierling, L.A.; Jaafar, W.S.W.M.; Mohan, M.; Garcia, M.; Ferraz, A.; Cardil, A.; Saatchi, S. (2017a). Predicting Stem Total and Assortment Volumes in an Industrial *Pinus taeda* L. Forest Plantation Using Airborne Laser Scanning Data and Random Forest, *Forests*, *8*, 254.

Silva, C.A.; Hudak, A.T.; Vierling, L.A.; Klauberg, C.; Garcia, M.; Ferraz, A.; Keller, M.; Eitel, J.; Saatchi, S. (2017b) Impacts of Airborne Lidar Pulse Density on Estimating Biomass Stocks and Changes in a Selectively Logged Tropical Forest. Remote Sens., 9, 1068, DOI: 10.3390/rs9101068

Chapter 1. Imputation of Individual Longleaf Pine (*Pinus palustris* Mill.) Tree Attributes from Field and Lidar Data

Silva, C. A.; Hudak, A. T.; Vierling, L. A.; Loudermilk, E. L.; O'Brien, J. J.; Hiers, J. K.; Jack, S. B.; Gonzalez-Benecke, C.; Lee, H.; Falkowski, M. J.; Khosravipour, A. Imputation of individual longleaf pine (*Pinus palustris* Mill.) tree attributes from field and LiDAR data. Canadian Journal of Remote Sensing. 2016, 42(5): 554-573.

Abstract

Light Detection and Ranging (lidar) has demonstrated potential for forest inventory at the individual-tree level. The aim in this study was to predict individual-tree height (Ht; m), basal area (BA; m^2), and stem volume (V; m^3) attributes, imputing Random Forest *k*-nearest neighbor (RF *k*-NN) and individual-tree-level-based metrics extracted from a lidar-derived canopy height model (CHM) in a longleaf pine (*Pinus palustris* Mill.) forest in southwestern Georgia, United States. We developed a new framework for modeling tree-level forest attributes that comprise three steps: (i) individual tree detection, crown delineation, and tree-level-based metrics computation from lidar-derived CHM; (ii) automatic matching of lidar-derived trees and field-based trees for a regression modeling step using a novel algorithm; and (iii) RF *k*-NN imputation modeling for estimating tree-level Ht, BA, and V and subsequent summarization of these metrics at the plot and stand levels. RMSDs for tree-level Ht, BA, and V were 2.96%, 58.62%, and 8.19%, respectively. Although BA estimation accuracy was poor because of the longleaf pine growth habitat, individual-tree locations, Ht, and V were estimated with high accuracy, especially in low-canopy-cover conditions. Future efforts based on the findings could help improve the estimation accuracy of individual-tree-level attributes such as BA.

Keywords: rLiDAR, CHM, *k*-NN imputation, Random Forest, individual tree attributes, forest inventory.

1.1 Introduction

Longleaf pine (*Pinus palustris* Mill.) was once one of the most ecologically important tree species in the southern United States (Oswalt et al., 2012). Historically, longleaf pine forests spanned an estimated area of 92 million acres (Frost 2006) and were among the most extensive ecosystems in North America (Landers et al., 1995). Today, only 4% of these longleaf pine forests remain (Franklin 2008).

Fire is one of the dominant forces that shape the longleaf pine landscape (Dobbs 2011). Longleaf pine is dependent on fire for successful regeneration and for suppressing hardwood growth (Loudermilk et al., 2011). However, due to fire suppression, much of the remaining longleaf pine forest is in poor or degraded condition. As a result, there has been tremendous interest in longleaf pine conservation, management, and restoration (Brockway 2005).

Successful management of these forests can have sustainable results, because longleaf pines can produce quality wood products when grown in a variety of densities (Franklin 2008). Accurate measures of forest attributes such as tree density (tree·ha^{-1}), and attributes such as height (Ht), basal area (BA), and stem volume (V) that are used at the tree, plot and stand levels, are essential to management and conservation practices in longleaf pine forests. The most accurate method of estimating these attributes is to physically sample them in the field. However, individual tree field measurements over large areas are limited by budgets and time, making them impractical.

Airborne Light Detection and Ranging (lidar) systems have become the dominant remote sensing technique for plot- and stand-level forest inventory, mainly because this technology can quickly provide highly accurate and spatially detailed information about forest attributes across entire forested landscapes (Silva et al., 2014). Increased interest, dataset availability, and technological improvements have greatly expanded the use of lidar technologies in forestry over the past decade (Saremi et al., 2014; Hudak et al., 2006, 2009, 2014; Hansen et al., 2015). The use of airborne lidar to retrieve forest attributes at the tree level is promising, however, not as widely studied as plot- or stand-level approaches. In a tree-level-based modeling approach, individual-tree attributes are usually predicted through

three steps: (*i*) individual tree detection and metrics extraction, (*ii*) lidar- and field-based tree matching, and (*iii*) modeling and prediction.

The accurate prediction of tree-level attributes is highly dependent on the methods used to detect and extract individual-tree metrics and forest structure as well (Kankare et al., 2015). A lidar-derived Canopy Height Model (CHM) can be used for detecting individual trees, delineating tree crowns, and subsequently estimating biophysical attributes such as biomass and stem volume (Popescu et al., 2003; Popescu, 2007; Falkowski et al., 2008; Falkowski et al., 2009; Vauhko- nen et al., 2012; Hu et al., 2014; Duncanson et al., 2014; Duncanson et al., 2015; Kankare et al., 2015). There are a variety of approaches used to detect and delineate individual trees from lidar-derived CHMs. These include identifying local maxima (Popescu et al., 2003; Weinacker et al., 2004; Falkowski et al., 2008; Falkowski et al., 2009) for tree detection, as well as region growth (Hyyppa et al., 2001; Solberg et al., 2006; Pang et al., 2008), valley following (Leckie et al., 2003), and watershed (Chen et al., 2006; Jing et al., 2012) for tree crown delineation.

In addition to the individual-tree detection method and forest structure, the accurate prediction of forest attributes at the tree level is also highly dependent on the modeling technique applied (Vauhkonen et al., 2010). Examples of the existing methods for modeling forest attributes at the tree-level from lidar data are both parametric (Chen et al., 2007) and nonparametric (Breidenbach et al., 2010; Vauhkonen et al., 2010; Vauhkonen et al., 2012). Saarinen et al., (2014), Vastaranta et al., (2015) and Kankare et al., (2015) have recently tested *k*-nearest neighbor (*k*- NN) imputation for forest inventory modeling at the tree level. In most cases however, *k*-NN imputation, as a nonparametric method, has commonly been used to predict forest inventory attributes at the plot or stand levels (Falkowski et al., 2010; Hudak et al., 2014; Racine et al., 2014; McRoberts et al., 2015). For example, Hudak et al., (2008) evaluated nine *k*-NN imputation methods combined with lidar data for imputing plot-level BA and tree density (TD) of 11 conifer species occurring in mixed-conifer forests of north central Idaho, USA. Racine et al., (2014) used lidar data and *k*-NN imputation to estimate plot age across a managed boreal forest in Quebec, Canada, and Fekety et al., (2015) used repeated field and lidar survey data to assess the feasibility of

predicting forest inventory attributes across space and time in a conifer forest in northern Idaho, USA.

The aforementioned studies integrated lidar and field data in an area-based *k*-NN imputation to predict forest attributes at the plot or stand levels. However, accurate characterization of the forest at the individual-tree level not only enhances conventional and lidar area-based forest inventory, but also extends its applications into disciplines where greater detail is valued, such as ecology, wildlife habitat, or biodiversity applications (Goetz et al., 2007; Hinsley et al., 2002; Vierling et al., 2008).

Given that only a fraction of the historic longleaf pine forest ecosystem range remains today, accurate characterization and spatial distribution of individual trees are critical for sustainable forest management and for ecological and environmental protection in longleaf pine forests. Our goal in this study was to predict individual-tree-level attributes using *k*-NN imputation and individual-tree lidar-based metrics in a longleaf pine forest in southwestern Georgia, in the United States. Our first aim, therefore, was to evaluate the ability of lidar to accurately detect individual trees and determine treetop height (HMAX, m) and crown area (CA, m^2) that are subsequently used for predicting tree attributes. Our second aim was to predict individual tree Ht (m), BA (m^2), and V (m^3) attributes from HMAX and CA metrics using *k*-NN imputation and evaluate its accuracy and precision. This investigation is based on the hypothesis that lidar technology and a *k*-NN imputation modeling approach can feasibly provide accurate estimates of these tree attributes in the open canopy structure that is typical of healthy longleaf pine forests.

1.2 Material and Methods

1.2.1 Study area

The study area for this project is located at Ichauway, an 11,700 ha reserve of the Joseph W. Jones Ecological Research Center in southwestern Georgia, USA (Figure 1.1). The area is characterized by a humid subtropical climate (Christensen 1981) with a mean annual precipitation of 131 cm fairly evenly spread throughout the year. Mean daily temperatures range from 21 ˚C to 34 ˚C in the summer and 5 ˚C to 17 ˚C in the winter (Loudermilk et al., 2011). Elevation ranges from 6.23 m to 33.66 m, and the soils are

characterized as paleudults, kandiudults, and hapludults with some localized quartzipsamments (Kirkman et al., 2004). The Ichauway reserve has an extensive tract of second- growth longleaf pine managed with low-intensity, dormant- season-prescribed fires at a frequency of about 1–3 years since 1945 (Loudermilk et al., 2011).

In this study, vegetation structure is characterized by an open canopy longleaf pine forest (Figure 1.1a, b) and a wiregrass- dominated ground cover maintained under a high-frequency fire regime (Figure 1.1c). Maintaining a high-frequency fire regime through repeated application of prescribed fire is a top management goal at Ichauway, with occasional individual-tree selection harvesting for management and research purposes in the natural, second-growth longleaf forests (Palik et al. 2003).

1.2.2 Field Data Collection

The field measurements were carried out from March 2009 to July 2009. A total of 15 rectangular plots (about 4 ha each) were established in 3 stands: CNT, NE, and NW (Figure 1.1d). All plots were georeferenced with a geodetic GPS with differential correction capability (Trimble Nomad) with an external Hemisphere Crescent A100 antenna, and all had a horizontal accuracy of < 0.6 m with differential GPS (DGPS) and < 2.5 m without DGPS in open canopy, and 1 m^{-2} m accuracy with DGPS under forest canopy. All trees were measured for DBH using calipers (two perpendicular measurements at right angles, averaged) or a steel diameter tape, and for Ht using a LaserTech Impulse 200. We also geolocated (UTM E, N) them using the GPS mentioned, and, from these measures, a field-stem map was created. In a few instances, DGPS was not able to resolve locations of multiple small trees in areas with high stocking, and tree locations were recorded by establishing a known DGPS.

The outside-bark V (m^3) was obtained via a longleaf pine allometric equation according to Gonzalez-Benecke et al., (2014) (Equation 1.1). The equation has a coefficient of determination (R^2) of 0.78 and absolute and relative root mean square error (RMSE) of 0.17 m^3 and 38.21%, respectively.

$$\ln(V) = -9.944543 + 3.123691 * \ln(Ht). \quad (1.1)$$

In addition to V, tree-level BA was also computed. Statistical summaries of the reference field measurements and BA and V calculations are presented in Table 1.1 and Table 1.2.

1.2.3 Lidar Data and Pre-processing

Lidar data were acquired using an Optech GEMINI Air- borne Laser Terrain Mapper (ALTM) mounted in a twin-engine Cessna Skymaster (Tail Number N337P). The survey was carried out on March 5, 2008. Lidar flight parameters are presented in Table 1.3.

Lidar preprocessing was performed using US Forest Service FUSION/LDV 3.42 software (McGaughey 2015) and LAStools (Isenburg 2015). The workflow is graphically shown in Figure 1.2a. First, in FUSION/LDV, the quality of the lidar dataset was visually evaluated, and a simple report using the Catalog tool was generated. A filtering algorithm based on Kraus and Pfeifer (1998) was applied to differentiate between ground and nonground returns. Digital Terrain Models (DTMs) were generated using the classified ground points with a spatial resolution of 1.0 m, using the GridSurfaceCreate function. The CanopyModel tool was then used to interpolate vegetation points and to generate Digital Surface Models (DSMs) with a spatial resolution of 0.5 m. Afterward, the ClipData tool was applied with the height and dtm switches to normalize heights and to assure that the z coordinate for each point corresponded to the height above ground and not the orthometric elevation of the single point. The PolyClipData tool was then used to make a subset of the lidar points within each of the 15 in situ measured test plots. The cloudMetrics tool with a height and cover thresholds of 1.37 m (Nilsson 1996) were used to compute the canopy cover (COV,%), within sample plots. COV was calculated as the number of lidar first returns above 1.37 m, divided by the total number of first returns. Such lidar-derived CHM often contain height irregularities within individual-tree crowns—so-called data pits—which reduce accuracy in tree detection and subsequent extraction of biophysical parameters (Gaveau and Hill 2003, Shamsoddini et al., 2013). Therefore, the pit-free algorithm, developed by Khosravipour et al., (2014) was used to generate a pit-free CHM at 0.5-m spatial resolution though a workflow implemented in LAStools (Isenburg 2015).

1.2.4 Individual tree detection and HMAX extraction

Individual tree detection was performed in R (R Development Core Team 2015) using the FindTreesCHM function from the rLiDAR package (Silva et al., 2015). The FindTreesCHM function uses a local maximum algorithm to search for tree tops in the CHM through a moving window with a fixed tree-top window size (TWS; Wulder et al., 2000). To achieve optimal tree detection, we tested 3 TWS (3 x 3, 5 x 5, and 7 x 7 pixels) first on an unsmoothed CHM, and then on a CHM smoothed by a mean smooth filter with fixed smoothing window size (SWS) of 3 x 3 and 5 x 5 pixels. Even when the smoothed CHM option was used to find trees, the treetop heights (HMAX) were extracted from the unsmoothed CHM.

A total of 15 test subplots (30 m 30 m) were randomly situated within each of the 15 plots (1 subplot per plot), and the number of trees detected (NTD) per subplot from lidar were manually compared with field-based data and evaluated in terms of true positive (TP, correct detection), false negative (FN, omission error) and false positive (FP, commission error). The accuracy of the detection was further evaluated for recall (r), precision (p) and F-score (F) according to Li et al. (2012), using the following equations (Goutte and Gaussier 2005; Sokolova et al., 2006):

$$r = \frac{TP}{TP+FN} \tag{1.2}$$

$$p = \frac{TP}{TP+FP} \tag{1.3}$$

$$F = 2 * \frac{r * p}{r+p} \tag{1.4}$$

Note that recall is inversely related to omission error and represents the tree detection rate. Precision is inversely related to commission error and describes the rate of correct detections. F-score is used to represent the harmonic mean of recall and precision, which takes both commission and omission errors into consideration. Hence, a higher F-score indicates that both commission and omission errors are lower (Li et al., 2012). Recall,

precision and F-score ranges from 0 to 1, and the F-score will become higher with higher p and r values.

1.2.5 Individual tree crown delineation and crown area computation

Tree-crown delineation was also performed in R, using the ForestCAS function from the rLiDAR package (Silva et al., 2015). Inputs to this process were the smoothed CHM in addition to the tree-location output described in the previous steps. The algorithm implemented in the ForestCAS function is shown in Figure 1.2c and Figure 1.3, and follows the example presented in the figure illustrating 3 hypothetical trees (Figure 1.3a). The algorithm starts by applying a variable radius crown buffer (Figure 1.3b) to delimit the initial tree crown area. In this study, the variable radius was calculated for each tree by multiplying the lidar-derived tree height by 0.6, because preliminary field observation revealed that the tree crown radius typically was not larger than 60% of the lidar-derived tree height. After determining the merged tree polygon using the first area delimitation (Figure 1.3b), we then split the data using the centroidal voronoi tessellation approach (Aurenhammer and Klein 1999) to isolate each individual-tree polygon (Figure 1.3c, d). After isolating each tree polygon, we clipped them from the CHM and excluded the grid cells with values below 30% of the HMAX in each specific detected tree (Figure 1.3e) to eliminate the low-lying noise. Finally, the tree-crown delineation and crown area (CA, m^2) were computed by delimiting the boundary of grid cells belonging to each tree (Figure 1.3f).

1.2.6 rSTree: Searching for the lidar and reference trees

Forest inventory and modeling of individual trees using field and lidar data is a highly desirable approach. However, to develop this type of modeling approach, the challenge is to match lidar-delimited trees with reference trees measured in the field. In many cases, the tree-location reference measured in the field is inaccurate (often due to GPS error), complicating the individual-tree-level modeling approach. Instead of manually moving reference tree locations to match with the tree locations detected from lidar, we developed a novel approach for matching lidar and field trees automatically (Figure 1.4). The proposed rSTree algorithm uses the acceptable maximum Euclidian distance (MED) and minimum height difference (MHD) computed between lidar and field-based data, in

terms of tree location and height, respectively, as the imputed parameters. The algorithm processes a single match tree at a time, and it starts with the first detected lidar tree. The user-defined MED parameter is then used to buffer a search area for a possible matching tree. In this study, we used 10 m, because, given the GPS errors, we are assuming that the reference tree is within a radius of 10 m. The field-based trees located inside the search area are selected. Trees with height difference (HD) ≤ MHD are then selected for the next step as target trees. In this study, we used MHD = 1.5 m, because most of the literature for conifer lidar versus field stems have reported a RMSE in height of ~ 1 m (e.g., Vastaranta et al. 2014). In an open canopy forest such as longleaf pine presented herein, we are assuming that the error in lidar height would not exceed 1.5 m. If more than one reference field-based tree has HD ≤ MHD, the trees are ranked by HD and the tree with the smallest HD is selected. If 2 or more field-based trees have a perfect match in terms of smallest HD and distance to the detected tree, we randomly selected one as the target field-based tree to match with the lidar tree. After all interactions, the lidar and reference trees are combined, added, and exported as a table for the individual-tree-level attributes modeling approach.

1.2.7 Imputation modeling development

In this study, because the height–diameter allometry for longleaf pine breaks down after reaching a diameter of ∼25 cm, when height growth asymptotes at ∼25 m (Gonzalez-Benecke et al., 2014), we believed that a nonparametric modeling technique to predict forest attributes at tree level would be more appropriate than a parametric model. Therefore, *k*-NN imputation, a nonparametric technique, was conducted using the yaImpute (Crookston and Finley 2008) package in the R statistical software (R Core Team 2015). Many imputation methods can be used for associating target and reference observations; however, recent studies have shown that the Random Forest (Breiman 2001) approach generally produces better results compared to other imputation methods (Hudak et al., 2008; Nelson et al., 2011; Waske et al., 2012). For this study, we used Random Forest-based *k*-NN (RF *k*-NN) to characterize the relationships between predictor (HMAX and CA) and response (Ht, BA, and V) variables used for imputation. The number of neighbors was set

to one (k= 1) to maintain the original variance in the data (Hudak et al., 2008). The dataset for the modeling process was randomly split into subsets with 75% for training and 25% for testing, and a total of 1,000 regression trees were fitted in the RF *k*-NN model.

1.2.8 Model assessment

Accuracy of the imputation model was assessed by calculating the absolute and relative root mean square distance (RMSD, RMSD%) and bias (Bias, Bias%) between imputations and observations (Stage and Crookston 2007), computed for a single response variable as follows:

$$\text{RMSD} = \sqrt{\frac{\sum_{i=1}^{n}(I_i - O_i)^2}{n}} \quad (5)$$

$$\text{Bias} = \frac{1}{n}\sum_{i=1}^{n}(I_i - O_i) \quad (6)$$

where I is the imputed value of a variable, O is the observed value, and n is the number of reference observations. The RMSD is analogous to the RMSE used to assess regression model accuracy (Stage and Crookston 2007). The relative RMSD and Bias are computed by dividing absolute RMSD and Bias by the mean of the variable computed over the reference observations and multiplied by 100. We defined acceptable model precision and accuracy as a relative RMSD and Bias of 15% to have a model precision and accuracy higher than or equal to the conventional forest inventory standard in the longleaf pine. We also employed statistical equivalence tests to assess whether the imputed tree attributes are statistically similar (i.e., equivalent) to the field-based attributes (Robinson et al., 2005). According to Smith et al., (2009), statistical equivalence tests are used to test the null hypothesis of "no substantial difference" between 2 sample populations (H0: the sample populations are different; H1: the sample populations are equivalent). We employed a regression-based equivalence test to test for intercept equality (i.e., the mean of imputed tree attribute is equal to the mean of the field-based attribute) and slope equality to 1 (i.e., if the pairwise, imputed and observed, attributes are equal, the regression will have a slope of 1). A description of equivalence tests can be also found in the "equivalence" package in R

(Robinson, 2015), and examples of equivalence plots in lidar studies can be found in Falkowski et al., (2008), Smith et al., (2009), Hudak et al., (2012), and Silva et al., (2014).

1.2.9 Stand-level imputation of tree attributes

According to Falkowski et al., (2008), tree-detection accuracy decreases with increasing COV. An adaptive approach using COV as a constraint to select the best parameters of TWS and SWS for tree detection was developed in this study. Therefore, we tiled the normalized point cloud using a grid-layer of 200 m x 200 m square plots, and for each single tile we computed COV, which was calculated by the number of lidar first returns above 1.37 m, divided by the total number of first returns. A buffer of 30 m was applied over each single square layer to remove the edge effect of the individual tree detection. As the parameters of the tree detection at stand level was dependent on the results from the test plots, our hypothesis was that small TWS would provide better results in close canopy area, and vice versa. In the buffer overlaid areas, after tree detection using the FindTreesCHM function from the rLiDAR package (Silva et al., 2015), 1 of 2 trees detected was automatically removed to avoid overdetection. Afterward, tree-crown delineation was performed across the entire stand, using the ForestCAS function from the rLiDAR package (Silva et. Al., 2015). The RF *k*-NN imputed model based in the test plots was then applied, and the tree attributes Ht, BA, and V were estimated for each single tree across all stands.

1.3 Results

1.3.1 Stand-Level Characterization from Field Data and Lidar-Based Plot Metrics

According to the lidar-derived HMAX value, canopy height of the longleaf pine forest was similar across the 3 stands (Figure 1.5a). Lidar-derived COV indicated a decrease in percent canopy cover from the NW to CNT and NE stands, whereas COV variance increased (Figure 5b). Although the stands are similar in height, they are different in terms of field-measured tree density. As observed in the description of the sites in the material and methods section, the NW stand had highest tree density and the NE stand had the lowest, whereas the variance in tree density showed the opposite trend in COV (Figure 1.5c).

1.3.2 Individual-Tree Detection

The individual-tree detection results from the test plots are shown in Table 1.4. The TWS and SWS combination were sensitive parameters in terms of tree detection. The TWSs that provide better results were 5x5 and 7x7 pixels, with a tree detection overall improvement of 58.25% and 34.59% compared to the 3x3, respectively. The relationship between SWS and the NTD from lidar was inversely proportional. Smaller TWSs, such as 3x3 pixels, detected more trees compared to large TWSs, such as 7x7, causing an overestimation of NTD. In general, TWS of 3x3 for the CHM smoothing provided better results.

Although different combinations of TWS and SWS parameters might provide a better performance in each test plot, we identified a positive and strong nonlinear relationship between the number of reference trees and lidar-derived COV (Figure 1.6a). Therefore, in an effort to be consistent and replicable, we decided to use the adaptive approach already cited in the methods section, in which the COV is used as an auxiliary variable to select the TWS in each test plot. For the sample plots with COV > 70%, the 5x5 TWS was selected and in plots with COV < 70% the 7x7 TWS was selected. Additionally, the SWS of 3x3 pixels was selected to be applied across all test plots, because it in general provides more accurate results (Table 1.4).

The relationship between the reference and lidar-derived number of trees per test plot according to the adaptive approach mentioned is shown in Figure 1.6b. Our method slightly underestimates the number of trees, especially in the test plots with COV > 70%. However, the correlation between reference and NTD per hectare ($N \cdot ha^{-1}$) is relatively strong, displaying a correlation coefficient of 0.90.

The accuracy assessment results for individual-tree detection in the 15 test subplots is shown in Table 1.5. The recall varies from 0.74 to 1, with the overall value of 0.82; the value of p varies from 0.71 to 1, with the overall value of 0.85; and the F-score, which considers both of these last 2 factors, varies from 0.74 to 1, with the overall value from all the plots of 0.83. There are 185 reference trees in our test subplots, and only 177 (81.6%) trees were detected. In summary, the algorithm missed 34 (14.1%) trees, and falsely detected 26 (18.1%) trees, with underdetection outweighing overdetection (Table 1.5 and 1.6).

The strongest results were obtained in test subplots with COV < 70%, with 96% of the trees detected, commission and omission errors limited to 17.0 and 2% and an F-score of 0.90. When considering test subplots with COV > 70%, the algorithm detected 76% of trees with commission and omission errors of 13% and 24%, respectively (Table 1.6). The relationship between the F-score and COV is shown in Figure 1.7. The correlation is relatively strong, with a correlation coefficient of 0.91.

The lidar-derived HMAX ranged from 5.24 m to 31.91 m with mean and standard deviation (SD) of 24.39 m and 3.18 m, respectively. The lidar-derived CA ranged from 3.0 m^2 to 204.5 m^2, with mean and SD of 50.2 m^2 and 24.74 m^2, respectively. The distributions of HMAX and CA are shown in the Figure 1.8.

1.3.3 Imputation Modeling Estimates at Tree Level at the Test Plots

The rStree algorithm matched 4,242 detected trees to field- based trees (48.0%). From this total, 3181 (75%) trees were used as training and 1061 (25%) trees were used as testing data for imputation modeling. The HMAX and CA metrics were better predictors of Ht and V than BA. The imputed training model produced a relative RMSD of 2.56%, 57.33% and 7.49%; relative BIAS of 0.08%, 0.50% and 0.22%, and pseudo-R2 of 0.96, 0.22, and 0.95 for the Ht, BA, and V attributes, respectively.

The imputed and observed Ht and V attributes from the validation dataset were statistically equivalent at the 25% rejection region (Figure 1.9a,c). However, the imputed and observed BA values were not statistically equivalent at the 25% rejection region (Figure 1.9b). The Ht and V imputation models produced estimates that were strongly ($r > 0.97$) correlated with the validation inventory dataset, whereas the BA imputation model produced estimates of BA that were weakly correlated ($r=0.42$) with the validation data. The RMSD and Bias values were relatively low, whereas pseudo-R^2 values were high for the Ht and V. On the contrary, the RMSD and Bias was relatively high, and the pseudo-R^2 relatively low, for the BA estimates. The distributions of imputed and observed forest attributes across all stands from the testing dataset are shown in the Figure 1.10. In general, the similarity between the observed and imputed attributes is high.

1.3.4 Stand-Level Forest Attributes Estimates

The N of trees detected in the stands ranged from 35,980 to 52,184; mean tree Ht ranged from 21.10 to 23.17 m; mean tree BA ranged from 0.09 to 0.10 m^2 and mean tree V ranged from 0.79 to 0.96 m^3, as presented in Table1.7 Mean stand-level BA was 10.73 $m^2 \cdot ha^{-1}$ (± 2.69 $m^2 \cdot ha^{-1}$) and mean stand-level V was 99.94 $m^3 \cdot ha^{-1}$ (± 26.25 $m^3 \cdot ha^{-1}$). We also graphed histograms of imputed values for each stand and the shape of these distributions (Figure 1.11). The distributions show that the NW stand is the most mature, the NE stand has the highest proportion of smaller trees, and the CNT stand has an intermediate structure. These distributions provide more information that is subsumed within the Ht, BA, and V mean and standard deviation trends between stands, as summarized in Figure 1.5.

1.4 Discussion

1.4.1 Individual Tree Detection

Accurate individual-tree attributes are critical for forest assessment and planning. This study presents a simplified framework for automated, lidar-based individual-tree detection and modeling procedure for estimating tree attributes. The results presented herein demonstrate that the total number of trees can be derived with satisfactory accuracy.

We found that the successful identification of tree locations using the local maximum technique depends on the careful selection of the TWS. If the TWS is too small or too large, errors of commission or, respectively, omission occur, as was also reported by Wulder et al. (2000). Tree-detection accuracy was greatly affected by the different TWS and SWS combinations tested (Table 1.4). TWS was inversely proportional to the number of trees detected in general. Because COV is directly proportional to tree density in general, larger TWS is generally more appropriate in open canopy forest structures. In this study, 70% COV was the threshold chosen as the TWS; this is substantially higher than the 50% threshold reported in previous studies (Falkowski et al. 2008) and represents a significant advance in our ability to extract individual-tree attributes from denser coniferous forest canopies. Even though different combination of TWS and SWS would provide high accuracies in certain local areas, a consistent TWS parameter is also advantageous for

automated tree detection across large spatial extents, and therefore, we employed the COV variable as a criterion for adapting the TWS.

Smoothing is a common technique applied to lidar-derived CHMs for individual tree detection purposes. In this study, we tested the mean smoothing filter as a smoother. Khosravipour et al. (2014) reported that the performance of individual-tree detection was better using pit-free CHMs instead of a standard smoothed Gaussian CHM (in a coniferous plantation forest in Barcelonnette basin, southern French Alps, France). We observed the same improvement, but then further applied the 3x3 pixels SWS over the pit-free CHM to produce even more accurate results. Applying the 3 × 3 pixels SWS the irregular crown shapes that typify longleaf pine tree crowns (compared to other conifers, which tend to have a more regular, conical shape), thus eliminating spurious local maxima caused, for example, by longleaf pine tree branches that were not already removed by the pit-free CHM itself. Filter sizes and the conditions for filtering the CHM must be carefully tested and selected for different forest types (Lindberg and Hollaus 2012).

The tree-detection results from this study are comparable to the results obtained in other studies using both point cloud and raster-based approaches. Li et al. (2012), using a new method for segmenting individual trees from the lidar point cloud in a mixed conifer forest on the western slope of central Sierra Nevada Mountains of California, USA, showed that the algorithm detected 86% of the trees ("recall"), and 94% of the trees were segmented correctly ("precision"), with an overall F-score of 0.90. Vega et al. (2014), using the PTrees algorithm to segment individual trees in a conifer plantation in southwestern France, reported overall recall, precision, and F-score of 0.93%, 0.98%, and 0.95, respectively. Khosravipour et al., (2014), comparing the accuracy of individual-tree detection from the lidar-derived Gaussian smoothed and pit-free CHMs in mixed forest in southern French Alps in France, achieved an overall accuracy of 70.6% and 74.2%, respectively, from high-density lidar, and 35.7% and 67.7%, respectively, from artificially thinned, low-density lidar data. Lahivaara et al. (2014), using a Bayesian approach to tree detection based on lidar data, reported an accuracy of 70.2% for 2751 trees measured across 36 different field plots in a managed boreal forest in Eastern Finland. Maltamo et al., (2004), in state-owned forest located in Kalkkinen, southern Finland, using local maximum and segmentation techniques,

detected only 39.5% of all trees, although the proportion of detected dominant trees was as high as 83.0%.

In this study, the accuracy of individual-tree detection measured by the F-score, as expected, was inversely proportional to forest COV. Overall, commission errors were more prevalent in less dense test plots, and omission errors were more common where crowns overlapped. Previous research has shown that tree-detection accuracy decreases with increasing canopy cover (Falkowski et al. 2008). As also reported in Falkowski et al., (2008), the influence of GPS error is also an unquantifiable source of uncertainty in the current study. Popescu (2007) reported that treetop positions might be determined with higher accuracy using a CHM image rather than error-prone measurements derived from differential GPS in the field. Even though we collected at least 20 GPS positions at each tree and performed a differential correction, it can be argued that the field GPS tree location is less accurate than the treetop location detected from lidar, especially in high-canopy-cover conditions that can degrade field GPS accuracy (Wing et al., 2008). For example, in Figure 12, the reference tree location represented by the black point (Figure 1.12a) and vertical black line (Figure 12b,c) are located far away from the treetop location (white point, Figure 1.12a) and the point cloud peaks (Figure 1.12b). This leads to a less accurate stem map in areas with high COV, ultimately making it very difficult to objectively determine if a sample tree had actually been detected in high-canopy-cover situations. Moreover, the irregular shape of longleaf pine tree crowns likely further reduces tree detection accuracy compared to most other conifer species with more regular conical crowns.

1.4.2 Imputing Forest Attributes at Tree Level

In this study, we used an individual tree detection and crown delineation approach to compute HMAX and CA, which were subsequently employed as predictors to estimate tree-level metrics such as V and BA in a modeling framework (RF *k*-NN imputation). This is the first study to detect individual trees and model tree-level attributes using such an approach in longleaf pine forest.

In the modeling process, before building the tree-level RF *k*-NN imputation model, it was necessary to match individual trees detected from the lidar-derived CHM with the

associated reference trees measured in the test plots. The rSTree was able to match up 48.0% of all reference trees. Most of the missed trees occurred in test plots with COV conditions over 70%. However, even though an ideal situation (i.e., matching all the lidar and reference trees) was not achieved, the rStree algorithm proposed herein is still appropriate for tree matching when GPS errors in the field-based stem map are an issue.

Error in estimating Ht, BA, and V came disproportionately from young trees, although these comprised only 1.9% of the total number of stems. Additional error could be attributed to the 1-year difference between the lidar acquisitions (2008) and field measurements (2009). Nevertheless, the accuracies of the RF *k*-NN imputation model for imputing Ht and V were satisfactory, with RMSD in the cross-validation ranging from 2.96% to 8.19%, clearly surpassing the stated goal of less than 15%. However, the adjusted model was not able to accurately model BA. However, the primary contributor to the high BA estimation error is that the height–diameter allometry for longleaf pine breaks down after reaching a diameter of 25 cm, when height growth asymptotes at 25 m (Gonzalez-Benecke et al., 2014). The addition of crown-dimension attributes to a biometric model can help, but in this study, it did not explain much BA variance.

The use of airborne lidar to retrieve forest attributes such as Ht, V, and BA at tree level has been not widely studied, however, some previous studies have shown the great potential of this technology to provide it. For example, Maltamo et al., (2009), using lidar-based metrics and *k*-Most Similar Neighbor (*k*- MSN) imputation for predicting tree-level characteristics from a reference dataset comprising 133 trees, reported relative RMSEs of 1.95%, 5.6%, and 11.0% for the Ht, DBH, and V attributes estimation in 14 Scots pine (*Pinus sylvestris* L.) plots located in the Koli National Park in North Karelia, eastern Finland. Vauhkonen et al. (2010), working in mixed conifer mixed forest dominated mostly by Scots pine and Norway spruce (*Picea abies* L. Karst.) in southern of Finland, employed *k*-MSN and RF imputation methods simultaneously for estimating stem dimensions using lidar-based variables, and reported relative RMSEs of 3%, 13% and 31%, for Ht, DBH, and V, respectively. Vastaranta et al. (2014) using a multisource single-tree inventory (MS-STI) in a broad mixture of forest stands located in Evo, Finland, reported RMSEs ranging from 4.2% to 5.3%, from 10.9% to 19.9% and from 28.7% to 43.5%, for Ht, DBH, and saw log

volume, respectively. Our accuracies were not higher than those reports in Maltamo et al., (2009) and Vauhkonen et al., (2010). However, it is difficult to compare these results with ours owing to methodological and site differences. Lindberg and Hollaus (2012) reported estimates of individual tree BA that were more accurate based on the regression models than those derived from identifying tree tops from local maxima in the CHM in hemi-boreal forest in the southwest of Sweden. Furthermore, Vauhkonen et al. (2010) reported that the variation in RMSEs of 11%–15% for individual-tree BA estimation was due to the type of method (*k*-MSN or RF), value of k, and the set of predictor variables applied in the modeling process. In another study, also in Evo, Finland, Kankare et al., (2015) verified that the DBH accuracy was inversely proportional to tree density, where DBH accuracy decreased when tree density increased.

Our BA results might be improved by optimizing *k* or adding more individual tree metrics as predictors, such as canopy volume (Chen et al., 2007, Vauhkonen et al., 2010). Even though it is time consuming, individual tree segmentation directly from the lidar point cloud methods as presented by Reitberger et al., (2009), Ferraz et al., (2012) and Yao et al., (2013) are considered alternatives to increase the number of individual-tree metrics to be derived from the lidar point cloud data, as can be accomplished with the rLiDAR package (Silva et al., 2015). We have tested the rLiDAR algorithms for individual-tree detection and crown delineation on a CHM derived from airborne lidar at plot and stand levels; the rLiDAR package is not designed to ingest large lidar datasets, due to inherent memory limitations of R compared to specialized lidar processing software such as FUSION/LDV and LAStools.

1.4.3 Stand-Level Forest Attributes Characterization

The longleaf pine forest attributes estimates reported in this study represent useful information for the study and management of the longleaf pine forest at the Ichauway site. The spatially detailed information such as the number, location, spacing, size, Ht, BA, and V distribution of individual trees as available in map form (not shown) helps managers achieve greater management and conservation efficiency. Forestry studies often produce estimates of the stand-level forest attributes and how they change over time (Gonzalez-Benecke et al.,

2014). Therefore, distributions of forest structure attributes (Fig. 1.11) are relevant for forest management and planning.

1.5 Conclusions

In this study, we investigated the use of lidar and RF *k*-NN imputation for individual tree detection and forest attributes modeling in longleaf pine forest. Overall, our method detects individual trees with high accuracy in areas with < 70% COV. The precision and accuracy of lidar in retrieving Ht and V parameters at an individual-tree level using the framework presented was clearly demonstrated through a relative RMSE and bias less than 15%. Even though the desired accuracy of BA was not fully attained, the framework presented herein can serve as a useful methodology, and the result will ultimately support further study and management of longleaf pine forest ecosystems in the study area. We hope that the promising results for individual-tree-level forest-attribute modeling in this study will stimulate further research and applications not just in longleaf pine but other forest types.

References

Aurenhammer, F., and Klein, R. (1999). Voronoi diagrams. In Hand- book on Computational Geometry, edited by J.R. Sack and G. Urru- tia, pp. 201–290. Amsterdam: Elsevier.

Breidenbach, J., Næsset, E., Lien, V., Gobakken, T., and Solberg, S. (2010). Prediction of species specific forest inventory attributes using a nonparametric semi-individual tree crown approach based on fused airborne laser scanning and multispectral data. Remote Sensing of Environment, 114, 911–924.

Breiman, L. (2001). Random forest. Machine Learning, 45(1), pp. 5–32.

Brockway, D.G., Outcalt, K.W., Tomczak, D.J., and Johnson, E.E. (2005). Restoration of Longleaf Pine Ecosystems. Report No. 83. Southern Research Station, Asheville, NC, USA: US Department of Agriculture, Forest Service.

Crookston, N.L., and Finley, A.O. (2008). yaImpute: An R package for kNN imputation. Journal of Statistical Software, 23,1–16.

Chen, Q., Baldocchi, D., Gong, P., and Kelly, M. (2006). Isolating individual trees in a savanna woodland using small footprint lidar data. Photogrammetric Engineering & Remote Sensing, 72(8), 923–932.

Chen, Q., Gong, P., Baldocchi, D., and Tian, Y.Q. (2007). Estimating basal area and stem volume for individual trees from lidar data. Photogrammetric Engineering & Remote Sensing, 73(12), 1355–1365.

Christensen, N.L. (1981). Fire regimes in south-eastern ecosystems. In Fire Regimes and Ecosystem Properties: Proceedings of the Con- ference. General Technical. Report No. 26. edited by H.A. Mooney, T.M. Bonnicksen, J.R. Christensen, L. Norman, J.E. Lotan, and W.A. Reiners. Washington, D.: USDA Forest Service.

Dobbs Jr., R.H. (2011). Environmental State of the State Longleaf Pine Ecosystem. Report No.1. Atlanta, GA: R. Howard Dobbs Jr. Foun- dation.

Duncanson, L.I., Cook, B.D., Hurtt, G.C., and Dubayah, R.O. (2014). An efficient, multi-layered crown delineation algorithm for map- ping individual tree structure across multiple ecosystems. Remote Sensing of Environment, 154, 378–386.

Duncanson, L.I., Dubayah, R.O., Cook, B.D., Rosette, J., and Parker, G. (2015). The importance of spatial detail: Assessing the utility of individual crown information and scaling approaches for Lidar- based biomass density estimation. Remote Sensing of Environment, 168, 102–12.

Falkowski, M.J., Smith, A.M.S., Gessler, P., Hudak, A.T., Vierling, L.A. and Evans, J.S. (2008). The influence of conifer forest canopy cover on the accuracy of two individual tree measurement algo- rithms using lidar data." Canadian Journal of Remote Sensing, 34(2), 1–13.

Falkowski, M.J., Evans, J.S., Martinuzzi, S., Gessler, P.E., and Hu- dak, A.T. (2009). Characterizing forest succession with lidar data: An evaluation for the Inland Northwest, USA. Remote Sensing of Environment, 113 (5), 946–956.

Falkowski, M.J., Hudak, A.T., Crookston, N.L., Gessler, P.E., Uebler, E.H., and Smith, A.M.S. (2010). Nearest neighbor imputation ap- proach incorporating lidar data. Canadian Journal of Forest Re- search, 40(2), 184–199.

Fekety, P.A, Falkowski, M.J., and Hudak, A.T. (2015). Temporal trans- ferability of lidar-based imputation of forest inventory attributes." Canadian Journal of Forest Research, 45(4), 422–435.

Ferraz, A., Bretar, F., Jacquemoud, S., Gonc¸alves, G., Pereira, L., Tome´, M., and Soares, P. (2012). 3-D mapping of a multi-layered Mediter- ranean forest using ALS data." Remote Sensing of Environment, 121, 210–23.

Franklin, R.M. (2008). Stewardship of Long Leaf Pine Forests: A Guide for Landowners. Report No. 2. Clemson, SC, USA: Clemson Uni- versity Cooperative Extension Service.

Frost, C. (2006). History and future of the longleaf pine ecosystem. In the Longleaf Pine Ecosystem: Ecology, Silviculture, and Restora- tion, edited by S. Jose, E.J. Jokela, and D.L. Miller, pp. 9–48. New York: Springer Science & Business Media.

Gaveau, D.L., and Hill, R.A. (2003). Quantifying canopy height un- derestimation by laser pulse penetration in small-footprint airborne laser scanning data. Canadian Journal of Remote Sensing, 29, 650–657.

Goetz, S., Steinberg, D., Dubayah, R., and Blair, B. (2007). Laser remote sensing of canopy habitat heterogeneity as a predictor of bird species richness in an Eastern Temperate forest, USA. Remote Sensing of Environment, 108(3), 254–263.

Gonzalez-Benecke, C.A., Gezan, S.A., Samuelson, L.J., Cropper, W.P., Leduc, D.L., and Martin, T.A. (2014). Estimating Pinus palustris tree diameter and stem volume from tree height, crown area and stand- level parameters. Journal of Forestry Research, 25(1), 43–52.

Goutte, C., and Gaussier, E. (2005). A probabilistic interpretation of precision, recall and F-score, with implication for evaluation. Advances in Information Retrieval, (3408), 345– 359.

Hansen, E.H., Gobakken, T., Bollandsa˚s, O.M., Zahabu, E., and Næsset,E. (2015). Modeling aboveground biomass in dense tropical submon- tane rainforest using airborne laser scanner data. Remote Sensing, 7(1), 788–807.

Hinsley, S.A., Hill, R.A., Gaveau, D.L.A., and Bellamy, P.E. (2002). Quantifying woodland structure and habitat quality for birds using airborne laser scanning. Functional Ecology, 16(6), 851–857.

Hu, B., Li, J., Jing, L., and Judah, A. (2014). Improving the efficiency and accuracy of individual tree crown delineation from high-density lidar data. International Journal of Applied Earth Observation and Geoinformation, 26,145–155.

Hudak, A.T., Crookston, N.L., Evans, J.S., Falkowski, M.J., Smith, A.M.S., and Gessler, P. (2006). Regression modeling and mapping of coniferous forest basal area and tree density from discrete-return lidar and multispectral satellite data.” Canadian Journal of Re- mote Sensing, 32(2), 126–38.

Hudak, A.T., Crookston, N.L., Evans, J.S, Hall, D.E., and Falkowski, M.J. (2008). Nearest neighbor imputation of species-level, plot-scale forest structure attributes from lidar data. Remote Sensing of Environment, 112(5), 2232–2245.

Hudak, A.T., Evans, J.S., and Smith, A.M.S. (2009). lidar utility for natural resource managers. Remote Sensing, 1(4), 934–951.

Hudak, A.T., Haren, A.T., Crookston, N.L., Liebermann, R.J., and Ohmann, J.L. (2014). Imputing forest structure attributes from stand inventory and remotely sensed data in Western Oregon, USA. Forest Science, 60(2), 253–269.

Hudak, A.T., Strand, E.K., Vierling, L.A., Byrne, J.C., Eitel, J.U.H., Martinuzzi, S., and Falkowski, M.J. (2012). Quantifying above- ground forest carbon pools and fluxes from repeat lidar surveys. Remote Sensing of Environment, 123, 25–40.

Hyyppa, J., Kelle, O., Lehikoinen, M., and Inkinen, M., (2001). A segmentation-based method to retrieve stem volume estimates from 3-D tree height models produced by laser scanners. IEEE Trans- actions on Geoscience and Remote Sensing, 39(5), 969–975.

Isenburg, M. 2015. LAStools—Efficient Tools for lidar Processing, accessed October 3, 2015. <lastools.org>

Jing, L., Hu, B., Li, J., and Noland, T., (2012). Automated delineation of individual tree crowns from lidar data by multi-scale analysis and segmentation. Photogrammetric Engineering & Remote Sensing, 78(12),1 275–1284.

Kankare, V., Liang, X., Vastaranta, M., Yu. X., Holopainen, M., and Hyppa. J. (2015). Diameter distribution estimation with laser scanning based multisource single tree inventory." ISPRS Journal of Photogrammetry and Remote Sensing, 108, 161–171.

Kirkman, L.K., Goebel, P.C., Palik, B.J. and West, L.T. (2004). Predicting plant species diversity in a longleaf pine landscape. Ecoscience, 11(1), 80–93.

Khosravipour, A., Skidmore, A.K., Isenburg, M., Wang, T., and Hussin,Y.A. (2014). Generating pit-free canopy height models from airborne lidar. Photogrammetric Engineering & Remote Sensing, 80(9), 863–872.

Kraus, K., and Pfeifer, N. (1998). Determination of terrain models in wooded areas with airborne laser scanner data. ISPRS Journal of Photogrammetry & Remote Sensing, 53, 193–203.

La¨hivaara, T., Seppa¨nen, A., Kaipio, J.P., Vauhkonen, J., Korhonen, L., Tokola, T., and Maltamo, M. (2014). Bayesian approach to tree detection based on airborne laser scanning data. IEEE Transac- tions on Geoscience and Remote Sensing, 52(5), 2690–2699.

Landers, J.L., Van Lear, D.H., and Boyer, W.D. (1995). The longleaf pine forests of the Southeast: requiem or renaissance? Journal of Forestry. 93(11), 39–44.

Leckie, D., Gougeon, F., Hill, D., Quinn, R., Armstrong, L., and Shree- nan, R. (2003). "Combined high-density lidar and multispectral imagery for individual tree crown analysis." Canadian Journal of Remote Sensing, 29(5), 633–649.

Li, W., Guo, Q., Jakubowski, M.K. and Kelly, M. (2012). A new method for segmenting individual trees from the lidar point cloud. Photogrammetric Engineering & Remote Sensing, Vol. 78(1), 75–84.

Lindberg, E., and Hollaus, M. (2012). Comparison of methods for estimation of stem volume, stem number and basal area from airborne laser scanning data in a hemi-boreal forest. Remote Sensing, 4(4), 1004–1023.

Loudermilk, E.L., Cropper Jr., P., Mitchell, R.J., and Lee, H. (2011). Longleaf pine (Pinus palustris) and hardwood dynamics in a fire- maintained ecosystem: A simulation approach. Ecological Modelling, 222(15), 2733–2750.

Lucas, R., Lee, A., and Williams, M. (2005). The role of lidar data in understanding the relation between forest structure and SAR im- agery. International Geoscience and Remote Sensing Symposium (IGARSS), 3, 2101–2104.

Maltamo, M., Mustonen, K., Hyyppa¨, J., Pitka¨nen, J., and Yu, X. (2004). The accuracy of estimating individual tree variables with airborne laser scanning in a Boreal Nature Reserve." Canadian Journal of Forest Research, 34(9), 1791–1801.

Maltamo, M., Peuhkurinen, J., Malinen, J., Vauhkonen, J., Packale´n, P., and Tokola. P. (2009). Predicting tree attributes and quality char- acteristics of scots pine using airborne laser scanning data. Silva Fennica, 43(3), 507–521.

McGauchey, R.J. (2015). FUSION/LDV: Software for lidar Data Analysis and Visualization. Forest Service Pacific Northwest Research Station USDA, Seattle, accessed Oct.15 2015, <http://http://forsys.cfr.washington.edu/fusion/ FU- SION manual.pdf>.

McRoberts, R.E., Næsset, E., and Gobakken, T. (2015). "Optimizing the k-nearest neighbor technique for estimating forest aboveground biomass using airborne laser scanning data." Remote Sensing of Environment, 163, 13–22.

Nelson, M.D., Healey, S.P., Moser, W.K., Maser, J.G., and Cohen,W.B. (2011). "Consistency of forest presence and biomass predictions modeled across overlapping spatial and temporal extents. Mathe- matical and Computational Forestry & Natural Resource Science, 3(2), 102–113.

Nilsson M. (1996). Estimation of tree heights and stand volume using an airborne lidar system. Remote Sensing of Environment, 56, 1–7.

Oswalt, C.M., Cooper, J.A., Brockway, D.G., Brooks, H.W., Walker, J.L., Connor, K.F., Oswalt, S.N., and Conner, R.C. (2012). History and Current Condition of Longleaf Pine in the Southern United States. Report No. 166. Southern Research Station, Asheville, NC, USA. US Department of Agriculture Forest Service.

Palik, B., Mitchell, R.J., Pecot, S., Battaglia, M., and Pu, M. (2003). Spatial distribution of overstory retention influences resources and growth of longleaf pine seedlings." Ecological Applications, 13, 674–686.

Pang, Y., Lefsky, M., Andersen, H.E., Miller, M.E., Sherrill, K., (2008). Validation of the ICEsat vegetation product using crown-area- weighted mean height derived using crown delineation with dis- crete return lidar data." Canadian Journal of Remote Sensing, 34(2), 471–484.

Popescu, S.C. (2007). Estimating biomass of individual pine trees using airborne lidar. Biomass and Bioenergy, 31(9), 646–655.

Popescu, S.C., Wynne, R.H., and Nelson, R.F. (2003). Measuring indi- vidual tree crown diameter with lidar and assessing its influence on estimating forest volume and biomass. Canadian Journal of Remote Sensing, 29(5), 564–577.

R Core Team. (2015). R: A Language and Environment for Statistical Computing. R Foundation for Statistical Computing, Vienna, Aus- tria, accessed Oct. 15 2015, <http://www.R-project.org≥.

Racine, E.B., Coops, N.C., St-Onge, B., and Begin, J. (2014). Estimating forest stand age from lidar-derived predictors and nearest neighbor imputation. Forest Science, Vol. 60(1), 128–136.

Reitberger, J., Schno¨rr, C.L., Krzystek, P., and Stilla, U. (2009). 3D segmentation of single trees exploiting full waveform lidar data. ISPRS Journal of Photogrammetry and Remote Sensing, 64(6), 561–574.

Robinson, A.P., Duursma, R.A., and Marshall, J.D. (2005). A regression-based equivalence test for model validation: shifting the burden of proof. Tree Physiology, 25, 903–913.

Robinson, A. (2015). Equivalence: Provides Tests and Graphics for Assessing Tests of Equivalence, version 0.7.0, accessed Oct. 15 2015,<https://cran.r-project.org/web/packages/ equivalence/>.

Saarinen, N., Vastaranta, M., Kankare, V., Tanhuanpaa, T., Holopainen, M., Hyyppa, J., and Hyyppa, H. 2014. Urban tree attribute update using multisource single tree inventory. Forests, 5(5), 1032–052.

Saremi, H., Kumar, L., Stone, C., Melville, G., and Turner, R. (2014). Sub-compartment variation in tree height, stem diameter and stock- ing in a Pinus radiata D. Don plantation examined using airborne lidar data. Remote Sensing, 6(8), 7592–7609.

Shamsoddini, A., Turner, R., and Trinder, J.C. (2013). Improving lidar-based forest structure mapping with crown-level pit re- moval. Journal of Spatial Science, 58, 29–51.

Silva, C.A., Crookston, N.L., Hudak, A.T., and Vierling, L.A. (2015). rLiDAR: An R package for reading, processing and visualizing lidar (Light Detection and Ranging) data, version 0.1, accessed Oct. 15 2015, < http://cran.r-project.org/web/packages/rLiDAR/index.html>.

Silva, C.A., Klauberg, C., Carvalho, S.P.C., Hudak, A.T., and Ro- driguez, L.C.E. (2014). "Mapping aboveground carbon stocks using lidar data in Eucalyptus spp. plantations in the state of Sa˜o Paulo, Brazil." Sciencia Forestalis, Vol. 42: pp. 591–604.

Smith, A.M.S., Falkowskie, M.J., Hudak, A.T., Evans, J.S., Robinson, A.P., and Steele, C.M. (2009). A cross-comparison of field, spectral, and lidar estimates of forest canopy cover. Canadian Journal of Remote Sensing, 35(5), 447–459.

Sokolova, M., Japkowicz, N., and Szpakowicz, S. (2006). Beyond accuracy, F-score and ROC: A family of discriminant measures for perfor- mance evaluation. In Advances in Artificial Intelligence, edited by A. Sattar and B.H. Kang, pp. 1015–102.

Berlin/Heidelberg: Springer. Solberg, S., Næsset, E., and Bollandsas, O.M., (2006). Single tree segmentation using airborne laser scanner data in a structurally heterogeneous spruce forest." Photogrammetry Engineering and Remote Sensing, 72(12), 1369–1378.

Stage, A.R., and Crookston, N.L. (2007). Partitioning error components for accuracy-assessment of near neighbor methods of imputation. Forest Science, 53(1), 62–72.

Vastaranta, M., Saarinen, N., Kankare, V., Holopainen, M., Kaartinen, H., Hyyppa¨, J., Hyyppa¨, H. 2014. Multisource single tree inventory in prediction of tree quality variables and log- ging recoveries." Remote Sensing, 6(4), 3475– 3491.

Vauhkonen, J., Ene, L., Gupta, L., Heinzel, L., Holmgren, J., Pitka˜nen, J., Solberg, J.P.S., et al. (2012). Comparative testing of single-tree detection algorithms under different types of forest. Forestry, 85(1), 27–40.

Vauhkonen, J., Korpela, I., Maltamo, M., and Timo Tokola. (2010). Imputation of single-tree attributes using airborne laser scanning- based height, intensity, and alpha shape metrics. Remote Sensing of Environment, 114(6),1263–76.

Vega, C., Hamrouni, A., Mokhtari, S.E., Morel, J., Bock, J., Renaud, J.P., Bouvier, M., and Durrieu, B. (2014). PTrees: A point-based approach to forest tree extraction from lidar data. International Journal of Applied Earth Observation and Geoinformation, 33, 98–108.

Vierling, K.T., Vierling, L.A., Gould, W.A., Martinuzzi, S., and Clawges, R.M. (2008). Lidar: Shedding new light on habitat charac- terization and modeling. Frontiers in Ecology and the Environment, 6(2), 90–98.

Waske, B., Benediktsson, J.A., and Sveinsson, J.R. (2012). Random forest classification of remote sensing data. In Signal and Image Processing for Remote Sensing, edited by C.H. Chen, pp. 365–374. Abingdon, UK: CRC Press, Taylor & Francis Group.

Weinacker, H., Koch, B., Heyder, U., and Weinacker, R. (2004). Development of filtering, segmentation and modelling modules for LI- DAR and multispectral data as a fundamental of an automatic forest inventory system. Photogrammetry, Remote Sensing and Spatial Information Sciences. 36(8), 50–55.

Wing, M.G., Eklund, A., Sessions, J., and Karsky, R. (2008). Horizontal measurement performance of five mapping-grade GPS receiver con- figurations in several forested settings. Western Journal of Applied Forestry, 23(3), 166–171.

Wulder, M., Niemann, K.O., and Goodenough, D.G. (2000). Local maximum filtering for the extraction of tree locations and basal area from high spatial resolution imagery." Remote Sensing of Environment, 73(1), 103–114.

Yao, W., Krzystek, P., and Heurich, M. (2013). Enhanced detection of 3D individual trees in forested areas using airborne full-waveform lidar data by combining normalized cuts with spatial density clus- tering. ISPRS Annals of Photogrammetry, Remote Sensing and Spa- tial Information Sciences, Vol. II-5/W2. 349–354.

Table 1.1. Statistical summary of tree measurements attributes at the sample plots

Stand	Nº Plots	Tree Density (N/ha)				DBH (cm)				Ht (m)			
		min	max	mean	sd	min	max	mean	Sd	min	max	mean	sd
NE	7	201	204	202	2	10.00	60.00	30.66	12.11	6.20	31.40	23.01	5.12
CNT	6	126	194	147	25	10.00	74.60	33.21	13.77	6.10	33.30	23.24	4.77
NW	2	77	203	131	61	9.50	71.30	36.29	14.02	8.50	32.10	22.75	4.75

Table 1.2. Statistical summaries of tree basal area (BA) and stem volume (V) at sample plots

Stand	BA (m^2/Tree)				V (m^3/tree)			
	min	max	mean	sd	min	max	Mean	sd
NW	0.01	0.40	0.12	0.08	0.04	2.44	0.94	0.47
CNT	0.01	0.44	0.10	0.07	0.01	2.73	1.01	0.50
NE	0.01	0.28	0.09	0.06	0.01	2.28	0.99	0.52

Table 1.3. Lidar flight parameters

LIDAR Survey Parameters	
Scan Frequency	45 Hz
Scan Angle	+/- 20 deg
Scan Cutoff	+/- 4.0 deg
Scan Offset	0 deg
System PRF	125 kHz
Swath Width	344.64 m
Flying Altitude	600m AGL
Down Track Resolution	0.75 m
Points per square meter	5.06
Horizontal Datum	NAD83
Vertical Datum	NAVD88 (GEOID 03)
Projection	UTM Zone 16N

Table 1.4. Individual tree detection in the test subplots. The highlighted gray color represents the best results, which were determined by comparing the number of trees detected (NTD) to the field-based tree inventory number (N). The closest values of NTD compared with N were selected as the best results.

Plots	Stand	COV	Ref. (N)	TWS								
				3x3			5x5			7x7		
					SWS			SWS			SWS	
				NF	3x3	5x5	NF	3x3	5x5	NF	3x3	5x5
1	NW	68.39	803	4675	1112	587	1246	702	478	620	507	413
2		75.63	815	4725	1156	586	1312	674	480	639	514	410
3	CNT	70.40	519	4063	893	467	1028	515	393	485	399	340
4		70.96	503	4346	939	490	1079	548	410	526	425	370
5		71.47	572	4256	1021	536	1131	632	437	570	467	381
6		72.62	543	4208	953	505	1096	584	426	550	440	385
7		73.17	777	4222	1052	577	1110	622	449	552	452	383
8		75.53	621	4723	1050	573	1221	620	465	609	483	410
9	NE	60.13	321	2994	684	346	750	373	272	344	275	243
10		61.75	306	3222	701	363	771	414	283	374	300	250
11		63.85	366	3366	750	393	852	427	319	414	323	292
12		63.96	338	3319	743	370	849	396	292	411	318	265
13		72.24	737	4006	940	510	1018	563	405	521	436	368
14		74.50	810	4379	1012	547	1119	612	437	530	463	385
15		75.56	797	4357	1023	561	1145	620	452	567	454	391

Ref.: reference number of tree per test plot (N); TWS: fixed treetop windows size; SWS: fixed smoothing windows size; NF: no filter applied; NE: Northeast stand; CNT: Central stand and NW: Northwest stand.

Table 1.5. Accuracy assessment results of lidar-based individual tree detection according to recall (r), precision (p) and F-score (F) statistics parameters.

Subplots	COV (%)	Number of Trees Detected (NTD)					r	p	F
		lidar	Reference	FP	FN	TP			
1	46.21	13	16	1	4	12	0.75	0.92	0.83
2	46.87	16	18	2	4	14	0.78	0.88	0.82
3	50.66	8	6	2	0	6	1.00	0.75	0.86
4	56.55	5	5	0	0	5	1.00	1.00	1.00
5	60.31	4	4	0	0	4	1.00	1.00	1.00
6	63.02	4	4	0	0	4	1.00	1.00	1.00
7	64.71	9	8	1	0	8	1.00	0.89	0.94
8	67.13	7	5	2	0	5	1.00	0.71	0.83
9	71.41	16	17	3	4	13	0.76	0.81	0.79
10	71.45	18	21	2	5	16	0.76	0.89	0.82
11	74.33	20	23	4	7	16	0.70	0.80	0.74
12	76.93	11	10	2	1	9	0.90	0.82	0.86
13	80.56	23	27	3	7	20	0.74	0.87	0.80
14	85.58	15	13	3	1	12	0.92	0.80	0.86
15	83.48	8	8	1	1	7	0.88	0.88	0.88
Overall	66.41	177	185	26	34	151	0.82	0.85	0.83

Table 1.6. Accuracy assessment results for the individual tree detection as a function of lidar-derived COV. FP: False positive; FN: False negative; TP: True positive; r: recall; p: precision and F: F-score.

COV (%)	Number of Trees Detected (NTD)					r	p	F
	lidar	Reference	FP	FN	TP			
≤ 70	60	53	9 (17.0)	2 (3.8)	51 (96.2)	0.96	0.85	0.90
>70	117	132	17 (12.9)	32 (24.2)	100 (75.8)	0.76	0.85	0.80
Overall	177	185	26 (14.1)	34 (18.1)	151 (81.6)	0.82	0.85	0.83

Table 1.7. Estimated tree attributes summarized at the stand-level.

		Ht (m)		BA (m^2)			V (m^3)		
Stands	NTD	Mean	Sd	Mean	Sd	Total	Mean	Sd	Total
NW	36958	23.17	4.14	0.10	0.07	3824.11	0.96	0.40	35658.33
CNT	52184	21.26	5.34	0.09	0.07	4478.04	0.80	0.49	42114.29
NE	35980	21.10	5.42	0.09	0.07	3119.95	0.79	0.49	28564.40

NTD=Number of Trees Detected

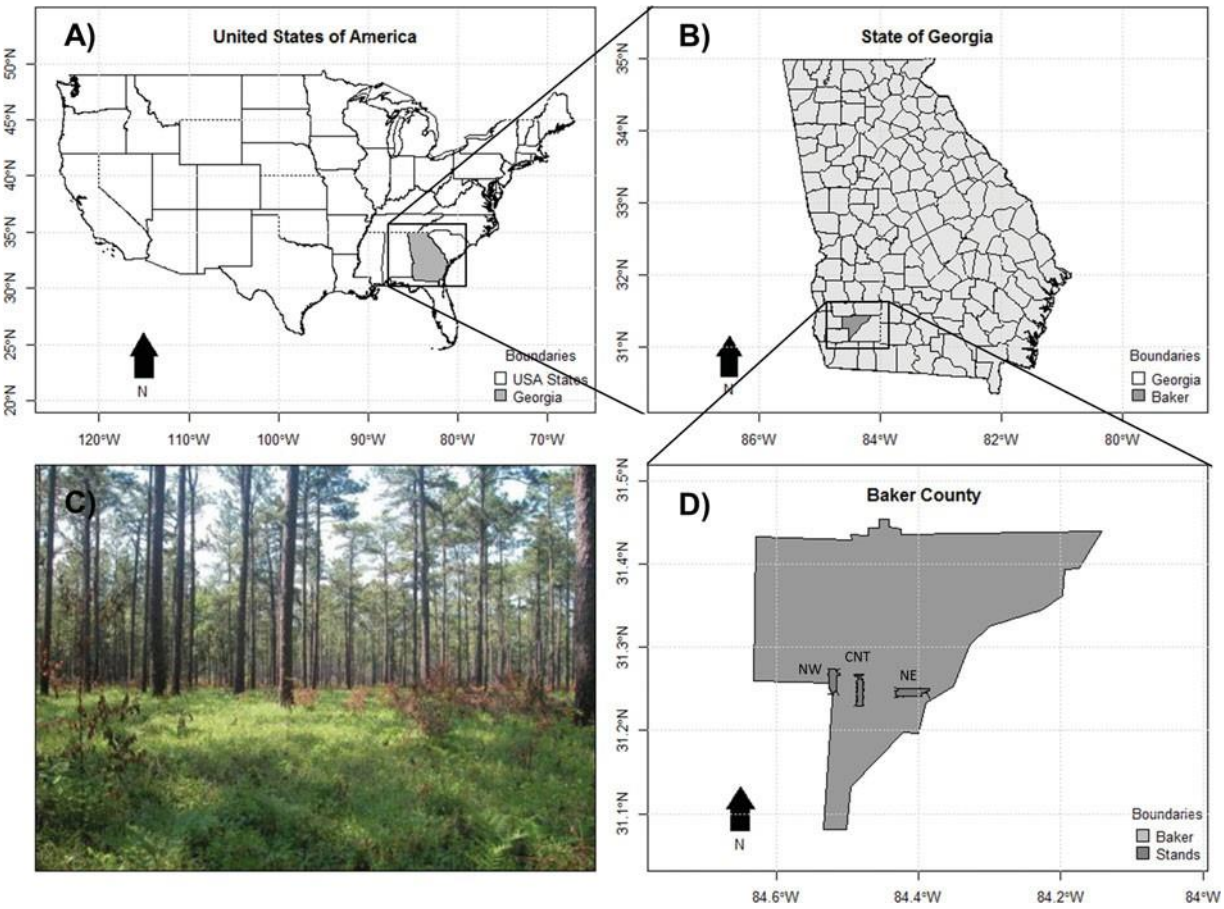

Figure 1.1. Longleaf pine forest location: A, B, and D, and profile picture at Ichauway in southwestern Georgia, USA. NW: Northwest; CNT: central and NE: Northeast stands.

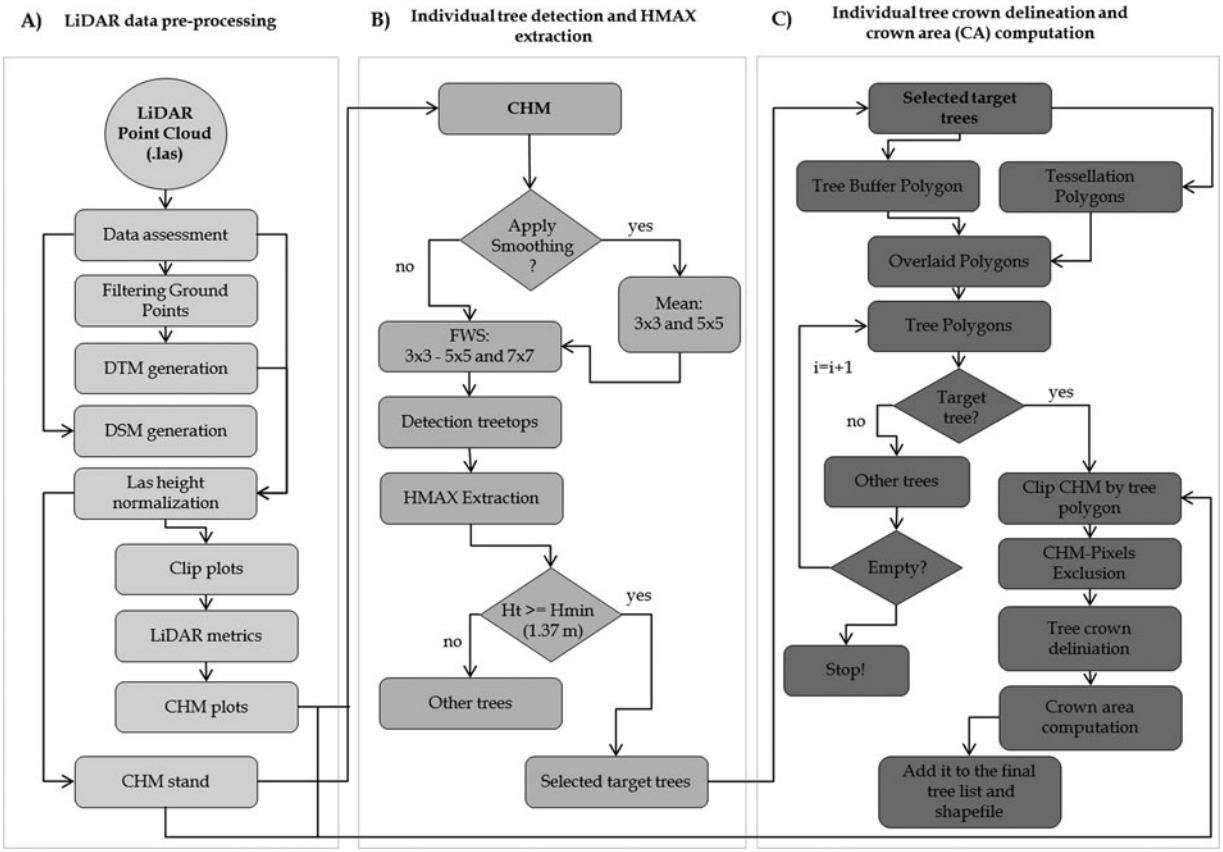

Figure 1.2. Flowchart of the lidar data processing.

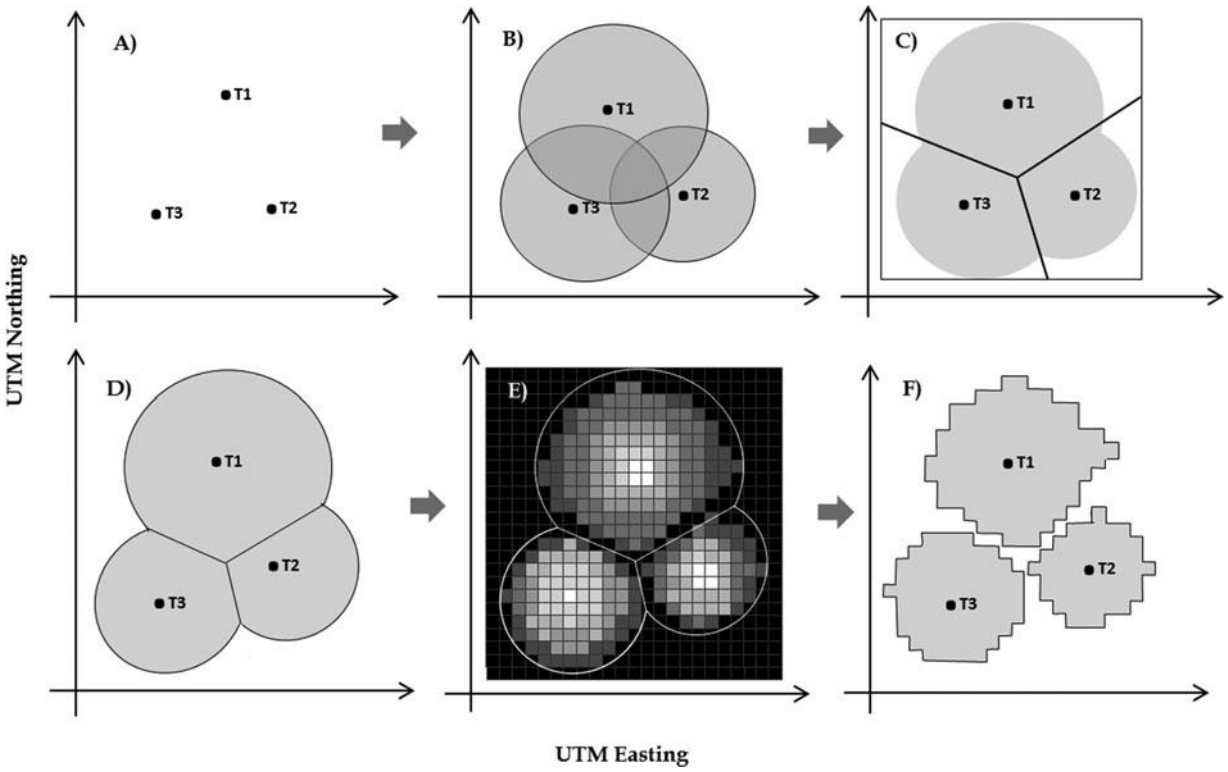

Figure 1.3. Illustration of the individual tree crown delineation algorithm. T=trees. (A) treetops; (B) buffer earch area of 10 m maximum radius; (C) Centroidal Voronoi Tessellation delineation; (D) buffer and Centroidal Voronoi Tessellation are overlaid (E) CHM clipping; (F) crown delineation.

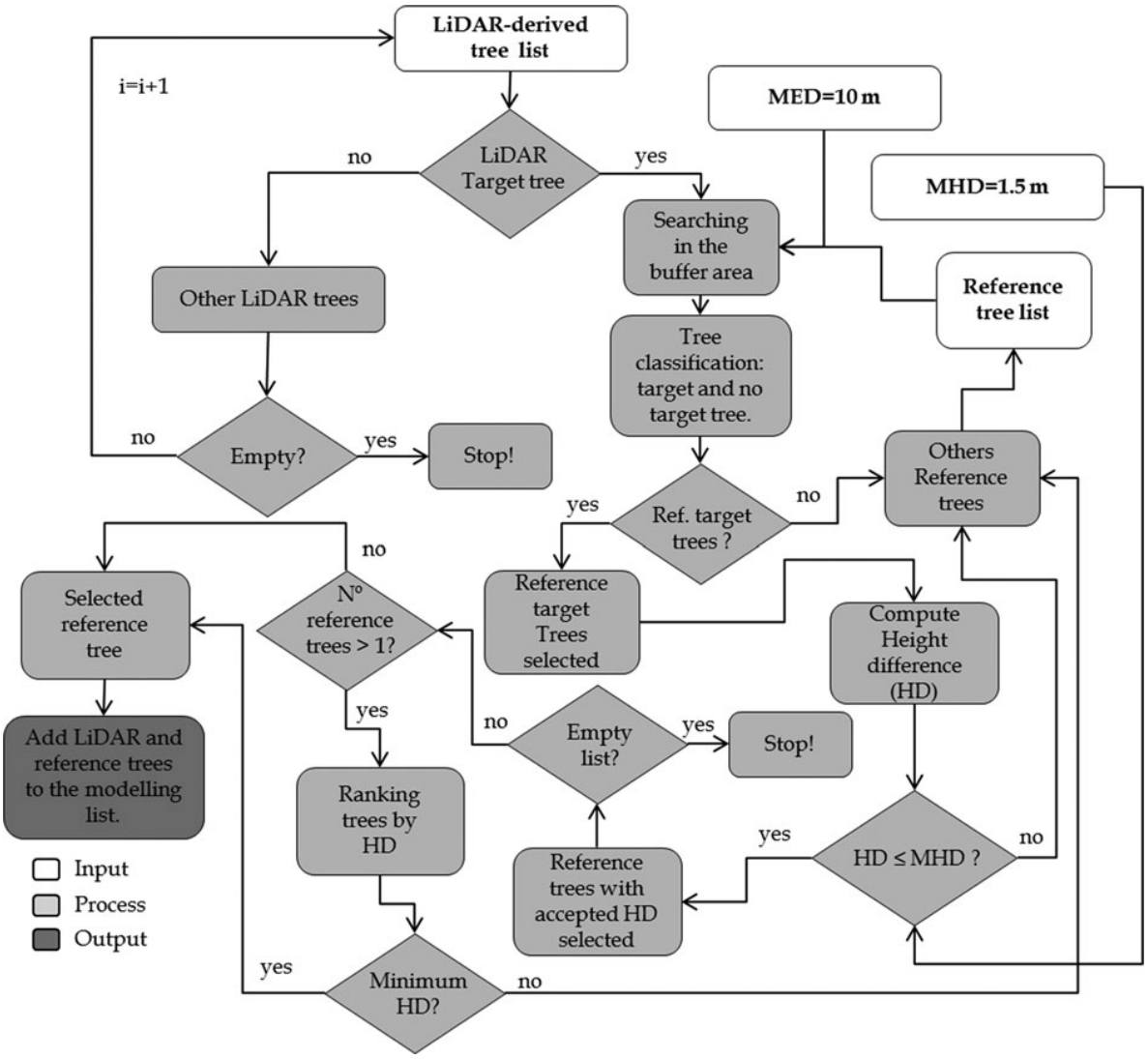

Figure 1.4. rSTree algorithm: searching for the lidar and reference trees. MED = maximum Euclidian distance, MHD = minimum height deference, HD = height difference.

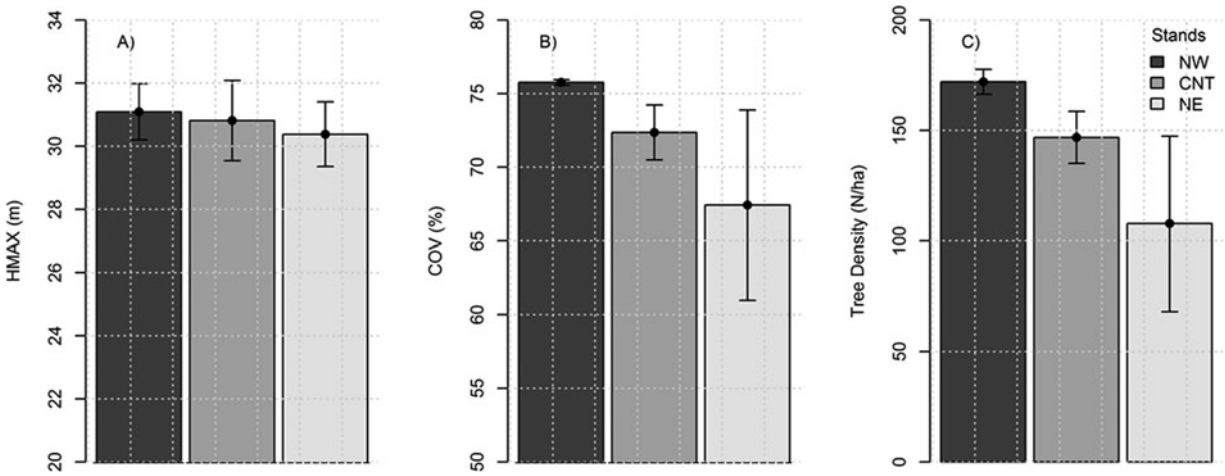

Figure 1.5. Lidar-based plot (A) HMAX and (B) COV; and (C) tree density measured in the field at the longleaf pine test plots. Error bars indicate standard deviations.

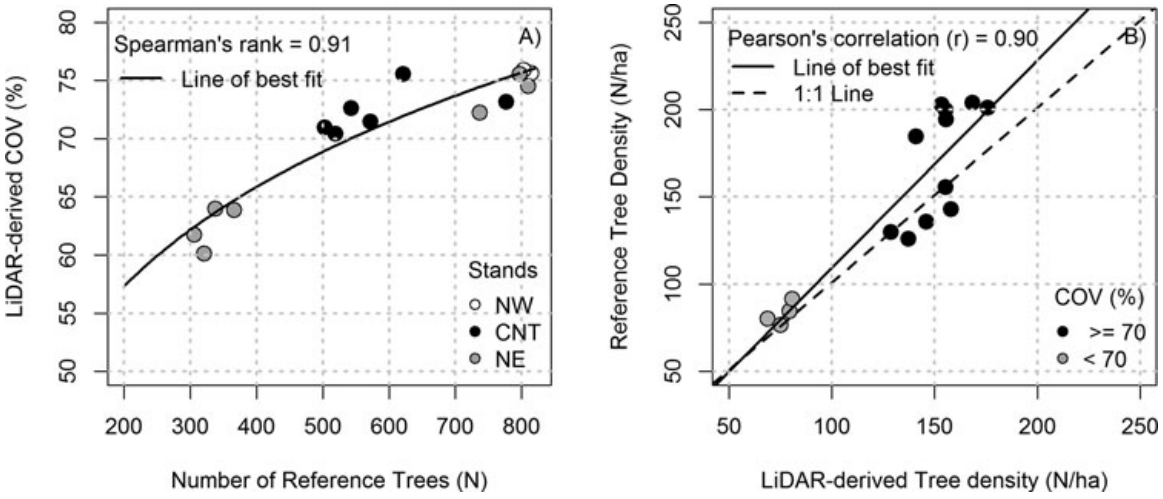

Figure 1.6. Lidar-derived COV versus number of reference trees (N) measured in the field (A), and lidar-derived versus reference tree densities.

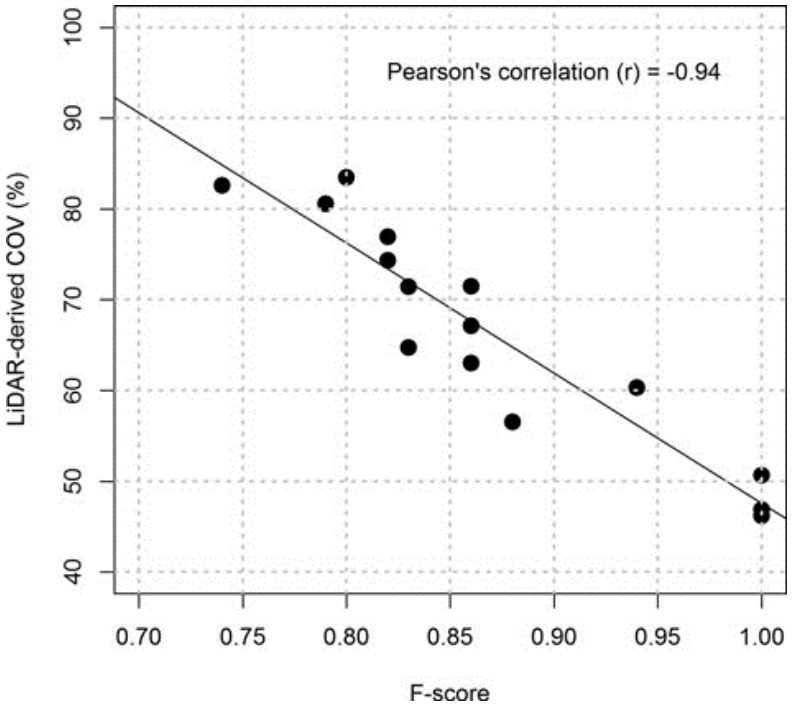

Figure 1.7. Relationship between lidar-derived COV and F-score in the 15 test subplots.

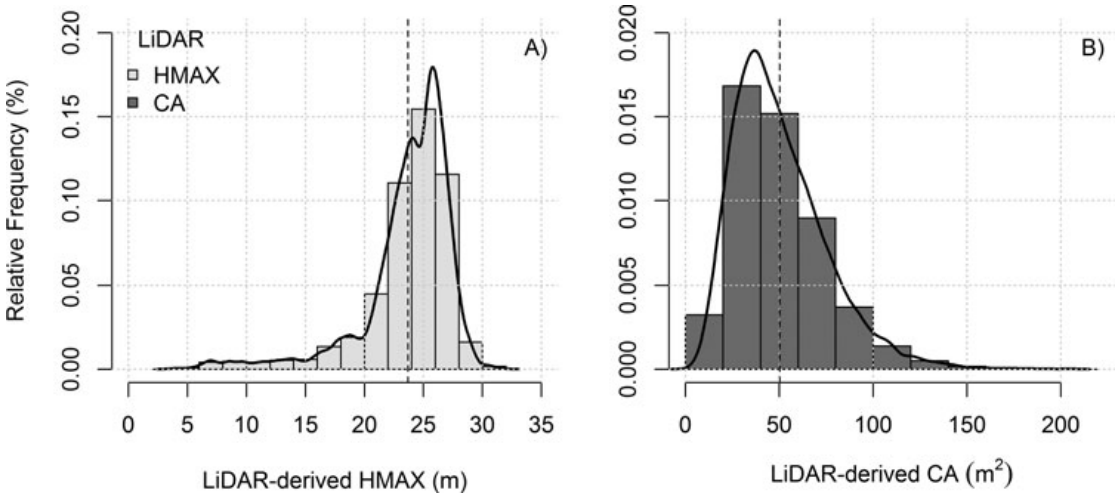

Figure 1.8. Distribution of lidar-derived (A) HMAX and (B) CA values. The black line represents a fitted distribution.

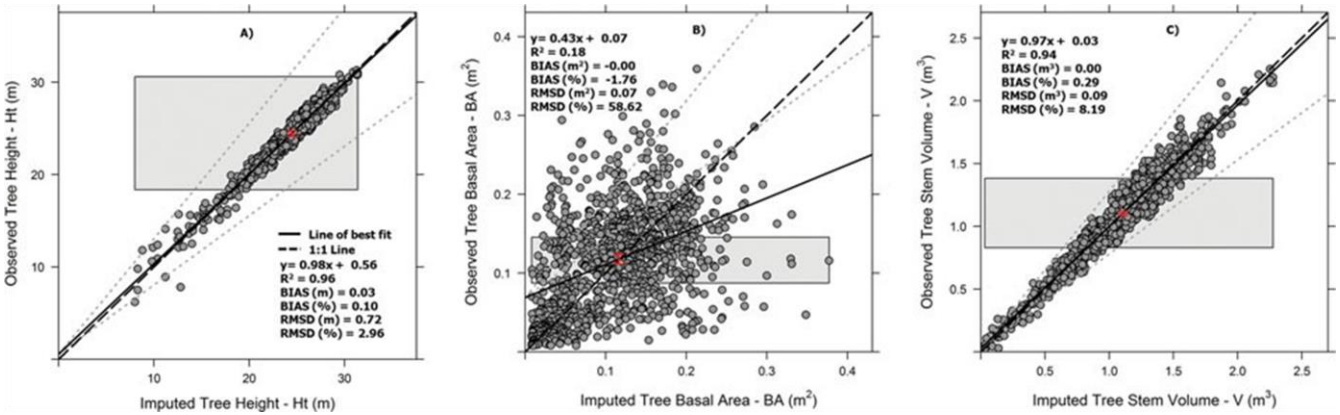

Figure 1.9. Equivalence test graphs for the imputed and observed longleaf pine tree attributes. (A) Tree Height Ht (m); (B) Tree Basal Area - BA (m^2); (C) Tree Stem Volume - V (m^3), N 1061. The equivalence plots design presented herein are an adaptation of the original equivalence plots presented by Robinson (2015). The grey polygon represents the 25% region of equivalence for the intercept, and the red vertical bar represents a 95% confidence interval for the intercept. The imputed tree attributes are equivalent to the reference attributes when the red bar is completely within the grey polygon. If the grey polygon is lower than the red vertical bar, the imputed attributes are biased low; if it is higher than the red vertical bar, the imputed forest attributes are biased high. The grey dashed line represents the 25% region of equivalence for the slope, and the red vertical bar is contained completely within the grey dashed line, the pairwise measurements are equal. A bar that is wider than the region outlined by the grey dashed lines indicates highly variable predictions. The gray dots are the pairwise measurements, and the solid line is a best-fit linear model for the pairwise measurements. The black dashed line represents the 1:1 line.

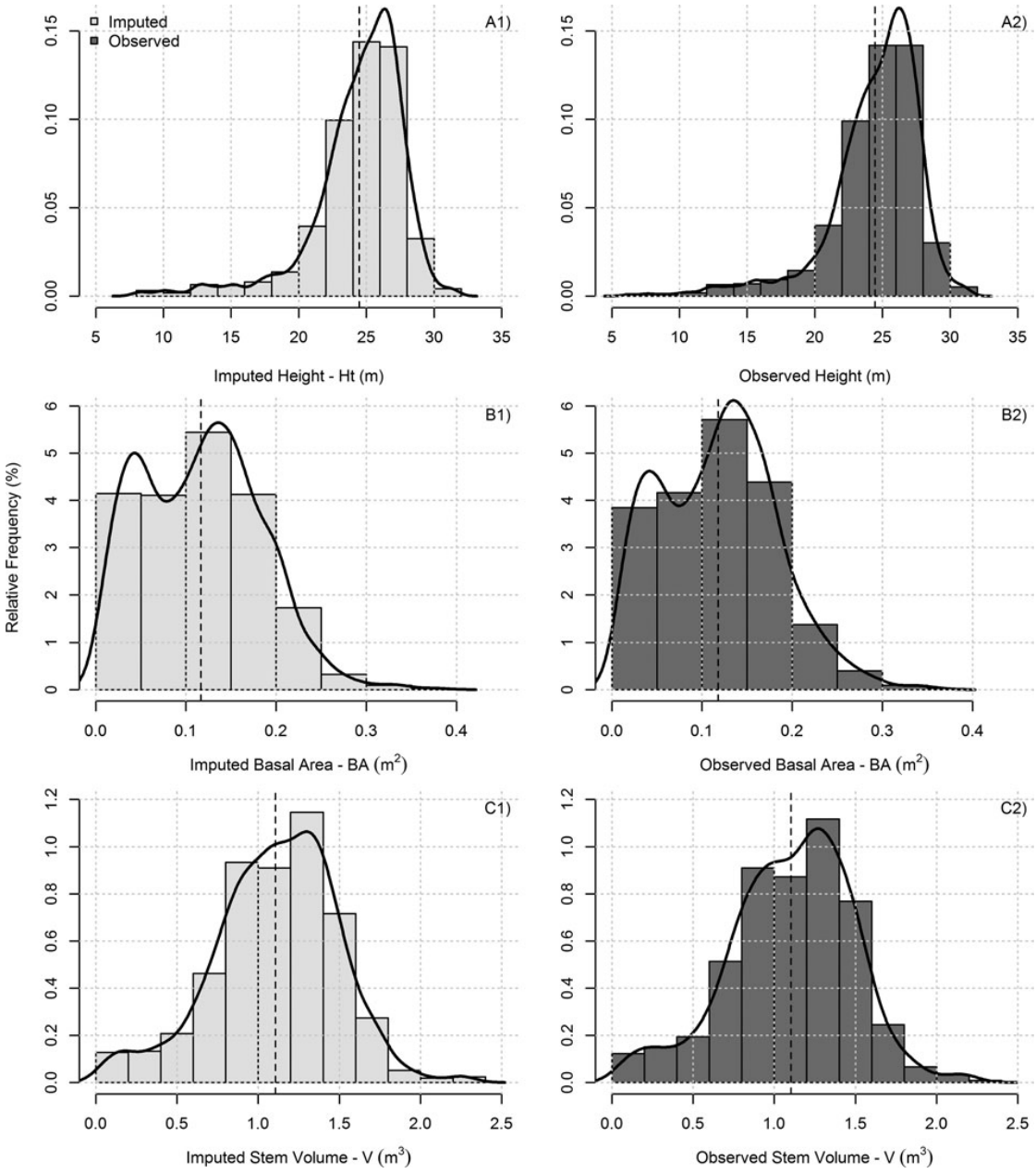

Figure 1.10. Imputed and observed tree attributes distribution from the testing dataset. (A), (B) and (C) represent Ht, BA, and V distribution across the 3 stands. The numbers 1 and 2 represent the imputed and observed values. The black line represents a fitted distribution, and the dashed vertical line represents the mean.

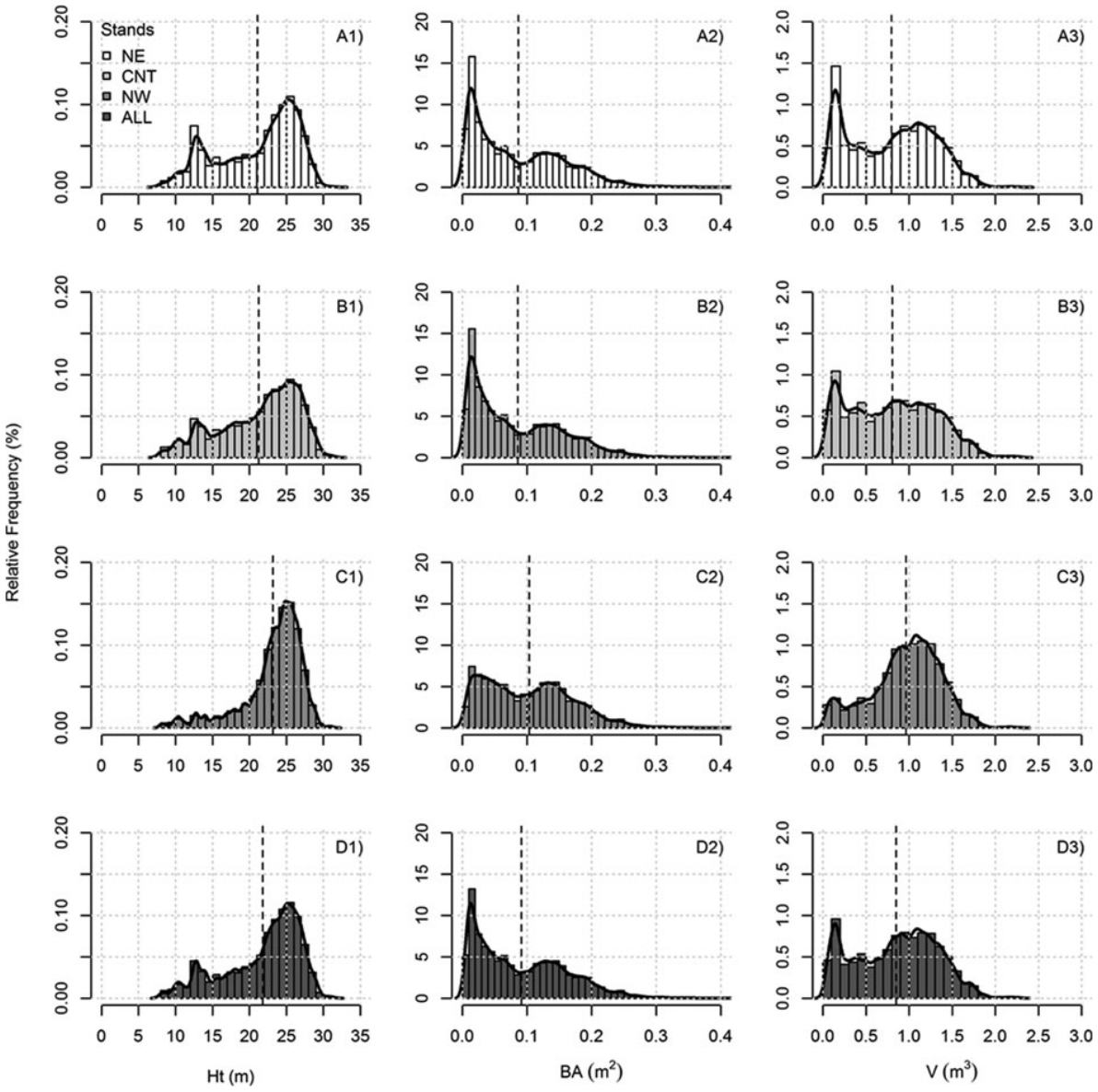

Figure 1.11. Distribution of imputed tree attributes (Ht, BA, and V) across the 3 stands in the study area. The numbers from 1 to 3 represent the attributes Ht, BA, and V, respectively. The letters from (A) to (D) represent the NE, CNT, and NW, and all stands, respectively. The black line represents a fitted distribution and the dashed vertical line represents the mean.

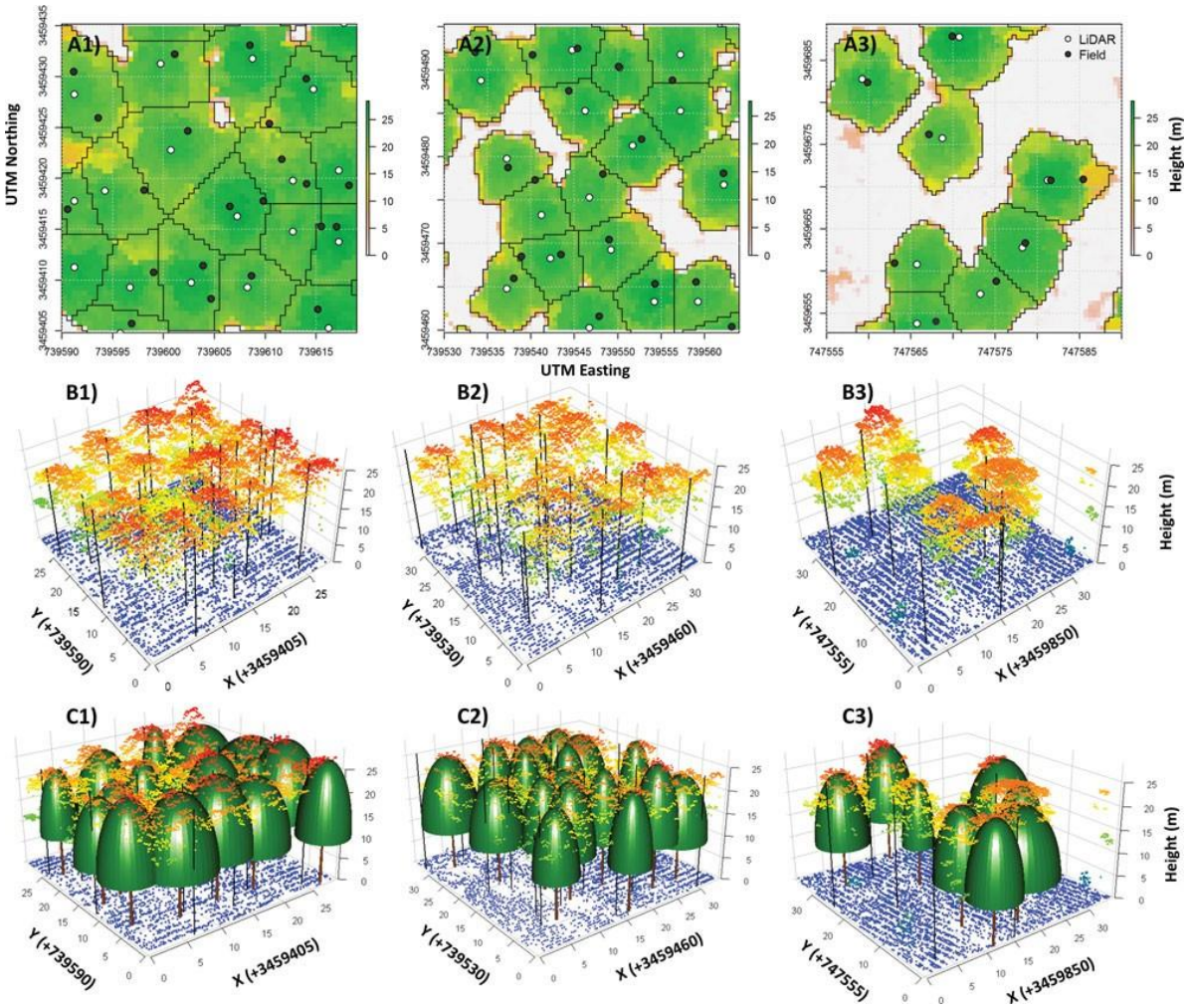

Figure 1.12. Illustration of individual tree detection and crown delineation under different COV conditions. (1) COV= 90.96%; (2) COV= 76.79%, and (3) COV= 58.66%. (A) 2D visualization of the tree location and crown delineation over the CHM. (B) 3D visualization of the lidar point cloud and reference trees measured in the field. (C) 3D visualization of the lidar virtual forest, and the reference tree locations.

Chapter 2. Predicting Stem Total and Assortment Volumes in an Industrial *Pinus taeda* L. Forest Plantation Using Airborne Laser Scanning Data and Random Forest

Silva, C.A.; Klauberg, C.; Hudak, A.T.; Vierling, L.A.; Jaafar, W.S.W.M.; Mohan, M.; Garcia, M.; Ferraz, A.; Cardil, A.; Saatchi, S. Predicting Stem Total and Assortment Volumes in an Industrial Pinus taeda L. Forest Plantation Using Airborne Laser Scanning Data and Random Forest. Forests 2017, 8, 254.

Abstract

Improvements in the management of pine plantations result in multiple industrial and environmental benefits. Remote sensing techniques can dramatically increase the efficiency of plantation management by reducing or replacing time-consuming field sampling. We tested the utility and accuracy of combining field and airborne lidar data with Random Forest, a supervised machine learning algorithm, to estimate stem total and assortment (commercial and pulpwood) volumes in an industrial *Pinus taeda* L. forest plantation in southern Brazil. Random Forest was populated using field and lidar-derived forest metrics from 50 sample plots with trees ranging from three to nine years old. We found that a model defined as a function of only two metrics (height of the top of the canopy and the skewness of the vertical distribution of lidar points) has a very strong and unbiased predictive power. We found that predictions of total, commercial, and pulp volume, respectively, showed an adjusted R^2 equal to 0.98, 0.98 and 0.96, with unbiased predictions of −0.17%, −0.12% and −0.23%, and Root Mean Square Error (RMSE) values of 7.83%, 7.71% and 8.63%. Our methodology makes use of commercially available airborne lidar and widely used mathematical tools to provide solutions for increasing the industry efficiency in monitoring and managing wood volume.

Keywords: forest inventory; lidar; remote sensing; supply chain

2.1 Introduction

The area of planted forests worldwide has been steadily growing, with an estimated 6.95% of total global forested area being plantations in 2010 (Payn et al., 2015). Tropical regions may be experiencing particularly rapid rates of plantation expansion (Iba, 2016). For example, the area of pine plantations in Brazil has dramatically risen in the last few decades to increase pulp and paper production. Currently ~20% of the total reforested area of Brazil is comprised of pine forest plantations (Khler et al., 2014).

Most of the pine plantations are concentrated in South Brazil, with 34.1% and 42.4% of the total reforested area located in Paraná and Santa Catarina states (Iba, 2016). *Pinus taeda* L., also known as loblolly pine, is the most planted forest specie in these regions. It has high economic importance due to its high volumetric increment in the colder regions of the southern Brazil (Kohler et al., 2014). It has fast growing rates presenting increments up to 50 $m^3 \cdot ha^{-1} \cdot year^{-1}$(Iba, 2016). Moreover, *P. taeda* is commonly managed for production of multiple types of wood such as stem total, saw logs, pulpwood and small-diameter logs and branches, which are used for energy. Saw logs and pulpwood can be further divided into different assortments that differ in size and therefore in economic value (Kohler et al., 2014).

Forest inventory in *P. taeda* is currently based on field measurements and typically conducted annually to monitor forest growth in Brazil, allowing managers to identify problematic conditions during initial growth stages, and determine optimal harvest time (Silva et al., 2017a). While field measurements are considered the most accurate approach for monitoring industrial forest plantations, measuring stem total and assortment volumes annually via traditional methods is an extremely time consuming and labor-intensive task, especially in large plantations where a huge number of plots need to be measured to characterize the variation (Silva et al., 2016). Hence, to improve plantation management there is a need to develop and implement accurate, repeatable, and economical remote sensing based methods that provide synoptic coverage at high spatial resolution.

Over the past few decades, lidar remote sensing has been established as one of the promising and primary tools for broad-scale analysis of forest systems. Lidar data can be used to characterize local to regional spatial extents with high enough resolution to quantify

the three-dimensional structure of the forest with the support of efficiently collected field data and several statistical methods (e.g., Næsset 1997; Næsset 2002; Næsset et al., 2007; Hudak et al., 2009). Lidar can be used to produce highly accurate retrievals of tree density, stem total and assortment volumes, basal area, aboveground carbon, and leaf area index, and thereby can be an effective way to predict and map forest attributes at unsampled locations (e.g., Andersen et al., 2005; Hudak et al., 2006; White et al., 2014; Silva et al., 2014; Korhonen et al., 2008; Peuhkurinen et al., 2008). To parlay these attributes into improved forest management practices for wood and pulp production, it is often necessary to predict stem total and assortment volumes of pine plantations in operational and experimental scenarios, as these scenarios often include thinning cruises, mid-rotation cruises, genetic trials, and silviculture research tests (Sherrill et al., 2011).

Current predictive modeling methods include parametric (e.g., multiple linear regression) and non-parametric (e.g., Random Forest) approaches (e.g., Næsset 1997; Næsset 2002; Hudak et al., 2008). Among the machine learning algorithms, the Random Forest (RF) modeling approach has gained popularity in estimating forest attributes from lidar data due to its flexibility and ability to maintain nonlinear dependences compared to parametric algorithms (Ahmed et al. 2005). The RF can be viewed as an improved version of classification and regression tree (CART) methods; data and variables can be randomly sampled by RF in an iterative bagging bootstrap procedure to generate a “forest” of regression trees (Breiman 2001). Also, incorporation of multiple decision trees and internal cross-validation has improved results, enhanced ease of use and reduced issues regarding over-fitting while performing this modeling approach (Grossmann et al, 2010; Naidoo et al., 2012). In case of regression-type problems, RF acts as an arbitrary number of simple trees whose responses are averaged to obtain an estimate of dependent variables (Yu et al., 2011). Diversification of sample trees is primarily done in two ways, either through a balancing methodology where equal numbers of samples are drawn from minority classes and majority classes, or by assigning a higher weight (i.e., heavier penalty) on misclassified minority class and taking the majority voting of individual classification trees (Ko et al., 2016). As RF does not require any assumptions about the relationships between explanatory and response variables, they are considered well suited for analyzing complex non-linear and

possibly hierarchical interactions in large datasets (Olden et al., 2008). In forest inventory, RF has been used for predicting and mapping forest attribute at the stand (e.g., Ahmed et al., 2015) and individual tree levels (Yu et al., 2011), in addition to disturbance evaluation (e.g., Stumpf et al., 2011), mapping invasive plant species (e.g., Lawerence et al., 2006), and vegetation classification (e.g., Grossmann et al., 2010). Despite of the above-mentioned studies, to our knowledge, lidar and RF have been not yet being combined for predicting and mapping stem total, saw log and pulpwood volumes in industrial *P. taeda* forest plantations at stand level.

Timely monitoring of stem total and assortment volumes in *P. taeda* plantations with lidar data and RF would allow managers to determine the optimal time for harvest or other treatment activities to maximize economic return. Therefore, the development of robust frameworks for modeling and mapping stem total and assortment volumes at plot and stand levels is still needed to increase the efficiency in monitoring and managing wood and pulp productions in forest plantations. Moreover, efficient frameworks also play important role in helping lidar technology move from research to operational modes, especially in industrial forest plantation settings where lidar applications are relatively new. The aims of this study were to: (i) present a robust and efficient framework for modeling, predicting and mapping stem total volume (Vt), saw logs (in this study mentioned as commercial) volume (Vc) and pulpwood volume (Vp) in a *P. taeda* plantation in southern Brazil using airborne lidar data; (ii) evaluate the use of the RF machine learning algorithm for modeling stem total and assortment volumes; and (iii) generate maps representing the spatial distribution of Vt, Vc and Vp in differently aged plantations of *P. taeda*.

2.2 Material and methods

2.2.1 Study Area Description

The study area consisted of *P. taeda* stands located within the Telêmaco Borba municipality in the state of Paraná, southern of Brazil (Figure 2.1). Trees were planted using a 3.0 × 2.0 m or 2.5 × 2.5 m grid configuration, resulting in an average tree density of 1667 or 2000 tree·ha^{-1}, respectively. The climate of the region is characterized as warm and temperate (Köppen 1928), with annual average precipitation of approximately 1378 mm and

an annual average temperature of 18.4 °C. The *P. taeda* stands are situated on a plateau where the topography is relatively flat. The plantations are managed by Klabin S.A., a pulp and paper company.

2.2.2 Field Data Collection

A total of 50 rectangular plots, each approximately 600 m^2 (i.e., 20 m × 30 m) were randomly established and measured across 50 stands distributed in four plantations. As such, the sample plots well represent the study area, and they capture the entire structural variability in these stands with ages ranging from three to nine years old. All plots were geo-referenced with a geodetic GPS with differential correction capability (Trimble Pro-XR, Trimble, Sunnyvale, CA, USA) ensuring a location error lower than 10 cm. In each sample plot, individual trees were measured for dbh (diameter at breast height) at 1.30 m and a random subsample (15%) of trees for tree height (Ht). For those trees in the plots that were not directly measured for Ht, the inventory team of Klabin S.A. predicted heights from hypsometric equations (Curtis 1967), employing dbh as the independent variable, and Ht as the dependent variable, following the model below:

$$\ln(\mathrm{Ht}) = \beta_0 + \beta_1 \times (1/\mathrm{dbh}) + \mathrm{e} \qquad (2.1)$$

where ln(Ht) is the natural logarithm of tree height (m); β_0 and $\beta_1$are the intercept and the slope of the model; dbh is the diameter at breast height (1.30 m) and e is the random error of the model. The coefficients of the hypsometric models are the company's intellectual property and not made available to the public, however, the adjusted coefficient of determination (adj.R^2) and standard error of estimate in percentage (SEE%) of the models ranged from 0.96 to 0.98 and 5.1 to 6.5, respectively.

The management goal of the *P. taeda* plantations at Klabin is optimized to produce commercial logs of 2.65 m in length, which are then classified in four timber assortment classes: 18 to 25 cm (Vc 1), 25 to 30 cm (Vc 2), 30 to 40 cm (Vc 3), and diameter ≥ 40 cm (Vc 4). The logs designated for pulpwood are produced with log lengths of 2.40 m and diameters ranging from 8 to 18 cm (Vp), as illustrated in Figure 2.2.

In this study, Vt, Vc and Vp for each tree were computed using the fifth-degree polynomial (Schöpfer 1966) as presented below:

$$\frac{d_i}{dbh} = \left[\beta_0 + \beta_1\left(\frac{h_i}{h}\right) + \beta_2\left(\frac{h_i}{h}\right)^2 + \beta_3\left(\frac{h_i}{h}\right)^3 + \beta_4\left(\frac{h_i}{h}\right)^4 + \beta_5\left(\frac{h_i}{h}\right)^5\right] \quad (2)$$

$$V = K\int_{h_1}^{h_2} d_i^2 \delta h \quad (3)$$

$$V = K\, dbh^2 \int_{h_1}^{h_2} (\beta_0 + \beta_1/h \times h_1^1 + \beta_2/h^2 \times h_2^2 + \beta_3/h^3 \times h_2^3 + \beta_4/h^4 \times h_2^4 + \beta_5/h^5 \times h_2^5)^2 \delta h \quad (4)$$

where $\beta =$ parameters to be estimated; d_i = stem diameter (cm) at the ith position; dbh = diameter (cm) at breast height (1.30 m); h = total height (m); h_i = height (m) at the ith position; and K = π/40,000 is an adjustment factor to estimate volume as $m^3 \cdot ha^{-1}$.

The polynomial models were adjusted for classes of dbh, and the coefficients of the models are the companies' intellectual property and not made available to the public; however, the classes of diameter, adj.R^2 and standard error of the estimate (SEE; given in %) for the polynomial models used in this study are presented in Table 2.1.

The total of Vt, Vc and Vp of all individuals were summed at plot-level and scaled to a hectare. The summary of volumes in $m^3 \cdot ha^{-1}$ for each class of stand ages is presented in Table 2.2. SEE (%) is the standard error of the estimate, expressed as a percentage.

2.2.3 Lidar Data Acquisition and Data Processing

Lidar data were obtained by a Harrier 68i sensor (Trimble, Sunnyvale, CA, USA) mounted on a CESSNA 206 aircraft. The characteristics of the lidar data acquisition are listed in Table 2.3. Lidar data processing consisted of several steps that ingested the lidar point cloud data and provided two major outputs: the digital terrain model (DTM), and the lidar-derived canopy structure metrics. All lidar processing was performed using FUSION/LDV 3.42 software (US Forest Service, Washington, DC, USA) (McGauchey, 2015).

The original point cloud data were filtered using Kraus and Pfeifer's algorithm (Kraus 1998) and a 1 m resolution DTM was generated from the points classified as ground. Subsequently, the height of the returns was computed by subtracting the elevation of the DTM from each return. Once the heights were normalized, the metrics shown in Table 2.4 were computed at plot and stand levels, at a grid cell resolution of 25 m, using all lidar returns.

2.2.4. Predictor Variables Selection

In order to derived accurate estimates of stem volumes from lidar, it is essential to select the most significant lidar metrics (predictor variables) for modeling within a parsimonious statistical model framework. Because the number of candidate lidar metrics can be very large (e.g., 30 metrics), in our study we selected the best lidar metrics for modeling stem volumes based on two steps. First, even though highly correlated variables will not cause multi-collinearity issues in RF, Pearson's correlation (r) was used to identify highly correlated predictor variables ($r > 0.9$) as presented in previous studies (e.g., Hudak et al., 2012; Silva et al., 2016). If a given group (2 or more) of lidar metrics were highly correlated, we retained only one metric by excluding the others that were most highly correlated with the remaining metrics. Second, we identified the most important metrics based on the Model Improvement Ratio (MIR), a standardized measure of variable importance (Evans et al., 2009; Evans et al., 2010). MIR scores are derived by dividing raw variable important scores (output from RF models) by the maximum variable importance score, so that MIR values range from 0 to 1. MIR scores allow for variable importance comparisons among different RF models. We ran the RF routine (package randomForest, Liaw 2015) in R (R Core Team 2015) 1000 times to compute MIR. In each MIR iteration, we bootstrapped the data by randomly selecting a sample of 50 plots with replacement. RF requires two parameters to be set: (i) mtry, the number of predictor variables performing the data partitioning at each node which in this study was defined by the number of highly uncorrelated preliminary set of lidar metrics and (ii) ntree, the total number of trees to be grown in the model run which was set to 1000 (e.g., Bright et al., 2013). Running 1000 iterations of RF produced consistent MIR distributions and avoided unnecessary processing time (Bright et al., 2013). To create

parsimonious models, we reserved the metrics for final RF models that exhibited the highest mean MIR values.

2.2.5. Random Forest Model Development

The three stem volumes (Vt, Vc and Vp) of interest were predicted at the plot and stand-levels using also the RF package (Liaw 2015) in R (R Core Team 2015). The number of RF trees to grow was set to 1000, and the number of predictor variables performing the data partitioning at each node was set to equal the number of best lidar metrics selected by MIR on Section 2.4 (Liaw 2015). The accuracy of estimates for each model was evaluated in terms of Adj.R^2, Root Mean Square Error (RMSE), and Bias (both absolute and relative) by the linear relationship between predicted (output from RF) and observed stem volumes:

$$\text{RMSE } (\text{m}^3 \cdot \text{ha}^{-1}) = \sqrt{\sum_{i=1}^{n} (y_i - \hat{y}_i)^2 \; /n} \tag{2.5}$$

$$\text{Bias } (\text{m}^3 \cdot \text{ha}^{-1}) = \frac{1}{n} \sum_{i=1}^{n} (y_i - \hat{y}_i) \tag{2.6}$$

where n is the number of plots, y_i is the observed value for plot i, and $\hat{y}_i$ is the predicted value for plot i. Moreover, relative RMSE (%) and biases (%) were calculated by dividing the absolute values (Equations 2.5 and 2.6) by the mean of the observed stem volume. Based on earlier experiences and recommendations from literature, we defined acceptable model accuracy as a relative RMSE and Bias of <15%.

For validation purposes, RF models were embedded in a bootstrap with 500 iterations. In each bootstrap iteration, we drew 50 times with replacement from the 50 available samples. In this procedure, on average 44% of the total of sample (~22 samples) are not drawn. These samples were subsequently used as holdout samples for an independent validation (e.g., Lopatin et al., 2016). In each bootstrap iteration, Adj.R^2, absolute and relative RMSE and Bias were computed based on the linear relationship between observed and predicted volumes using the holdout samples. We used also two-sided Kolmogorov-Smirnov (KS) in R (R Core Team) and a statistical equivalence test (Robinson et al., 2005) to compare the field- and lidar-based stem volume estimates in each iteration.

2.2.6. Predictive Stem Volume Maps

Predictive maps of stem volumes at 25 m of spatial resolution were generated based on the RF models containing the best lidar metrics according to MIR analysis. Because we have a large number of stands in this study, stem volumes predictions at the stand level were then presented herein by stand ages of 3–5, 5–7 and 7–9 years. Additionally, maps of coefficient of variation (CV, given in %) values for the stem volume predictions (as obtained from the 500 bootstrap runs) was also produced for each stand (e.g., Lopatin et al., 2016). Figure 2.3 provides an overview of the study methodology.

2.3 Results

2.3.1. Predictor Variable Selection

A total of 25 of the 32 lidar metrics showed a very strong correlation ($r > 0.9$). We retained one of the highly correlated metrics (H99TH), which along with seven other remaining metrics not extremely highly correlated ($r \geq 0.9$) were included in the MIR analysis (Table 2.5). Lidar metrics that were retained after correlation analysis included HMIN, HCV, HIQ, HSKEW, HKUR, H99TH and COV. Among these, H99TH and HSKEW exhibited the highest mean MIR values (Table 2.6) and therefore, were used for model development. Although HCV also showed high mean MIR values, its inclusion in the models did not significantly improve model performance.

2.3.2. Model Performances

The H99TH and HSKEW that exhibited high MIR values explained more than 80% variations of the stem volumes in Vt, Vc and Vp components with relative RMSE and Bias less than 10% and −0.10%, respectively (Table 2.7). The negative values in Bias indicate that the models are slightly underestimating the stem volumes. Predicted stem volumes at plot level did not differ significantly to the observed stem volumes by the KS and equivalence tests (p-values > 0.05). Figure 2.4 shows the distribution of observed and stem volumes and a good agreement can be observed.

The performance of RF model to predict Vt, Vc and Vp was also summarized in terms of Adj.R^2, RMSE and Bias for all 500 bootstrap runs (Table 2.8). Observed and predicted

stem volumes in each bootstrap iteration did not differ significantly by the statistical KS and equivalence test (*p*-values > 0.05) as well. Overall, all models using H99TH and HSKEW performed very well, with relative RMSE and Bias <15% in the bootstrap procedure. The observed and the average of the predicted stem volumes from the 500 bootstrap runs were also compared and according to the KS and equivalence tests those values did not differ significantly (*p*-values > 0.05) too (Figure 2.5).

2.3.3. Prediction Maps

Box plots of predicted stem values of Vt, Vc and Vp of *P. taeda* at the stand level are shown in Figure 2.5. On average, naturally predicted stem volumes tended to be lower at young age (Figure 2.6a) and higher at advanced age stands (Figure 2.6c). Herein, because it is not convenient to show all the maps for the 50 stands, Figures 2.7 and 2.8 is showing as an example the predicted map of stem volumes and CV (%) with spatial resolution of 25 m for only three stands, but with ages ranging from three to nine years old.

2.4. Discussion

Detailed information on stem total and assortments volumes is required in industrial forest plantations to achieve production efficiency. For instance, incomplete or inaccurate forest information adds to the expense and challenge of forest operations (e.g., Holopainen et al., 2010). Moreover, improving forest plantation productivity and efficiency are important for reducing harvest pressure on natural forests. To achieve efficiency gains in operational forest management, a wide range of forest inventory attributes are required to be measured accurately at high spatial resolution and landscape to regional extents (Sibona et al., 2016). More detailed inventory information can allow forest owners to make better decisions concerning the timing of timber sales, and allow forest companies to optimize their wood supply chain from forest to factory (Kankare et al., 2014). In this study, we present a framework for predicting and mapping total, commercial and pulpwood volumes in industrial *P. taeda* forest plantations using airborne lidar data and RF. While there have been previous studies exploring the use of lidar and non-parametric machine learning

algorithm for forest inventory modeling (e.g., Ahmed et al., 2015; Zhao et al., 2011; Mascaro et al., 2014; Garcia et al., 2015; Hudak et al., 2016), no studies yet have demonstrated the potential of lidar and RF combined for predicting and mapping commercial and pulpwood volumes in industrial pine forest plantations.

Stem total and assortment volumes are directly related to the supply of fiber to pulp and paper companies. Herein, the accuracy of lidar for retrieving Vt, Vc and Vp using RF models was clearly demonstrated through achieving a relative RMSE and Bias less than <15% both for modeling and for validation. As we are predicting forest attributes at a homogenous and single layered forest structure, our measures of precision and accuracy were similar to or higher than those who used lidar data for predicting stem volume through a RF framework in other forest types (Korhonen et al., 2008; Peuhkurinen et al., 2008; Holopainen et al., 2010; Hayashi et al., 2014). Among prior studies, RF has generally showed better performance compared to other statistical approaches, such as multiple linear regression, boosting trees regression and support vector regression (Kankare et al., 2013; Wu et al., 2015; Shataeea et al., 2011). Lidar-derived stem total and saw log volumes and their estimation accuracies have previously been reported at the forest stand level (e.g., Korhonen et al., 2008; Peuhkurinen et al., 2008; Holmgren et al., 2012; Hawbaker et al., 2010). For instance, in Eastern Finland in a typical Finnish southern boreal managed forest area, two studies used lidar data for estimating species-specific diameter distributions and saw log volumes (Korhonen et al., 2008; Peuhkurinen et al., 2008). Two years later, in Southern Wisconsin, USA, lidar data were used for predicting not only saw log volume, but also pulpwood volume (Hawbaker at al., 55); the models produced R^2 of ~0.65 for estimating both saw log and pulpwood volumes. While those authors have showed the great potential of lidar in retrieving assortment volumes, this specific application is still relatively novel and further studies, such as presented herein, still need to be carried out.

In this study, we showed that lidar measurements could be used as input data to predict and map stem total and assortment volumes through a RF framework. High levels of accuracy were found when predicting Vt, Vc and Vp volumes across variable stand ages of *P. taeda* using only H99TH and HSKEW as predictor variables. Lidar-derived H99TH represents the top of the canopy (height at 99th percentile) and HSKEW is a measure of the

asymmetry of height distribution, which is associated with the age of the stands because older trees are taller and cause a more negatively skewed distribution. Skewness and height percentile variables are logical selections for distinguishing between different volume levels based on distributional shapes and height frequencies (Van Aardt et al., 2006). In particular, these variables can explain changes in the volume distribution (Silva et al., 2016), thus providing a solid justification for inclusion in the predictive model. Our results suggest that models based on variables describing the height of the canopy and the symmetry of the distribution of the returns are capable of predicting stem total and assortment volumes across different tree ages in industrial *P. taeda* forest plantations. Height percentile lidar metrics, such as H99TH, and height distributional metrics, such as HSKEW, have been shown to be powerful metrics for modeling and predicting forest attributes (e.g., Næsset et al., 2007; Silva et al., 2017b; Hudak et al., 2017).

A disadvantage of using the RF framework presented here is that RF models do not extrapolate predictions beyond the trained data, and consequently, as found herein, reduce the variance compared to the observations (Figure 2.5). However, an important advantage of non-parametric approaches, such as RF, is that they can model non-linear, complex relationships between the dependent and the independent variables more efficiently than parametric approaches (Mascaro et al., 2014). Furthermore, RF is insensitive to data skew, robust to a high number of variable inputs, and its implementation does not require pre-stratification by forest type (Breiman 2001; Mascaro et al., 2014; Silva et al., 2017b). From an overall statistical perspective, the predicted and observed volumes were equivalent, although our RF model validations showed a systematic tendency to overestimate small values and underestimate high values. The same was found in previous studies (e.g., Lopatin et al., 2016). According to one study (Ota et al., 2014), a possible cause might be that because the RF model estimates values by averaging the predictions of many decision trees, it might tend to underestimate when the predicted value is close to the maximum value of the training data. Similarly, when the estimated value is close to the minimum value of training data it might tend to overestimate. Other possible causes might be that we have a relatively small number of field plots, especially in the young and older stands.

Traditional forest inventory approaches are not effective in terms of costing and mobility especially in *P. taeda* forest plantations, where there is a need to monitor annual forest growth and properties are very large. Lidar remote sensing constitutes an important step towards operational wood procurement planning and is of high current interest to forestry organizations. Such technology is of great interest owing to their spatial sampling capabilities within plantations, and have had great reliability in forest inventory work in countries such as Norway, Canada, or the USA (e.g., Næsset 1997; Næsset 2002; Hudak et al., 2006; Coops et al., 2007). Moreover, the application of airborne lidar technology for Brazilian industrial management is relatively new. While some studies have showed that the cost of the forest inventory derived from lidar could be lower than conventional forest inventory (Tilley et al., 2004; Hummel et al., 2011), the cost of lidar data acquisition could still be high to monitor forest growth annually; however, lidar has the ability to provide wall-to-wall, accurate mapping of forest attributes at high spatial resolutions (e.g., Figures 2.7 and 2.8).

Traditional forest inventory approaches are based on sampling theory, and forest attributes measured at plot level are then used to infer inventory attributes for an entire stand (Silva et al., 2014). We showed here that lidar and RF machine learning combined can be a powerful tool for mapping forest attributes in *P. taeda* forest plantations. In practice, lidar-derived maps of stem total and assortment volumes (Figures 2.7 and 2.8) allow the owners to evaluate the production and forest structure variability within stands in a spatially explicit manner, which is not possible in a traditional forest inventory of *P. taeda*. Also, such maps may allow managers to detect spatial patterns related to tree diseases, fire or forest clearing.

Recently, a study carried out in *Eucalyptus* spp. forest plantations showed that lidar and RF could be combined to predict and map aboveground carbon at high spatial resolution (5 m), even if the models are calibrated using field plots with area larger than the cell size used for mapping (Silva et al., 2017b). Therefore, future studies should be also test the ability of lidar and RF to map stem total and assortment volumes even at higher spatial resolution than presented in this study (e.g., Figures 7.2 and 8.2). Herein, we demonstrated the potential of combined lidar-derive metrics and RF to predict forest attributes through a lidar-plot based approach framework, however, to get even higher amount of details in *P. taeda* forest

plantations, RF could be also tested in a lidar-individual tree based approach. For instance, RF has been successfully used to impute individual tree height and volume in longleaf pine (*Pinus palustris* Mill.) forest in Southern USA (Silva et al., 2016); therefore, lidar and RF could be also used to predict stem total and assortment volumes at an individual tree level in *P. taeda* forest plantations, if carefully implemented.

2.5. Conclusions

Refining strategies for improving productivity of forest plantations requires accurate and detailed spatial information on forest structure and growing stock volume. In this study, we showed that airborne lidar data metrics can predict total, commercial and pulpwood volumes in a *P. taeda* forest plantation in Brazil. We found that different stem volumes can be estimated with high levels of accuracy from two lidar-derived variables describing the height and the shape of the vertical distribution of the height. The use of a model based on two variables suggests a higher generalization potential than models based on specific metrics that could result in over-fitting. However, this potential should be tested in other plantations and forested environments. Although airborne lidar data has not been adopted by paper companies operationally, our results show that the method used could be readily applied to support the supply chain of pulp and paper companies in Brazil or elsewhere.

References

Ahmed, O.S.; Franklin, S.E.; Wulder, M.A.; White, J.C. (2005) Characterizing stand-level forest canopy cover and height using landsat time series , samples of airborne lidar, and the random forest algorithm. *ISPRS J. Photogramm. Remote Sens.*, *101*, 89–101, doi:10.1016/j.isprsjprs.2014.11.007.

Andersen, H.E.; McGaughey, R.J.; Reutebuch, S.E. Estimating forest canopy fuel parameters using lidar data. (2005). *Remote Sens. Environ.*, *94*, 441–449, doi:l0.1016/j.rse.2004.10.0.

Breiman, L. (2001). Random forests. *Mach. Learn.*, *45*, 5–32, doi:10.1023/A:1010933404324.

Bright, B.C.; Hudak, A.T.; McGaughey, R.; Andersen, H.E.; Negron, J. (2013). Predicting live and dead tree basal area of bark beetle affected forests from discrete-return lidar. *Can. J. Remote Sens*., *39*, S99–S111, doi:10.5589/m13-027.

Coops, N.C.; Hilker, T.; Wulder, M.A.; St-Onge, B.; Newnham, G.; Siggins, A. (2007). Estimating canopy structure of Douglas-fir forest stands from discrete-return lidar. *Trees*, *21*, 295−310, doi:10.1007/s00468-006-0119-6.

Curtis, R.O. (1967) Height-diameter and height-diameter-age equations for second-growth Douglas-fir. *For. Sci*., *13*, 365–375.

Evans, J.S.; Cushman, S.A. (2009). Gradient modeling of conifer species using Random Forests. *Landsc. Ecol*., *5*, 673–683, doi:10.1007/s10980-009-9341-0.

Evans, J.S.; Murphy, M.A.; Holden, Z.A.; Cushman, S.A. (2010). Modeling species distribution and change using Random Forests. In *Predictive Modeling in Landscape Ecology*; Drew, C.A., Huettmann, F., Wiersma, Y., Eds.; Springer: New York, NY, USA, 139–159.

García Gutiérrez, J.; Martínez Álvarez, F.; Troncoso Lora, A.; Riquelme Santos, J.C. (2015). A comparison of machine learning regression techniques for lidar-derived estimation of forest variables. *Neurocomputing*, *167*, 24–31,doi:10.1016/j.neucom.2014.09.091.

Grossmann, E.; Ohmann, J.; Kagan, J.; May, H.; Gregory, M. (2010). Mapping ecological systems with a random forest model: Tradeoffs between errors and bias. *GAP Anal. Bull.*, *17*, 16–22.

Hudak, A.T.; Evans, J.S.; Stuart, A.M. (2009). Lidar utility for natural resource managers. *Remote Sens.*, *1*, 934–951, doi:10.3390/rs1040934.

Hudak, A.T.; Crookston, N.L.; Evans, J.S.; Falkowski, M.J.; Smith, A.M.; Gessler, P.E.; Morgan, P. (2006). Regression modeling and mapping of coniferous forest basal area and tree density from discrete-return lidar and multispectral satellite data. *Can. J. Remote Sens*., *32*, 126–138, doi:10.5589/m06-007.

Hudak, A.T.; Crookston, N.L.; Evans, J.S.; Hall, D.E.; Falkowski, M.J. (2008). Nearest neighbor imputation of species-level, plot-scale forest structure attributes from lidar data. *Remote Sens. Environ*., *112*, 2232–2245, doi:10.1016/j.rse.200.10.009.

Hudak, A.T.; Strand, E.K.; Vierling, L.A.; Byrne, J.C.; Eitel, J.U.H.; Martinuzzi, S.; Falkowski, M.J. (2012). Quantifying aboveground forest carbon pools and fluxes from repeat lidar surveys. *Remote Sens. Environ*., *123*, 25–40, doi:10.1016/j.rse.2012.02.023.

Hudak, A.T.; Bright, B.C.; Pokswinski, S.M.; Loudermilk, E.L.; O'Brien, J.J.; Hornsby, B.S.; Klauberg, C.; Silva, C.A. (2016). Mapping forest structure and composition from low-density lidar for informed forest, fuel, and fire management at Eglin Air Force Base, Florida, USA. *Can. J. Remote Sens.*, *42*, 411–427, doi:10.1080/07038992.2016.1217482.

Hayashi, R.; Weiskittel, A.; Sader, S. (2014). Assessing the feasibility of low-density lidar for stand inventory attribute predictions in complex and managed forests of Northern Maine, USA. *Forests*, *5*, 363–383, doi:10.3390/f5020363.

Holmgren, J.; Barth, A.; Larsson, H.; Olsson, H. (2012). Prediction of stem attributes by combining airborne laser scanning and measurements from harvesters. *Silva Fen.*, *46*, 227–239, doi:doi.org/10.14214/sf.56.

Hawbaker, T.J.; Gobakken, T.; Lesak, A.; Trømborg, E.; Contrucci, K.; Radeloff, V. (2010). Light detection and ranging-based measures of mixed hardwood forest structure. *For. Sci.*, *56*, 313–326.

Hummel, S.; Hudak, A.T.; Uebler, E.H.; Falkowski, M.J.; Megown, K.A. (2011). A comparison of accuracy and cost of lidar versus stand exam data for landscape management on the Malheur national forest. *J. For.*, *109*, 267–273.

Holopainen, M.; Vastaranta, M.; Rasinmäki, J.; Kalliovirta, J.; Mäkinen, A.; Haapanen, R.; Melkas, T.; Yu, X.; Hyyppä, J. (2010). Uncertainty in timber assortment estimates predicted from forest inventory data. *Eur. J. For. Res.*, *129*, 1131–1142, doi:10.3390/f1030177.

Indústria Brasileira de Árvores (IBÁ). (2015). Brazilian Tree Industry. Available online: http://www.iba.org/images/shared/iba_2015.pdf (accessed on 10 November 2016).

Kankare, V.; Vastaranta, M.; Holopainen, M.; Raty, M.; Yu, X.; Hyyppa, J.; Hyyppa, H.; Alho, P.; Viitala, R. (2013). Retrieval of forest aboveground biomass and stem volume with airborne scanning lidar. *Remote Sens.*, *5*, 2257–2274, doi:10.3390/rs5052257.

Kankare, V.; Vauhkonen, J.; Tanhuanpaa, T.; Holopainen, M.; Vastaranta, M.; Joensuu, M. (2014). Accuracy in estimation of timber assortments and stem distribution—A comparison of airborne and terrestrial laser scanning techniques. *ISPRS J. Photogramm. Remote Sens.*, *97*, 89–97, doi:10.1016/j.isprsjprs.2014.08.008.

Kohler, S.V.; Wolff, N.I.; Figueiredo Filho, A; Arce, J.E. (2014). Dynamic of assortment of *Pinus taeda* L. plantation in different site classes in Southern Brazil. *Sci. For.*, *42*, 403–410.

Korhonen, L.; Peuhkurinen, J.; Jukka, M.; Suvanto, A.; Maltamo, M.; Packalen, P.; Kangas, J. (2008). The use of airborne laser scanning to estimate sawlog volumes. *Forestry, 81,* 499–510, doi:10.1093/forestry/cpn018.

Ko, C.; Sohn, G.; Remmel, T.K.; Miller, J.R. (2016). Maximizing the Diversity of Ensemble Random Forests for Tree Genera Classification Using High Density Lidar Data. *Remote Sens., 8,* 646, doi:10.3390/rs8080646.

Köppen, W.; Geiger, R. (1928). *Klimakarte der Erde. Wall-map 150 cm × 200 cm*; Verlag Justus Perthes: Gotha, Germany.

Kraus, K.; Pfeifer, N. (1998). Determination of terrain models in wooded areas with airborne laser scanner data. *ISPRS J. Photogramm. Remote Sens., 53,* 193–203, doi:10.1016/S0924-2716(98)00009-4.

Liaw, A.; Wiener, M. (2015) *RandomForest:* Breiman and Cutler's Random Forests for Classification and Regression, Version 4.6–12. Available online: https://cran.rproject.org/web/packages/randomForest/ (accessed on 15 October 2016).

Lawrence, R.L.; Wood, S.D.; Sheley, R.L. (2006). Mapping invasive plants using hyperspectral imagery and Breiman Cutler classifications (RandomForest). *Remote Sens. Environ., 100,* 356–362, doi:10.1016/j.rse.2005.10.014.

Lopatin, J.; Dolos, K.; Hernández, H.J.; Galleguillos, M.; Fassnacht, F.E. (2016). Comparing Generalized Linear Models and random forest to model vascular plant species richness using lidar data in a natural forest in central Chile. *Remote Sens. Environ., 173,* 200–210, doi:10.1016/j.rse.2015.11.029.

Mascaro, J.; Asner, G.P.; Knapp, D.E.; Kennedy-Bowdoin, T.; Martin, R.E.; Anderson, C.; Higgins, M.; Chadwick, K.D. (2014). A tale of two "forests": Random forest machine learning AIDS tropical forest carbon mapping. *PLoS ONE, 9,* e85993, doi:10.1371/journal.pone.0085993.

McGauchey, R.J. (2015). *FUSION/LDV: Software for lidar Data Analysis and Visualization*; Forest Service Pacific Northwest Research Station USDA: Seattle, WA, USA. Available online: http://forsys.cfr.washington.edu/fusion/ FUSIONmanual.pdf (accessed on 15 October 2015).

Næsset, E. (1997). Determination of mean tree height of forest stands using airborne laser scanner data. *ISPRS J. Photogramm., 52,* 49–56, doi:10.1016/S0924-2716(97)83000-6.

Næsset, E. (2002). Predicting forest stand characteristics with airborne scanning laser using a practical two-stage procedure and field data. *Remote Sens. Environ.*, *80*, 88–99, doi:10.1016/S0034-4257(01)00290-5.

Næsset, E.; Gobakken, T.; Holmgren, J.; Hyyppä, H.; Hyyppä, J.; Maltamo, M.; Nilsson, M.; Olsson, H.; Persson, Å.; Söderman, U. (2004). Laser scanning of forest resources: The Nordic experience. *Scand. J. For. Res.*, *19*,482–499.

Næsset, E. (2007). Airborne laser scanning as a method in operational forest inventory: Status of accuracy assessments accomplished in Scandinavia. *Scand. J. For. Res.*, *22*, 433–442, doi:10.1080/02827580701672147.

Naidoo, L.; Cho, M.A.; Mathieu, R.; Asner, G. (2012). Classification of savanna tree species, in the Greater Kruger National Park region, by integrating hyperspectral and Lidar data in a Random Forest data mining environment. *ISPRS J. Photogramm. Remote Sens.*, *69*, 167–179, doi:10.1016/j.isprsjprs.2012.03.005.

Olden, J.D.; Lawler, J.J.; Poff, N.L. (2008). Machine learning methods without tears: A primer for ecologists. *Q. Rev. Biol.*, *83*, 171–193.

Ota, T.; Ahmed, O.S.; Franklin, S.E.; Wulder, M.A.; Kajisa, T.; Mizoue, N. (2014). Estimation of Airborne Lidar Derived Tropical Forest Canopy Height Using Landsat Time Series in Cambodia. *Remote Sens*., *6*, 10750–10772, doi:10.3390/rs61110750.

Payn, T.; Carnus, J.-M.; Freer-Smith, P.; Kimberley, M.; Kollert, W.; Liu, S.; Orazio, C.; Rodriguez, L.; Silva, L.N.; Wingfield, M.J. (2015). Changes in planted forests and future global implications. *For. Ecol. Manag*., *352*, 57–67, doi:10.1016/j.foreco.2015.06.021.

Peuhkurinen, J.; Maltamo, M.; Malinen, J. (2008). Estimating Species-Specific diameter distributions and saw log recoveries of boreal forests from airborne laser scanning data and aerial photographs: A distribution-based approach. *Silva Fenn.*, *42*, 600–625, doi:10.14214/sf.237.

Yu, X.; Hyyppä, J.; Vastaranta, M.; Holopainen, M.; Viitala, R. (2011). Predicting individual tree attributes from airborne laser point clouds based on the random forests technique. *ISPRS J. Photogramm. Remote Sens.*, *661*, 28–37, doi:10.1016/j.isprsjprs.2010.08.003.

R Core Team. (2017). *R: A Language and Environment for Statistical Computing*; R Foundation for Statistical Computing: Vienna, Austria. Available online: http://www.R-project.org (accessed on 20 October 2016).

Robinson, A.P.; Duursma, R.A.; Marshall, J.D. (2005). A regression-based equivalence test for model validation: Shifting the burden of proof. *Tree Physiol*., *25*,903–913.

Peuhkurinen, J.; Maltamo, M.; Malinen, J.; Pitkänen, J.; Packalén, P. (2007).Pre-harvest measurement of marked stands using airborne laser scanning. *For. Sci*., *53*, 653–661.

Shataeea, S.; Weinaker, H.; Babanejad, M. (2011). Plot-level Forest Volume Estimation Using Airborne Laser Scanner and TM Data, Comparison of Boosting and Random Forest Tree Regression Algorithms. *Procedia Environ. Sci*., *7*, 68–73, doi:10.1016/j.proenv.2011.07.013.

Silva, C.A.; Klauberg, C.; Carvalho, S.D.P.C.; Hudak, A.T. (2014). Mapping aboveground carbon stocks using Liar data in *Eucalyptus* spp. plantations in the state of São Paulo, Brazil. *Sci. For*., *42*, 591–604.

Silva, C.A.; Klauberg, C.; Hudak, A.T.; Vierling, L.A.; Liesenberg, V.; Carvalho, S.P.; Rodriguez, L.C. (2016). A principal component approach for predicting the stem volume in *Eucalyptus* plantations in Brazil using airborne Lidar data. *Forestry*, *89*, 422–433, doi:10.1093/forestry/cpw016.

Silva, C.A.; Hudak, A.T.; Vierling, L.A.; Loudermilk, E.L.; O'Brien, J.J.; Hiers, J.K.; Jack, S.B.; Gonzalez-Benecke, C.A.; Lee, H.; Falkowski, M.J. (2016). Imputation of individual longleaf pine forest attributes from field and lidar data. *Can. J. Remote Sens.*, *42*, 554–573, doi:10.1080/07038992.2016.1196582.

Silva, C.A.; Klauberg, C.; Hudak, A.T.; Vierling, L.A.; Liesenberg, V.; Bernett, L.G.; Scheraiber, C.F.; Schoeninger, E.R. (2017a). Estimating Stand Height and Tree Density in *Pinus taeda* plantations using in-situ data, airborne lidar and k-Nearest Neighbor Ismputation. *Ann. Braz. Acad. Sci*., *90*, 1–15, in press.

Silva, C.A.; Hudak, A.T.; Klauberg, C.; Vierling, L.A.; Gonzalez-Benecke, C.; de Padua Chaves Carvalho, S.; Rodriguez, L.C.E.; Cardil, A. (2017b). Combined effect of pulse density and grid cell size on predicting and mapping aboveground carbon in fast-growing Eucalyptus forest plantation using airborne lidar data. *Carbon Balance Manag*., *12*, 13.

Sherrill, J.R.; Bullock, B.P.; Mullin, T.J.; McKeand, S.E.; Purnell, R.C. (2011). Total and merchantable stem volume equations for mid rotation loblolly pine (*Pinus taeda* L.). *South. J. Appl. For*., *35*, 105–108.

Sibona, E.; Vitali, A.; Meloni, F.; Caffo, L.; Dotta, A.; Lingua, E.; Motta, R.; Garbarino, M. (2016). Direct Measurement of Tree Height Provides Different Results on the Assessment of lidar Accuracy. *Forests*, *8*, 1–12, doi:10.3390/f8010007.

Stumpf, A.; Kerle, N. (2011). Object-oriented mapping of landslides using Random Forests. *Remote Sens. Environ*., *115*, 2564–2577, doi:10.1016/j.rse.2011.05.013.

Schöpfer, W. (1966). Automatisierung Des Massem, Sorten Und Wertberechnung Stenender Waldbestande Schriftenreihe Bad; Wurtt-Forstl: Koblenz, Germany.

Tilley, B.K.; Munn, I.A.; Evans, D.L.; Parker, R.C.; Roberts, S.D. (2004). Cost Considerations of Using Lidar for Timber Inventory. Available online: http://sofew.cfr.msstate.edu/papers/0504tilley.pdf/ (accessed on 21 March 2016).

Van Aardt, J.A.N.; Wynne, R.H.; Oderwald, R.G. (2006). Forest Volume and Biomass Estimation Using Small-Footprint Lidar Distributional Parameters on a Per-Segment Basis. *For. Sci*., *52*, 636–649.

White, J.C.; Wulder, M.A.; Buckmaster, G. (2014). Validating estimates of merchantable volume from airborne laser scanning (ALS) data using weight scaled data. *For. Chron.*, *90*, 378–385, doi:10.5558/tfc2014-072.

Wu, J.; Yao, W.; Choi, S.; Park, T.; Myneni, R.B. (2015). A Comparative Study of Predicting DBH and Stem Volume of Individual Trees in a Temperate Forest Using Airborne Waveform lidar. *IEEE Geosci. Remote Sens. Lett*., *12*, 2267–2271, doi:10.1109/LGRS.2015.2466464.

Zhao, K.; Popescu, S.; Meng, X.; Pang, Y.; Agca, M. (2011). Characterizing forest canopy structure with lidar composite metrics and machine learning. *Remote Sens Environ.*, *115*, 1978–1996, doi:10.1016/j.rse.2011.04.001.

Table 2.1. Statistics of the taper models.

DBH (cm) Range	Adj. R^2	SEE (%)	
		dbh	Volume
0.0–17.9	0.96	9.58	11.55
18.0–29.9	0.98	7.99	9.33
30.0–70.0	0.98	7.52	8.21

Table 2.2. Summary of stem volumes computed in the 50 field sample plots.

Ages (I)	Stem Total and Assortment Volumes ($m^3 \cdot ha^{-1}$)			*N*
	Vt	Vc	Vp	
$3 \leq I < 5$	56.25 ± 10.98	47.53 ± 12.15	45.67 ± 11.14	19
$5 \leq I < 7$	134.20 ± 30.77	124.67 ± 30.3	114.20 ± 23.41	22
$7 \leq I < 9$	169.50 ± 22.86	160.2 ± 22.20	129.50 ± 24.83	13
Mean ± Sd	113.70 ± 52.53	103.86 ± 52.99	92.13 ± 42.11	Total = 50

N = number of plots.

Table 2.3. Airborne lidar system characteristics.

Parameter	Value
Scan angle (°)	+/−30°
Footprint (m)	0.33 m
Flight speed (km/h)	234.0 km/h
Horizontal accuracy	10 cm
Elevation accuracy	15 cm
Operating altitude	666.17 m
Scan frequency	300 kHz
Pulse density	4 pulse m^{-2}

Table 2.4. Lidar-derived canopy height metrics considered as candidate variables for predictive V models .

Variable	Description
HMIN	Height Minimum
HMAX	Height Maximum
HMEAN	Height Mean
HMAD	Height median absolute deviation
HSD	Height standard deviation
HSKEW	Height skewness
HKURT	Height kurtosis
HCV	Height coefficient of variation
HIQ	Height interquartile range
HMODE	Height mode
H01TH	Height 1th percentile
H05TH	Height 5th percentile
H10TH	Height 10th percentile
H15TH	Height 15th percentile
H20TH	Height 20th percentile
H25TH	Height 25th percentile
H30TH	Height 30th percentile
H35TH	Height 35th percentile
H40TH	Height 40th percentile
H45TH	Height 45th percentile
H50TH	Height 50th percentile
H55TH	Height 55th percentile
H60TH	Height 60th percentile
H65TH	Height 65th percentile
H70TH	Height 70th percentile
H75TH	Height 75th percentile
H80TH	Height 80th percentile
H90TH	Height 90th percentile
H95TH	Height 95th percentile
H99TH	Height 99th percentile
CR	Canopy Relief Ratio ((HMEAN − HMIN)/(HMAX − HMIN))
COV	Canopy Cover (Percentage of first return above 1.30 m)

Table 2.5. Pearson's correlations among lidar metrics selected.

r	**HMIN**	**HCV**	**HIQ**	**HSKEW**	**HKUR**	**H99TH**	**COV**
HCV	−0.45 **						
HIQ	0.14	−0.09					
HSKEW	−0.30 **	0.83 ***	−0.36 *				
HKUR	0.27	−0.81 ***	0.07	−0.82 ***			
H99TH	0.39 **	−0.80 ***	0.61 ***	−0.81 ***	0.77 ***		
COV	0.23	−0.74 ***	0.12	−0.67 ***	0.53 ***	0.58 ***	

"***": p-value < 0.001; "**": p-value < 0.01; "*": p-value < 0.05; If there is no *: p-value ≥ 0.05.

Table 2.6. Mean of the model improvement ratio (MIR) among the remained lidar-derived metrics not highly correlated. The bold represents the highest MIR values.

Atributes	**Lidar-Derived Metrics**						
	HMIN	**HCV**	**HIQ**	**HSKEW**	**HKUR**	**H99TH**	**COV**
Vt	0.16	0.40	0.18	0.75	0.31	0.99	0.12
Vc	0.15	0.39	0.17	0.77	0.30	0.99	0.10
Vp	0.16	0.65	0.20	0.74	0.38	0.98	0.11

Table 2.7. Model accuracies per stem volume type. The average and standard deviation of Adj. R2, RMSE and bias derived from the 500 bootstrap runs are displayed.

Volume	**Adj. R^2**	**RMSE**		**Bias**	
		$m^3 \cdot ha^{-1}$	**%**	**$m^3 \cdot ha^{-1}$**	**%**
Vt	0.94 ± 0.02	12.02 ± 2.78	9.80 ± 2.18	−0.58 ± 2.85	−0.45 ± 2.30
Vc	0.95 ± 0.02	11.67 ± 2.76	10.31 ± 2.76	−0.95 ± 2.80	−0.82 ± 2.45
Vp	0.91 ± 0.04	11.83 ± 2.56	12.10 ± 2.57	−0.49 ± 2.73	−0.54 ± 2.77

Table 2.8. Model accuracies of random forest (RF) models per stem volume in terms of Adj.R2, Root Mean Square Error (RMSE) and bias calculated by the relationship between predicted and observed stem volumes.

Volume	**Lidar Derived Metrics**	**Adj. R^2**	**RMSE**		**Bias**	
			$m^3 \cdot ha^{-1}$	**%**	**$m^3 \cdot ha^{-1}$**	**%**
Vt	H99TH + HSKEW	0.97	8.91	7.83	−0.19	−0.17
Vc		0.98	8.00	7.71	−0.12	−0.12
Vp		0.96	7.96	8.63	−0.22	−0.24

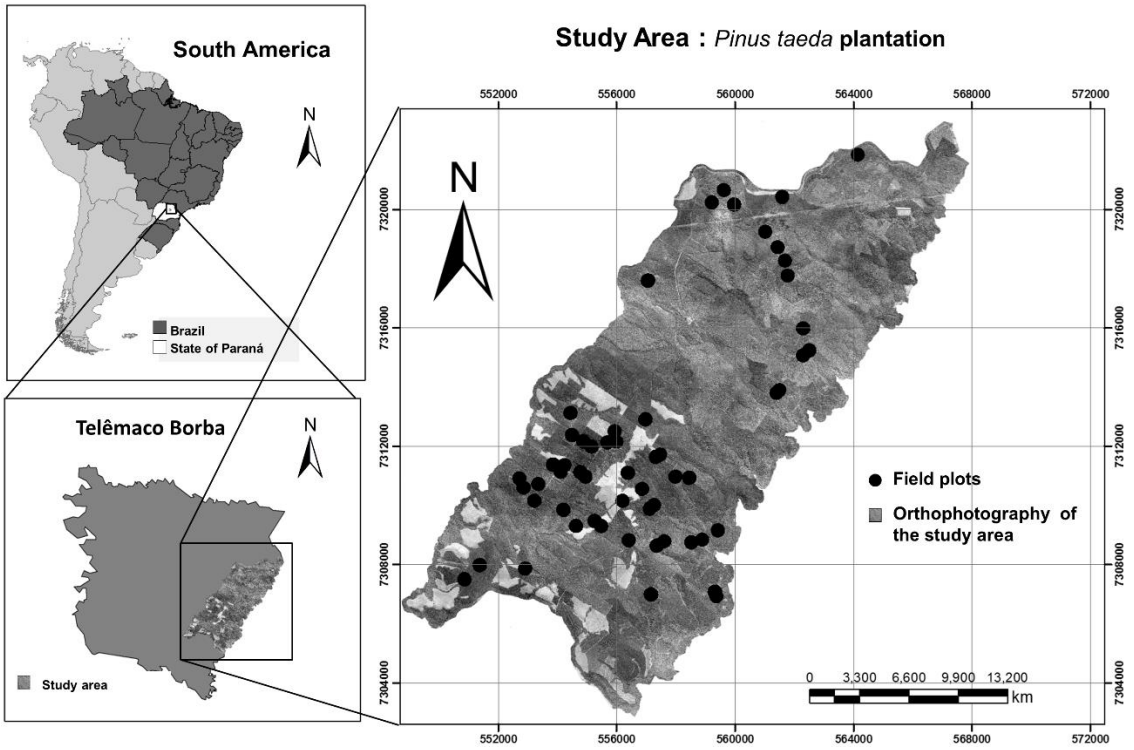

Figure 2.1. Location of study area in Telêmaco Borba, Paraná, Brazil. The black dots indicate the location of the *Pinus taeda* stands.

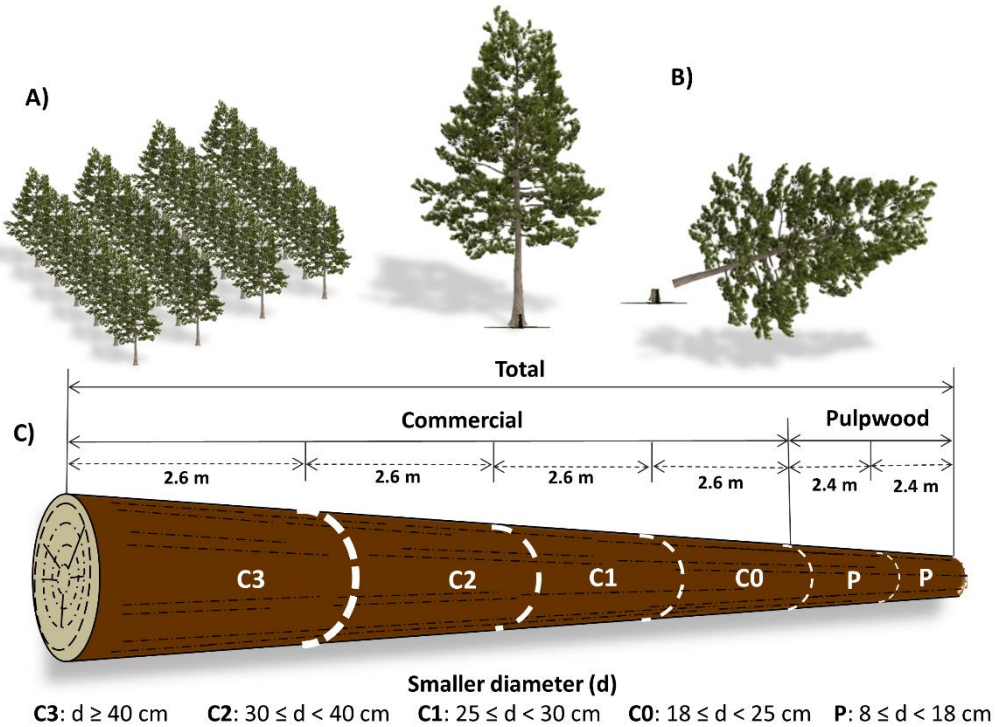

Figure 2.2. Process of forest volume measurement. (A) Pinus plantation; (B) Timber harvester and (C) Log segmentation for classes of volume measurements.

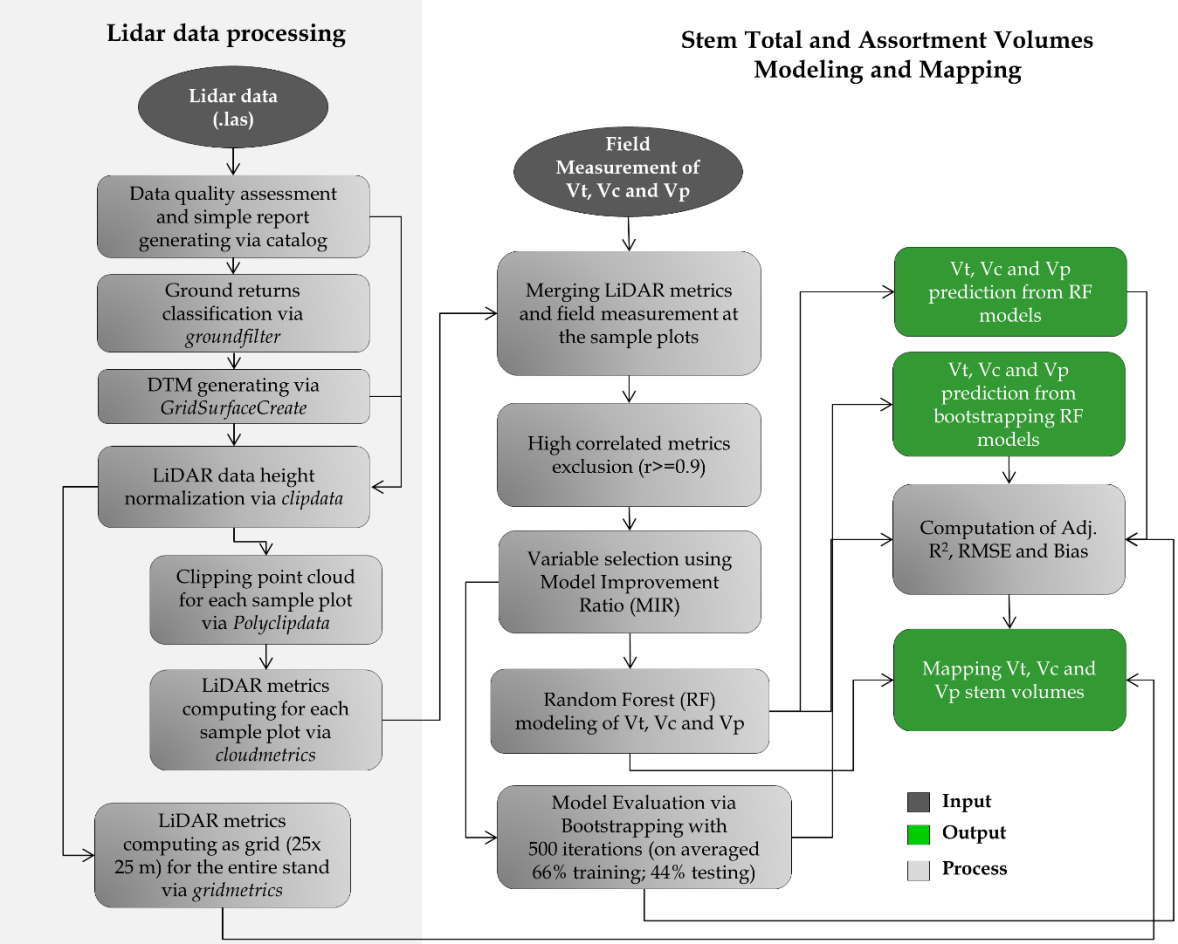

Figure 2.3. Procedure for predicting stem total and assortment volumes in an industrial P. taeda forest plantation using airborne laser scanning data and random forest.

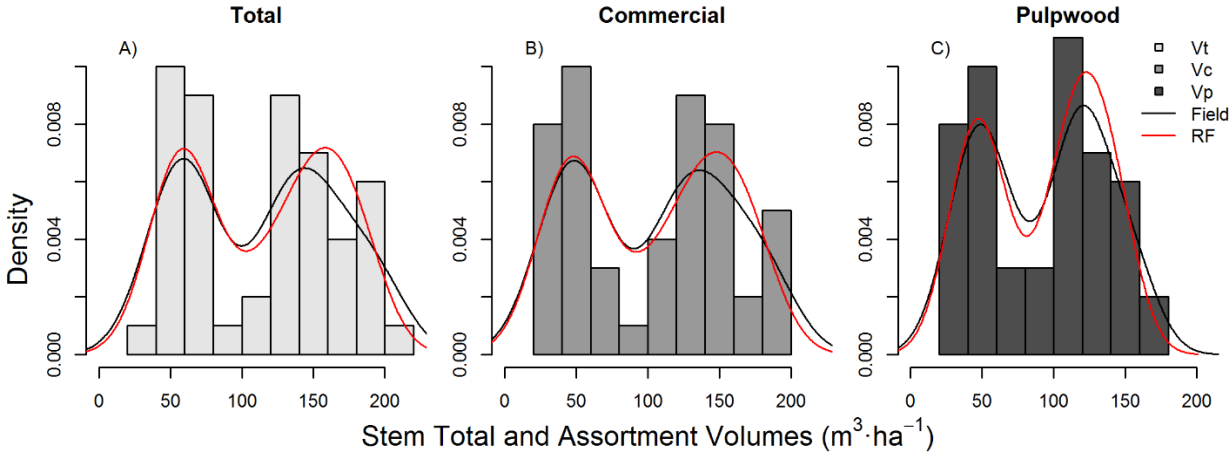

Figure 2.4. Distribution of observed (black line) and predicted (red line) stem volume from RF. The gray histograms are based from field data. (A) Total volume (Vt) (B) Commercial volume (Vc) and (C) Pulpwood volume (Vp).

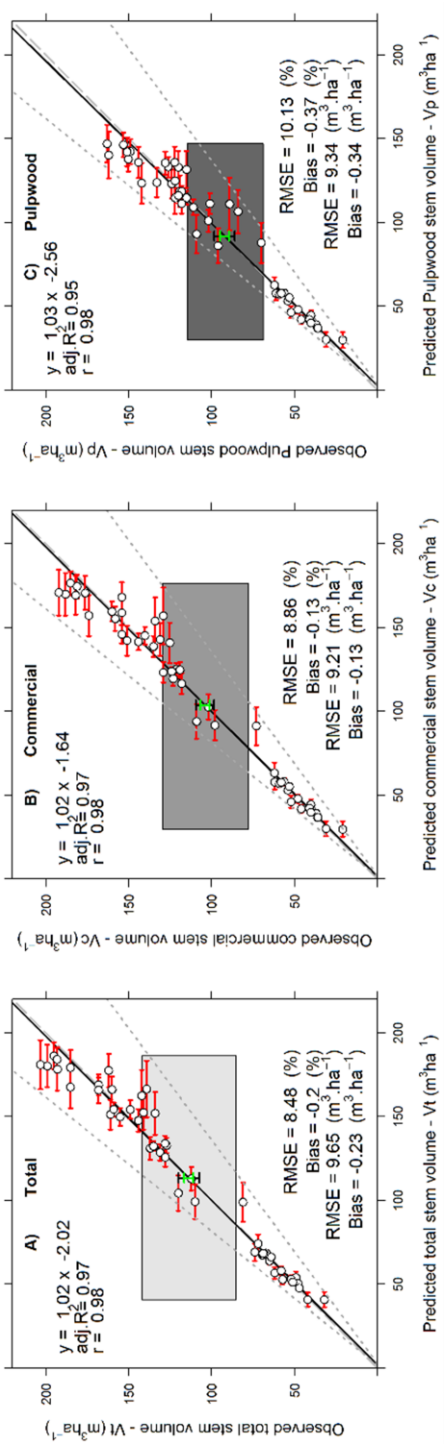

Figure 2.5. Equivalence plots of the observed and the mean of predicted Vt (A), Vc (B) and Vp (C) obtained from the 500 bootstrapped RF model runs. (N = 50). The equivalence plot design presented herein is an adaptation of the original equivalence plots presented by Robinson (2015).. The grey polygon represents the ±25% region of equivalence for the intercept, and the green vertical bar represents a 95% of confidence interval for the intercept. The predicted stem volumes from the RF models are equivalent with reference to the intercept and slope since the green bar is completely within the grey polygon. If the grey polygon is lower than the green vertical bar, the predicted stem volumes are negatively biased; and if it is higher than the green vertical bar, the predicted stem volumes are positively biased. Moreover, the grey dashed line represents the ±25% region of equivalence for the slope, the fit line is within the dotted lines and the black vertical bar is within the gray rectangle, indicating that the pairwise measurements are equivalent. A green bar that is wider than the region outlined by the grey dashed lines indicates highly variable predictions. The white dots are the pairwise measurements, and the solid line is a best-fit linear model for the pairwise measurements. The light grey dashed line represented the relationship 1:1. The horizontal red bars represent the standard deviation of the 500 bootstrapping predictions.

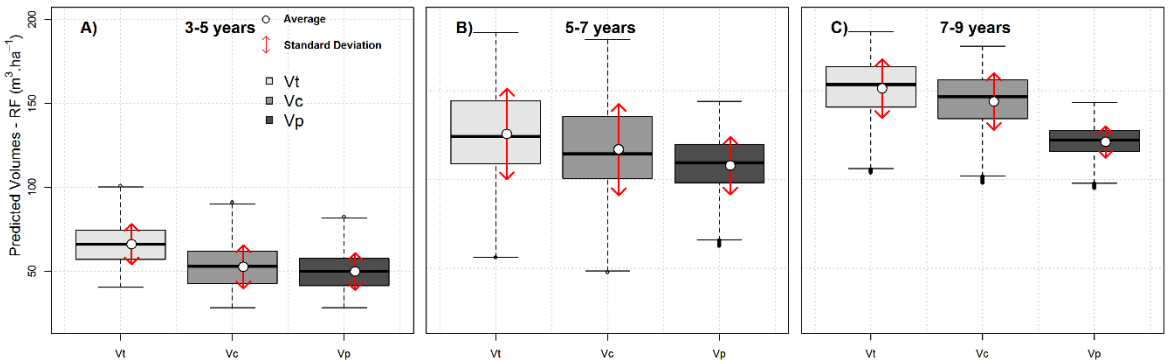

Figure 2.6. Predicted Vt, Vc and Vp of P. taeda at stand-level for the studied stands. (A) 3–5 years; (B) 5–7 years and (C) 7–9 years. The thick line in the box indicates the median value of the predicted stem volume. Boxes extend from the 25th to the 75th percentile, whiskers extend 1.5 times the length of the interquartile range above and below the 75th and 25th percentiles. The white dot is the mean of the predicted stem volume, and the vertical red lines represent the standard deviation around the mean (Mean ± SD).

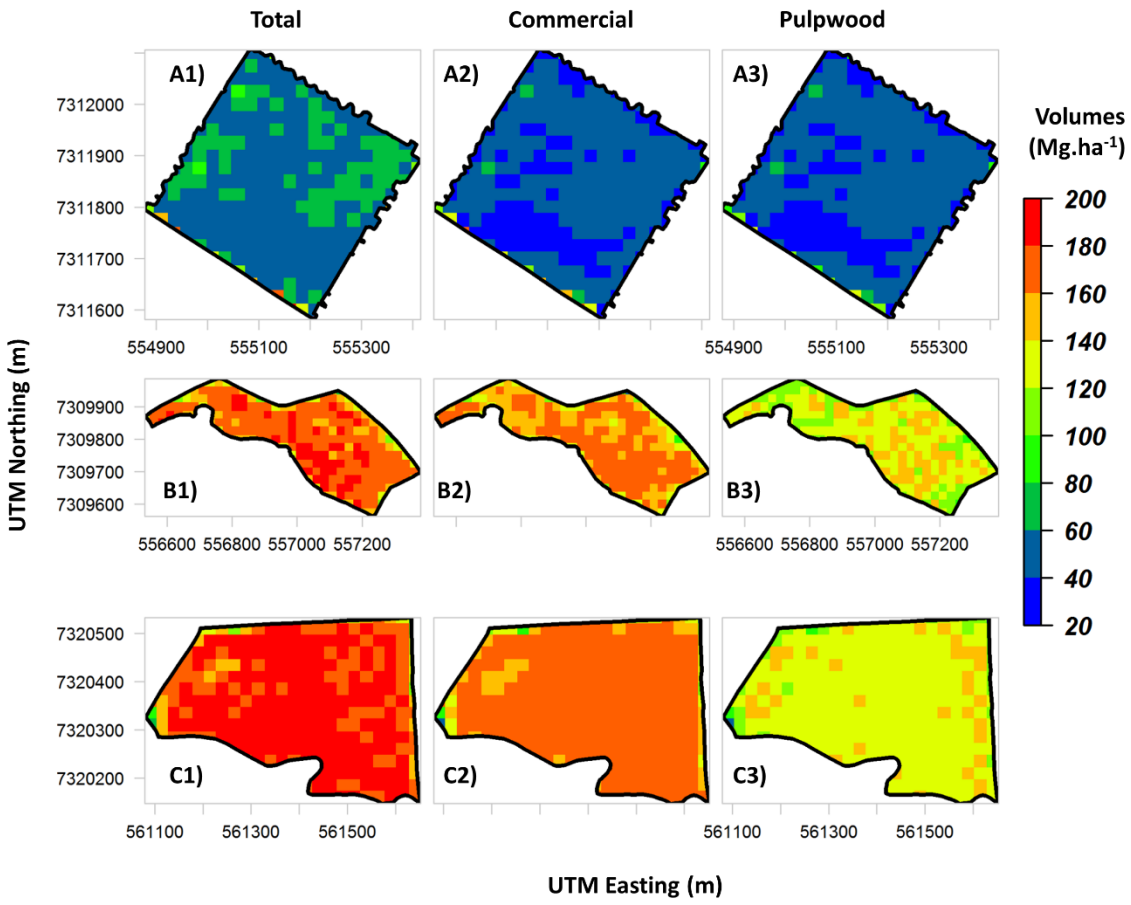

Figure 2.7. Predicted Vt (A1–C1), Vc (A2–C2) and Vp (A3–C3) of *P. taeda* at the stand-level obtained from the RF models. Representative stand of early (i.e., 3–5 years) (A1–3), intermediate (i.e., 5–7 years) (B1–3) and advanced-stages of development (i.e., 7–9 years) (C1–3).

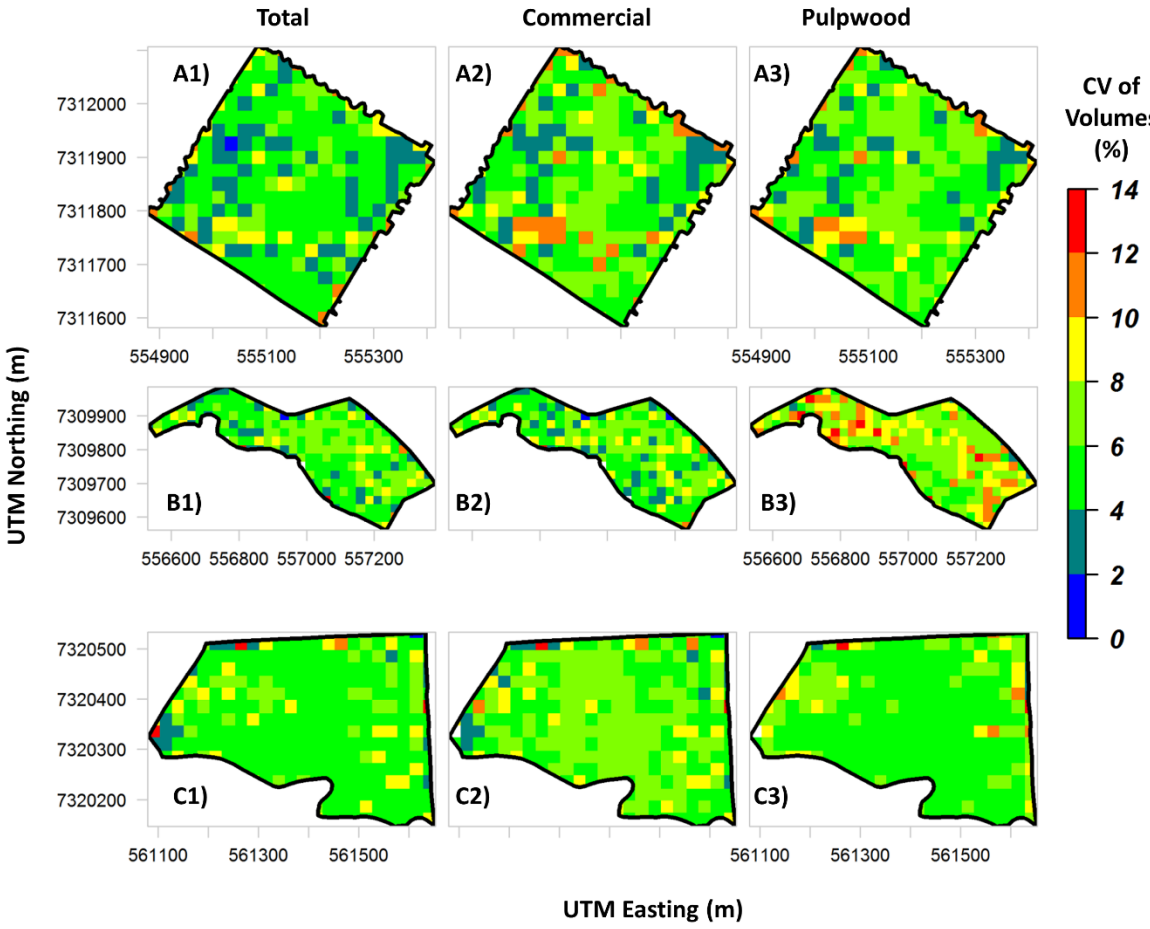

Figure 2.8. Coefficient of variation (CV) maps in percentage (%) of Vt (A1–C1), Vc (A2–C2) and Vp (A3–C3) of *P. taeda* at the stand-level obtained from the 500 RF bootstrapped runs. Representative stand of early (i.e., 3–5 years) (A1–3), intermediate (i.e., 5–7 years) (B1–3) and advanced stages of development (i.e., 7–9 years) (C1–3).

Chapter 3. Impacts of Airborne Lidar Pulse Density on Estimating Biomass Stocks and Changes in a Selectively Logged Tropical Forest

Silva, C.A.; Hudak, A.T.; Vierling, L.A.; Klauberg, C.; Garcia, M.; Ferraz, A.; Keller, M.; Eitel, J.; Saatchi, S. Impacts of Airborne Lidar Pulse Density on Estimating Biomass Stocks and Changes in a Selectively Logged Tropical Forest. Remote Sensing. 2017, 9, 1068.

Abstract

Airborne lidar is a technology well-suited for mapping many forest attributes, including aboveground biomass (AGB) stocks and changes in selective logging in tropical forests. However, trade-offs still exist between lidar pulse density and accuracy of AGB estimates. We assessed the impacts of lidar pulse density on the estimation of AGB stocks and changes using airborne lidar and field plot data in a selectively logged tropical forest located near Paragominas, Pará, Brazil. Field-derived AGB was computed at 85 square 50 × 50 m plots in 2014. Lidar data were acquired in 2012 and 2014, and for each dataset the pulse density was subsampled from its original density of 13.8 and 37.5 pulses·m^{-2} to lower densities of 12, 10, 8, 6, 4, 2, 0.8, 0.6, 0.4 and 0.2 pulses·m^{-2}. For each pulse density dataset, a power-law model was developed to estimate AGB stocks from lidar-derived mean height and corresponding changes between the years 2012 and 2014. We found that AGB change estimates at the plot level were only slightly affected by pulse density. However, at the landscape level we observed differences in estimated AGB change of >20 Mg·ha^{-1} when pulse density decreased from 12 to 0.2 pulses·m^{-2}. The effects of pulse density were more pronounced in areas of steep slope, especially when the digital terrain models (DTMs) used in the lidar derived forest height were created from reduced pulse density data. In particular, when the DTM from high pulse density in 2014 was used to derive the forest height from both years, the effects on forest height and the estimated AGB stock and changes did not exceed 20 Mg·ha^{-1}. The results suggest that AGB change can be monitored in selective logging in tropical forests with reasonable accuracy and low cost with low pulse density lidar surveys if a baseline high-quality DTM is available from at least one lidar survey. We

recommend the results of this study to be considered in developing projects and national level MRV systems for REDD+ emission reduction programs for tropical forests.

Keywords: lidar; humid tropical forest; biomass change; pulse density; MRV

3.1 Introduction

The Amazon is the largest remaining tropical forest in the world, however, its original extent has been steadily reduced due to deforestation and forest degradation, although deforestation rates in Brazil have decreased by 70% since 2004 (Hansen et al., 2013; Neptad et al., 2014). In recent decades, selective logging of valuable tree species has been an important land use of tropical forest in the Brazilian Amazon (Matricardi et al., 2010; Vidal et al., 2016). Selective logging timber extraction removes only the most valuable tree species from the forest (Hansen et al., 2013). It contributes substantially to gross carbon fluxes from the Brazilian Amazon and in other tropical regions as well (Asner et al., 2005). Selective logging has continued apace with degradation from forest fires and forest fragmentation, and may also degrade the Amazon forest through long term changes in structure, loss of forest carbon and species diversity (Longo et al., 2016). Characterizing the spatial distribution of forest structure, aboveground biomass (AGB), and AGB changes are important prerequisites for understanding carbon cycle dynamics and for monitoring the impact of selective logging in tropical forests over time (d'Oliveira, 2012). Accurate, landscape-wide estimates of AGB stocks and changes from selective logging in tropical forest are also desired for ongoing climate mitigation efforts to Reduce Emissions from Deforestation and Forest Degradation (REDD+) and for Measuring, Report and Verification (MRV) systems (d'Oliveira, 2012; Andersen et al., 2014).

Airborne lidar is a technology well-suited to measure forest structure and estimate AGB stocks and changes in tropical forests (e.g., Andersen et al., 2014; Asner et al., 2014; Drake et al., 2002a; Drake et al., 2002b; Dubayah et al., 2010; Meyer et al., 2013). Lidar can provide high resolution, three-dimensional information on forest structure and the underlying topography (Silva et al., 2016). Recently, d'Oliveira et al. (2012) and Andersen et al. (2014) have used airborne lidar for detecting selective logging activities and mapping

AGB stocks and changes in the Brazilian Amazon forest. To monitor selective logging impacts on forest structure and AGB changes over large areas, multiple lidar data acquisitions must be acquired that increase the cost of data collection and processing over time. Many factors influence the cost of lidar data, including variables such as project size, location and deliverables, as well as market variables, such as competition amongst lidar vendors. A major variable that affects the cost of acquisition of lidar data is the pulse density (Magnusson et al., 2007), defined as the number of pulses emitted by the sensor per m^2 (pulses·m^{-2}) (Evans et al., 2009). As pulse density increases, so does acquisition cost, due to the direct link between pulse density, aircraft altitude and flight time (Jakubowski et al., 2013; Le Quéré et al., 2015).

While airborne lidar can facilitate timely and accurate estimates of forest structure in tropical forest, trade-offs still exist between lidar pulse density and accuracy. For instance, it is unclear how much the lidar pulse density can be reduced and still maintain an adequate level of accuracy for AGB change estimation in tropical forests. Leitold et al. 2015 and Ota et al. 2015 have carried out studies to examine the relationship between lidar pulse density and AGB stock estimation accuracy in tropical forests. Even though they found that AGB can be accurately estimated from lidar using low-pulse density, neither of these authors assessed the impact of pulse density on estimating and mapping AGB stocks and AGB change at landscape level, and in the context of selectively logged tropical forest. Here, we focus on the impacts of pulse density in estimating AGB change in tropical forests and provide recommendations for specification of lidar data acquisitions for forest monitoring, REDD+ projects and MRV systems. We work with data collected in an eastern selectively logged Amazonian forest and lidar data with high pulse density acquired in 2012 and 2014. The study quantifies how reduced pulse density reduces the accuracy of AGB stock and AGB change estimation at plot and landscape levels. We evaluate accuracy based on lidar data acquired over dense tropical forests with variations of terrain characteristics and topography. The results of our study are then discussed in the context of implementation of airborne lidar systems in monitoring forest AGB change for REDD+ and emission reduction programs.

3.2 Material and Methods

3.2.1. Study Area

The study was conducted at the Fazenda Cauaxi in the Paragominas Municipality of Pará State, Brazil, in the eastern Amazon (Figure 3.1). The climate of the Cauaxi region is typically humid, with an average annual temperature of about 25 °C and an average annual precipitation of 2200 mm, which primarily falls between the months of January and June (Alvares et al., 2013). The forest is predominantly classified as tropical dense moist forest (IBGE, 2004). The terrain ranges from flat to steep slopes and the soils within the region are classified predominately as dystrophic yellow latosols following the Brazilian classification system (RadamBrazil 1983). The study area is divided into 12 logging units, where ten of them have been logged through the reduced-impact logging (RIL) since 2007 and the remaining two are still unlogged (Figure 3.1d).

3.2.2. Field Data Collection

A total of 22 field transects of 20 × 500 m were stratified randomly across the study area in 2012, and 88 plots of 50 × 50 m (0.25 ha) were spaced at 100 m intervals along the transects in 2014. In the field, plot corners were registered using differential GNSS (GeoXH6000, Trimble Navigation, Ltd., Dayton, OH, USA). At each plot, a sub-plot (strip) along one side of the plot with dimensions of 5 × 50 m (250 m^2) was also demarcated. Because three of the plots were not covered by the lidar data, we selected 85 plots for further analysis. For each plot, all living trees with diameter at breast height (dbh) ≥ 35 cm were identified by parataxonomists familiar with the flora of the region and their dbh measured. In the sub-plots, all trees with dbh ≥ 10 cm were measured. Dbh was measured at 1.3 m above ground or above buttresses. A total of 1757 living trees were measured. The AGB (kg) of each tree was estimated using the Chave et al. 2014 Equation (3.1).

$$\text{AGB (kg)} = exp[-1.803 - 0.976\text{E} + 0.976\ln(\rho) + 2.673\ln(\text{dbh}) - 0.0299[\ln(\text{dbh})]^2)] \quad (3.1)$$

where AGB (kg) is the live tree aboveground biomass in Kg; dbh is the diameter at breast height (1.30 m); $\boldsymbol{\rho}$ is the wood density and E is a measure of environmental stress. In this study area location E = −0.103815.

The total live aboveground biomass (AGB) of the plots and sub-plots was obtained by aggregating the individual tree biomass values and converting to $Mg \cdot ha^{-1}$. The summary of the dbh and AGB measurements in 2014 at the sample plots is presented in Table 3.1.

3.2.3. Lidar Data Acquisition and Processing

Airborne lidar data were collected as part of Sustainable Landscapes Brazil, a joint project of the Brazilian Corporation of Agricultural Research Corporation (EMBRAPA) and the United States Forest Service. The first lidar acquisition occurred in July of 2012 with a pulse density of 13.8 $pulses \cdot m^{-2}$, with the second lidar collection in December of 2014 with a pulse density of 37.5 $pulses \cdot m^{-2}$. The total area covered by the lidar survey for the multitemporal analysis was 1200 ha. The data attributes of the lidar sensor and flight characteristics are listed in Table 3.2.

The lidar data processing can be summarized in three steps:

(i) *Lidar data thinning*: Lidar data from both 2012 and 2014 were thinned from the original pulse density of 13.8 and 37.5 $pulses \cdot m^{-2}$ to lower densities of 12, 10, 8, 6, 4, 2, 0.8, 0.6, 0.4 and 0.2 $pulses \cdot m^{-2}$. An example of the pulse density reduction is shown in Figure 3.2. The reduction of pulse density was executed using the algorithm implemented in the ThinData utility of the FUSION toolkit (McGauchey 2015). The algorithm first identifies all the returns that belong to a pulse, and randomly reduces the number of pulses until achieving the desired pulse density within a certain grid cell size (e.g., in this case 50 m). To evaluate the uncertainty in the thinning process, we generated 30 random replicates for each lidar dataset and target density.

(ii) *Digital terrain models and lidar data above ground height normalization:* Ground returns were classified using the Progressive Triangulated Irregular Network (TIN) densification algorithm implemented in lasground (Isenburg 2016) (settings: step is 10 m, bulge is 0.5 m, spike is 1 m, offset is 0.05 m), and 1 m DTMs were created for each of

the reduced pulse density datasets using the blast2dem utility in Lastools [25]. Afterwards, the lidar datasets were normalized to height aboveground by subtraction of the DTM elevation from the Z coordinate of each return projected above the ground. In particular, the impacts of pulse density were assessed under two DTM scenarios. First, under the DTM scenario DS1, where the lidar datasets from both 2012 and 2014 were height normalized using the DTMs created from their respective thinned dataset. Second, under the DTM scenario DS2, where to simulate the impact of pulse density on subsequent acquisition, the DTMs generated at the highest pulse density (37.5 pulse·m^{-2}) from 2014 were used to normalize the lidar datasets from both 2012 and 2014.

(iii) *Lidar-derived Mean Height (HMEAN):* In this study, HMEAN, the mean height of all returns above 1.3 m in height, was computed at plot and landscape levels. Herein, even though the plot corners were geolocated with differential GNSS to within < 1 m in most cases (Longo et al., 2016), we chose to optimize plot location to reflect canopy conditions. It is common to find trees with crown diameters larger than 30 m in the study area. When large tree stems are found outside of a plot, substantial proportions of their crowns may fall inside a plot thereby influencing lidar metrics such as HMEAN. To avoid these effects, we iteratively shifted each plot within a 25 m square neighbourhood on the lidar canopy height model (CHM) for improved co-registration, and consequently to achieve a better correlation between AGB and HMEAN. After this procedure, we observed that the plot centers were moved an average of 18.38 m (sd ± 6.32 m) from the initial plot locations. Finally, at the landscape level, HMEAN was computed in grids with a cell size of 50 m × 50 m.

3.2.4. Aboveground Biomass Change Estimation and Mapping

For both DTM scenarios described in Section 2.3, we used the *nls* function in R (R Core Team 2016) to calibrate the relationship between plot level AGB measurements and lidar-derived HMEAN. Non-linear least-squares regression models (the power-law models) were used to model AGB across 30 replicates of each reduced target density in 2014, and used to predict and map AGB stocks in 2012 (AGB_{2012}) and 2014 (AGB_{2014}) at plot and landscape

levels. The AGB change ($\Delta AGB_{(2014-2012)}$) estimation was then computed as the difference in AGB prediction from 2012 to 2014.

$$\mathrm{AGB}_{2014} = a_{2014} * \mathrm{HMEAN}_{2014}{}^{b_{2014}} \quad (3.2)$$

$$\mathrm{AGB}_{2012} = a_{2014} * \mathrm{HMEAN}_{2012}{}^{b_{2014}} \quad (3.3)$$

$$\Delta AGB_{(2014-2012)} = \mathrm{AGB}_{2014} - \mathrm{AGB}_{2012} \quad (3.4)$$

where $\boldsymbol{a_{2014}}$ and $\boldsymbol{b_{2014}}$ are the estimates' parameters of the power-law models in 2014. Leave-one-out cross-validation (LOOCV) was developed (e.g., Silva et al., 2016), and the prediction precision of the LOOCV models was evaluated in terms of the coefficient of determination (R^2), absolute and relative Root Mean Square Error (RMSE), and absolute and relative bias from the linear relationship between observed and LOOCV predicted AGB values:

$$\mathrm{RMSE} = \sqrt{\frac{\sum_{i=1}^{n}(\hat{y}_i - y_i)^2}{n}} \quad (3.5)$$

$$\mathrm{Bias} = \frac{1}{n}\sum_{i=1}^{n}(\hat{y}_i - y_i) \quad (3.6)$$

where *n* is the number of plots, y_i is the observed value for plot *i*, and $\hat{y}_i$ is the predicted value for plot *i*. Moreover, relative RMSE and bias were calculated by dividing absolute RMSE and bias (Equations 3.5 and 3.6) by observed AGB mean. In order to have prediction accuracy equal to or higher than a conventional forest inventory in tropical forest, we defined accepted model accuracy as relative RMSE and bias of ≤ 20%.

At the landscape level, maps representing the mean and standard deviation of AGB stocks and AGB changes from the 30 replications were calculated and used as final estimates to assess the impact of pulse density. The mean of AGB stocks in 2012 and 2014 and AGB changes from the final maps were computed as follows:

$$\widehat{AGB}_{2012} = \frac{1}{n}\sum_{k=1}^{n} \mathrm{AGB}_{k\,2012} \tag{3.7}$$

$$\widehat{AGB}_{2014} = \frac{1}{n}\sum_{k=1}^{n} \mathrm{AGB}_{k\,2014} \tag{3.8}$$

$$\Delta\widehat{AGB}_{(2014-2012)} = \frac{1}{n}\sum_{k=1}^{n} \Delta AGB_{k\,(2014-2012)} \tag{3.9}$$

where $\widehat{AGB}_{2012}$, $\widehat{AGB}_{2014}$ and $\Delta\widehat{AGB}_{(2014-2012)}$ are the mean estimated AGB stock in 2012 and 2014 and mean estimated AGB change, respectively. $\mathrm{AGB}_{k\,2012}$, $\mathrm{AGB}_{k\,2014}$ and $\Delta AGB_{k\,(2014-2012)}$ are the predicted AGB stocks in 2012 and 2014 and their changes at the pixel *k*, respectively.

An uncertainty analysis of the $\widehat{AGB}_{2012}$ and $\widehat{AGB}_{2014}$ at landscape level for each pulse density target and DTM scenario was also performed by integrating the pixel level errors and accounting for spatial autocorrelation of the errors as follows (McRoberts 2006; Weisbin et al., 2014; Garcia et al., 2017):

$$\widehat{\sigma^2_{AGB}} = \frac{1}{m^2}\sum_{i=1}^{m}\sum_{j=1}^{m} cov(\sigma_i,\sigma_j) = \frac{1}{m^2}\left(\sum_{i=1}^{m}\sigma_i^2 + 2\sum_{i=1}^{m}\sum_{i<j}^{m}\rho(d)\,\sigma_i\sigma_j\right) \tag{3.10}$$

where $\widehat{\sigma^2_{AGB}}$ is the variance of the estimator for the mean AGB stock for the entire study area; *m* is the number of pixels in the area; $\rho(d)$ is the spatial autocorrelation function of the distance, *d*, based on an exponential semi-variogram model; and σ_i is the estimated standard error of AGB stock values at the i-th pixel.

The variance of the estimator of the mean $\widehat{\sigma^2_{\Delta AGB}}$ at landscape level was computed as:

$$\widehat{\sigma^2_{\Delta AGB}} = \widehat{\sigma^2_{AGB(2012)}} + \widehat{\sigma^2_{AGB(2014)}} - 2Cov\left(\widehat{AGB_{2012}}, \widehat{AGB_{2014}}\right). \tag{3.11}$$

where the variances ($\widehat{\sigma^2_{AGB(2012)}}$ and $\widehat{\sigma^2_{AGB(2014)}}$) were computed as described in Equation (3.10) and the cross-time covariance of the AGB was computed according to McRoberts et al., (2014):

$$cov(AGB_{2012}, AGB_{2014}) = \frac{1}{m^2}\sum_{i=1}^{m}\left(\sigma_{i(2012)} - \widehat{\sigma_{i(2012)}}\right)\left(\sigma_{i(2014)} - \widehat{\sigma_{i(2014)}}\right) \qquad (3.12)$$

3.2.5. Assessing Effects of Pulse Density on Lidar-Derived Mean Canopy Height

As the HMEAN values vary from one replication to another for a given plot and target density, we calculated the mean and standard deviation of HMEAN at the plot level across the 30 repetitions. The impacts of pulse density on HMEAN at plot level was then evaluated by the reliability ratio, which is the ratio of the variance of HMEAN among sample plots, to the total variance of the HMEAN across 30 repetitions (Fuller, 1987):

$$\text{Reliability ratio (RR)} = \frac{S_u^2}{S_u^2 + S_w^2} \qquad (3.13)$$

where S_u^2 is the estimated among-plot variance of HMEAN and S_w^2 is the estimated average within-plot variance. Reliability ratio ranges from 0 (no reliability) to 1 (complete reliability), and large replication variance makes HMEAN a low reliability predictor of AGB.

3.2.6. Assessing Impacts of Pulse Density on the Aboveground Biomass Stocks and Change Estimation at the Plot and Landscape Levels

The impacts of the lidar pulse density on AGB stocks and AGB change estimations were assessed at the plot level by comparing the R^2, relative and absolute RMSE and bias across pulse densities and DTM scenarios. Boxplots were created to compare the variability of LOOCV AGB stock estimates, RMSE and bias at plot level. Because we built a model for each repeated dataset and target density, we also calculated the mean and standard deviation of the a_{2014} and b_{2014} model parameters. The two-sided Kolmogorov-Smirnov (KS) (R

Core Team 2016) test was used to test if the distributions of the HMEAN, observed and LOOCV AGB stock estimates in 2014 differed significantly, with significance level of 0.05, across pulse densities and DTM scenarios. Moreover, besides the maps of AGB stock and changes, we created a map of the slope over the study area, and the impacts of the lidar pulse density on AGB stocks and change estimations were evaluated by the difference on the AGB estimates from 12 pulses·m^{-2} to lower pulse densities, in each DTM scenario and across slope gradients of 0 to 12%; 12 to 24% and 24 to 35%. An overview of the methodology is outlined in Figure 3.3.

3.3 Results

3.3.1. Impacts of Lidar Pulse Density on Mean Canopy Height (HMEAN)

The impacts of the pulse density on the lidar derived HMEAN at plot level are shown in Figure 3.4. The mean of HMEAN among plots slightly varied from 20.47 (±2.89) to 20.93 (±2.93) m and 20.32 (±2.90) to 20.33 (±2.91) m for DS1 and DS2 in 2012, and from 20.77 (±2.77) to 20.92 (±2.87) m and 20.77 (±2.74) to 20.78 (±2.75) m for DS1 and DS2 in 2014, respectively. In 2014 the HMEAN variation among-plots was slightly higher than 2012, however, HMEAN was not significantly affected by pulse density and DTM scenario in both years (KS: $D \geq 0.014$, p-value > 0.05) (Figure 3.4 (a1,a2)). The variability of HMEAN represented by the standard deviation (Figure 3.4 (b1,b2)) within plots for the 30 replications was larger at lower than at higher pulse densities for both DTM scenarios and years. Reduced pulse density resulted in a decreased reliability ratio (RR); however, RR still showed high stability of HMEAN across DTM scenarios and years with RR values higher than 0.96 (Figure 3.4 (c1,c2)).

3.3.2. Effects of Lidar Pulse Density on AGB Modelling

The parameters a_{2014} and b_{2014} of the models adjusted in 2014 to predict AGB from lidar-derived HMEAN for 2014 across scenarios and pulse densities are presented in Table 3. Reduced pulse density resulted in increased variation of these parameter values in both scenarios, where DS2 showed less variation then DS1. For DS1 the mean of model

parameters a_{2014} and b_{2014} showed significant differences (KS: D ≥ 0.40, p-values ≤ 0.015) at pulse densities ranging from 0.2 to 4 pulses·m^{-2} compared to the value at 12 pulses·m^{-2}; for DS2, significant differences from 12 pulses·m^{-2} (KS: D ≥ 0.46, *p*-values < 0.002) were found only at pulse densities ranging from 0.2 to 2 pulse·m^{-2}. Both parameters a_{2014} and b_{2014} showed significant differences (KS: D ≥ 0.47, *p*-values ≤ 0.002) at pulse densities ranging from 0.2 to 2 pulse·m^{-2} when compared at the same pulse density, but across scenarios.

The performance of the models to estimate AGB stock in 2014 was further assessed by leave-one-out cross-validation. The HMEAN was an important lidar metric to explain AGB stock variation. Reduced pulse density resulted in decreased R^2 and increased relative and absolute RMSE and bias for both DTM scenarios, particularly for DS1 (Figure 3.5). Mean R^2 values ranged from 0.60 (±0.09) to 0.73 (±0.00) and 0.71 (±0.02) to 0.73 (±0.00) across pulse densities in DS1 and DS2, respectively, and showed significant differences (KS: D ≥ 0.37, *p*-value ≤ 0.034) at pulse densities ranging from 0.2 to 6 pulse·m^{-2} and from 0.2 to 2 pulse·m^{-2} compared to the results at 12 pulses·m^{-2} in DS1 and DS2, respectively (Figure 5a). Mean relative RMSE values ranged from 18.81 (±0.06) to 22.80 (±0.270) % and 18.81 (±0.06) to 19.50 (±0.69) %, across pulse densities in DS1 and DS2, respectively, and also showed significant differences (KS: D ≥ 0.37, *p*-values < 0.035) at pulse densities ranging from 0.2 to 6 pulse·m^{-2} and from 0.2 to 2 pulse·m^{-2} compared to the value at 12 pulses·m^{-2} in DS1 and DS2, respectively (Figure 3.5(b1)). Bias was less affected by pulse density in DS2 than in DS1 (Figure 5(c1)). While mean bias across pulse densities ranged from −0.48 (±0.38) to −0.04 (±0.01) % in DS1, and showed significant differences (KS: D ≥ 0.57, *p*-values < 0.001) at pulse densities ranging from 0.2 to 2 pulse·m^{-2} compared to at 12 pulses·m^{-2}, mean bias remained constant around 0.04% in DS2, and showed significant differences (KS: D ≥ 0.43, *p*-values < 0.006) only at pulse densities ranging from 0.2 to 0.6 pulse·m^{-2} when compared to 12 pulses·m^{-2}.

3.3.3. Impacts of Lidar Pulse Density on AGB Stocks and AGB Change Estimation at the Plot and Landscape Levels

The AGB stocks estimates from the leave-one-out cross-validation at plot level are presented in Figure 3.6. In 2012, mean predicted AGB ranged from 226.81 (±76.29) to 230.35 (±75.98) $Mg \cdot ha^{-1}$ and from 226.51 (±75.78) to 227.02 (±74.46) $Mg \cdot ha^{-1}$ across pulse densities for DS1 and DS2, respectively, and significant differences (KS: $D \geq 0.035$, *p*-value ≤ 0.03) were found at pulse densities ranging from 0.2 to 0.4 $pulse \cdot m^{-2}$ compared to the value at 12 $pulses \cdot m^{-2}$, but only in DS1. In 2014, mean predicted AGB ranged from 237.83 (±74.37) to 238.89 (±70.21) $Mg \cdot ha^{-1}$ and 273.83 (±74.28) to 273.84 (±73.43) $Mg \cdot ha^{-1}$ across pulse densities for DS1 and DS2, respectively, and significant differences (KS: $D \geq 0.04$, *p*-value ≤ 0.015) were found only at pulse densities ranging from 0.2 to 0.4 $pulse \cdot m^{-2}$ compared to the value at 12 $pulses \cdot m^{-2}$, but only in DS1 as well (Figure 3.6(a1,a2)).

The estimated AGB change among plots ranged from −163.845 to 354.29 $Mg \cdot ha^{-1}$ and from −159.79 to 155.46 $Mg \cdot ha^{-1}$ across pulse densities for DS1 and DS2, respectively. The estimated mean AGB change among plots only ranged from 7.05 (±42.20) to 7.50 (±60.20) $Mg \cdot ha^{-1}$ and 10.83 (±41.42) to 11.01 (±38.68) $Mg \cdot ha^{-1}$ across pulse densities for DS1 and DS2, respectively, and significant differences (KS: $D \geq 0.38$, *p*-values ≤ 0.042) were found at pulse densities ranging from 0.2 to 0.8 $pulse \cdot m^{-2}$ and from 0.2 to 0.6 $pulse \cdot m^{-2}$ compared to 12 $pulses \cdot m^{-2}$ in DS1 and DS2, respectively. The reduced pulse density increased the variance of the AGB estimates within plots across the 30 replicates, and showed significant differences (KS: $D \geq 0.59$, *p*-values < 0.001) in the standard deviation of AGB stocks and changes, from 0.2 to 0.8 $pulse \cdot m^{-2}$ compared to the value at 12 $pulses \cdot m^{-2}$. DS2 shows slightly less variation than DS1, but after pulse density reaches values higher than 0.8 $pulses \cdot m^{-2}$, both scenarios show very low and not significant differences in standard deviation of AGB stocks and changes within plots across replicates.

Landscape-wide AGB stock and change estimations were mapped at a 50 m × 50 m grid cell size based on the mean of the 30 replicated AGB maps derived in 2012 and 2014, and their AGB changes (Figures 3.S1–3.S3). Reduced pulse densities and DTM scenarios did not affect mean predicted AGB at landscape level, and showed no statistically significant differences (KS: $D \leq 0.02$, *p*-value > 0.05). The AGB stocks at landscape level in

2012 and 2014 ranged from 43.90 to 811.33 Mg·ha^{-1} and from 42.42 to 853.00 Mg·ha^{-1}, respectively, while predicted AGB changes ranged from −406.78 to 177.00 Mg·ha^{-1} in DS2 at 12 pulses·m^{-2} (Figure 3.7a–c). The estimated mean AGB change for the entire study area ranged from 15.88 (±33.09) to 19.69 (±37.71) Mg·ha^{-1} and 22.58 (±37.22) to 23.26 (±38.25) Mg·ha^{-1} across pulse densities for DS1 and DS2, respectively. Figure 3.7c,d show the AGB changes in an unlogged and logged unit at 0.2 and 12 pulses·m^{-2} in DS1 while Figure 3.7e,f show the AGB changes in the same logged units and pulse density, but in DS2. The estimated mean AGB stocks and AGB changes and their uncertainties across pulse density and DTM scenarios are presented in Table 3.4.

Landscape-wide standard deviation of estimated AGB change was also mapped at a 50 m × 50 m grid cell resolution (Figure 3.8c,d and Figure 3.S4); reduced pulse density increased variation in estimated AGB change within replicates, and showed large standard deviation of AGB at 0.2 pulses·m^{-2}, for both DS1 and DS2 (Figure 3.8(c1,d1)). In general, the standard deviation of estimated AGB change was higher in DS1 than DS2. Landscape-wide elevation and slope were also mapped (Figure 3.8a,b), and for both DS1 and DS2 the large variability in AGB change occurred in high slope areas, reaching up to 33 Mg·ha^{-1} in areas with slopes ranging from 24 to 36% (Figure 3.8(c1)).

Estimated AGB change at landscape level at pulse densities ranging from 0.2 to 10 pulses·m^{-2} were compared with those estimates at 12 pulses·m^{2} across slopes and DTM scenarios (Figure 3.9a–c). In general, when compared with the AGB change estimates from 12 pulses·m^{-2}, reduced pulse density underestimated AGB change at landscape level in areas with slopes higher than 12% and showed significant differences (KS: $D \geq 0.45$, *p*-value > 0.001) at pulse densities ranging from 0.2 to 0.8 pulses·m^{-2}, but only for DS1 at slopes of 12–24% (Figure 3.9b) and 24–35% (Figure 3.9c). At slopes of 0–12% (Figure 3.9a), reduced pulse density increased the difference in AGB change when compared with those estimates at 12 pulses·m^{2} in both DS1 and DS2, but their differences were no higher than 20 Mg·ha^{-1} (Figure 3.9a).

3.4. Discussion

This research assessed the impact of lidar pulse density on AGB stocks and changes estimations in an Amazon tropical forest. Previous studies have evaluated the impact of lidar pulse density on forest attribute estimation from lidar data (e.g., Hansen et al., 2015; Magnussen et al., 2010; Strunk et al., 2012), yet few studies have evaluated the impacts of lidar pulse density on forest AGB stock estimates in tropical forest (Leitold et al., 2015; Ota et al., 2015; Singh et al., 2015). To our knowledge, this is the first study to assess the impact of airborne lidar pulse density on AGB stocks and AGB change estimations in tropical forest, and in the context of using an airborne lidar system in selective logging for monitoring forest AGB change for REDD+ and emission reduction programs.

Many lidar-derived metrics have been used for modelling forest attributes (e.g., Næsset 2001; Næsset 2002; Næsset et al., 2008; Hudak et al., 2012; d'Oliveira et al., 2012; Silva et al., 2014; Silva et al., 2017b). Hansen et al., (2015) evaluated the effects of lidar pulse density on DTM and canopy structure metrics in a tropical forest and showed also that HMEAN was one of the most stable predictor variables for modelling forest attributes using airborne lidar data. In our study, under both DTM scenarios, reduced pulse density did not significantly affect the variability of HMEAN among plots. Magnusson et al., (2010) recommended a calibration of lidar models when the reliability ratio (RR) of one or more predictors is below 0.9. In our study, even though reduced pulse density increased the standard deviation of HMEAN within plots, the RR of HMEAN across all pulse densities and both DTM scenarios remained very high (RR > 0.9). Therefore, further calibration of models was not necessary. This is not surprising given that HMEAN, unlike other metrics such as the top mean canopy height (MCH), considers all returns above a certain height threshold (e.g., 1.37 m) to compute a vertical mean height, and therefore uses more information to describe the canopy structure. Unlike MCH, HMEAN is computed directly from the point cloud, and does not have any influence of CHM interpolation methods or grid cell size. Garcia et al., (2017) assessed the impact of lidar point density on the prediction of AGB across different forest ecosystems and found that predictions were more affected when using CHM-derived metrics then those computed directly from the 3D point cloud, even if the point density was as low as 1 point$\cdot m^{-2}$. Herein, we simulated low pulse density lidar

datasets by removing pulses randomly, however, other approaches of removing lidar pulses have also been found in the literature (Magnusson et al., 2007; Jakubowski et al., 2013; Le Quéré et al., 2015; Leitold et al., 2015; Magnussen et al., 2010; Tesfamichael et al., 2010) and may lead to different outcomes when considering the covarying effect of pulse density when survey parameters are changed. Nevertheless, our results on HMEAN variation patterns agree with a previous study (Hansen et al., 2015), and independent of the approach used, a realistic thinning approach on real lidar data is always extremely challenging (Lovell et al., 2005).

In addition to the high stability, HMEAN correlated well with AGB, and we obtained linear relationships between observed and predicted AGB via LOOCV that explained at least 40% of the variation at the lowest pulse density (0.2 pulses·m^{-2}) in DS1, for example. For comparison purposes, the R^2 values were substantially greater than adjusted $R^2 = 0.43$ obtained by Leitold et al., (2015) using a regression model for predicting AGB stocks in the Brazilian Atlantic forest, but similar to those reported by d'Oliveira et al., (2012) and Andersen et al., (2014) using lidar for detecting and quantifying AGB changes in selective logging in western Amazonia, respectively. Herein, a substantial decrease in R^2 and increase in RMSE and bias occurred when the pulse density was reduced from 12 pulses·m^{-2} to pulse densities lower than 2 pulses·m^{-2}. For instance, AGB models under DS1 were much more affected at pulse densities ≤2 pulses·m^{-2}. Magnusson et al. (2010) and Watt et al., (2014) in mixed conifer forests also evaluated the effect of lidar pulse density on the prediction accuracy of forest attributes under DS1 and DS2, and found increased RMSE at relatively low pulse densities. However, similar to findings by those authors, our predictions were more affected in DS1 than DS2. Nevertheless, in both scenarios, AGB stocks were underestimated. An underestimation of AGB stock with reduced pulse density was also found in Leitold et al., (2015), but as AGB stocks at low pulse densities were estimated from a single model adjusted at high pulse density, the author attributed the underestimation to a systematic error in the DTM propagated to the canopy. Herein, the underestimation in AGB stock in DS1 is attributed to the deterioration of the DTM and HMEAN quality due to combined random effects derived from pulse density reduction, while in DS2, the underestimation in AGB stock is only attributed to the poor HMEAN quality. Moreover, as

we kept a constant interpolation method and grid size for DTM modeling in DS1 and DS2 as in Magnusson et al., (2010) and Watt et al., (2010), the pulse density is the only factor affecting the DTM and HMEAN quality. Therefore, the differences in R^2, RMSE and bias between DS1 and DS2 were only attributable to the deteriorating DTM and HMEAN quality.

In this study, we mapped AGB change at the landscape level at a spatial resolution of 50 m. Therefore, unlike most previous studies (e.g., Hansen et al., 2015; Magnussen et al., 2010; Strunk et al., 2012), we not only evaluated the impact of pulse density on AGB stocks estimation at plot the level, but also at the landscape scale. Andersen et al., (2014) used repeated lidar flights to monitor selective logging in western Amazonia, and AGB stock and changes maps were accurately derived from lidar data acquired in 2010 and 2011 with pulse densities of 25 pulses·m^{-2} and 14 pulses·m^{-2}, respectively. In the study, the authors found that multi-temporal lidar data can be used to detect and quantify AGB changes due to selective logging activities, even when the level of AGB change is low (10–20 Mg·ha^{-1}). While the pulse density was appropriate for the study, they are not economically feasible for large-area acquisitions and for monitoring selective logging over time. Hansen et al., (2015) suggest that canopy metrics derived from sparse pulse density ALS data can be used for AGB estimation in a tropical forest; however, the authors either estimated AGB or expanded the analysis to landscape level in their studies. Wilkes et al., (2015) found that structural metrics (canopy height, canopy cover and vertical canopy structure) derived from pulse densities < 0.5 pulses·m^{-2} returned larger differences, particularly for tropical forest. Herein, while our uncertainty analysis showed that reduced pulse density did not affect the accuracy of mean estimated AGB change at the landscape level in both DTM scenarios, reduced pulse density did significantly affect the standard deviation of estimated AGB change at the local scale, especially in areas of steeper slopes. However, this effect was only observed for the DS1 scenario at pulse densities ≤ 0.8 pulses·m^{-2}. Variation in AGB estimates increased with decreasing pulse density; this is illustrated by mapped standard deviation at landscape level (Figure 3.8).

From a carbon monitoring perspective, our results show that it is not necessary to acquire lidar data with pulse density higher than 0.2 pulses·m^{-2} for mapping AGB stocks

and AGB change in selective logging areas in the Amazonia when a DTM is already available from previously flown high pulse density airborne lidar. In cases where no such DTM already exists, our results suggest that a lidar data acquisition with a minimum pulse density of 2 pulses·m^{-2} is necessary. Furthermore, we have demonstrated that it is possible to capture AGB stocks and AGB change variability at the stand level even in steep terrain with low pulse density lidar under DS2 and with pulse density equal to or higher than 2 pulses·m^{-2} in DS1. Despite the change in AGB stocks, selective logging can also substantially alter forest structure and affect tree survival, growth, and recruitment rates for up to a decade post-harvest (Shenkin et al., 2015). In this study, we did not evaluate the impact of pulse density for detecting forest impacts associated with selective logging, nor the combined effect of pulse density and plot size on AGB change estimation. Therefore, we suggest caution when acquiring new lidar datasets, because the accuracy of the AGB change estimates in selective logging areas may depend also on other factors, such as plot and grid cell sizes for sampling and mapping, which were not evaluated in this study. In some small, randomly distributed areas, AGB change was highly overestimated (AGB change ≥ 100 Mg·ha^{-1}), which is not biologically possible in only two years. These overestimates could result from subtracting AGB stocks predicted from models calibrated with only 2014 data, and may not have resulted had independent AGB models been calibrated with data from both years (e.g., Hudak et al., 2012). Also, these overestimates could be attributable to small co-registration errors (<0.5 pixel) between the two lidar surveys, but this would lead to a comparable number of randomly distributed underestimates. In summary, it is unlikely that these errors would alter the sensitivity analysis to pulse density.

Although a quantitative evaluation of lidar data acquisition cost was not a central objective in this study, it is nonetheless an important factor to consider because it can be a primary factor driving choices made about forest and AGB monitoring across a wide range of spatial scales. Because pulse density has a strong influence on the acquisition cost of lidar data, and even though the cost for using lidar with high or low pulse density for AGB in tropical forest might be lower than the cost of a conventional inventory (Hummel et al., 2015), airborne lidar can be cost prohibitive for forest carbon monitoring, in selected logged areas for REDD+ at large spatial extents. Although field-based AGB estimations remain

necessary for these purposes, integrating lidar remote sensing into AGB inventory schemes allows recovery of carbon content and spatially-explicit estimates across landscapes, while reducing the total costs and need for extensive field-based sampling.

3.5. Conclusions

We evaluated the impacts of airborne lidar pulse density on AGB stocks and AGB change estimation in a selectively logged Amazon tropical forest. First, we confirmed that HMEAN is a stable lidar-derived metric for estimating AGB stock in selective logging. Second, we found that the accuracy of AGB stocks and AGB change estimates decreased as the pulse density decreased, but it remained relatively high except at low pulse densities of 0.8 and 0.2 pulses·m^{-2} for the DS1 and DS2 scenarios, respectively. Furthermore, AGB stocks estimations at the landscape level were strongly underestimated at pulse densities lower than 0.8 pulses·m^{-2} in areas with steep slopes, but only in DS1, where the lidar datasets from both 2012 and 2014 were height normalized using the DTMs created from their respective thinned dataset. Therefore, these results demonstrate that high lidar pulse density is not necessary to estimate and map AGB stock and changes in selective logging in tropical forest, especially when there is already an accurate DTM derived from high pulse density lidar. Third, we showed that low pulse density lidar data (~2 pulses·m^{-2}) has the ability to map ground topography, allowing accurate estimation of canopy height even over rough terrain and as a baseline for subsequent low density lidar acquisition for AGB change studies. Lower point densities can cover larger areas at reasonable cost and be used to complement satellite remote sensing measurements, e.g., NISAR—National Aeronautics and Space Administration-Indian Space Research Organization Synthetic Aperture Radar (http://nisar.jpl.nasa.gov) and GEDI—Global Ecosystem Dynamics Investigation (http://science.nasa.gov/missions/gedi/), that may have limitations in estimating tree height in areas with complex topography. Finally, although we focus on AGB stocks and AGB change estimation in a selectively logged tropical moist forest in Brazil, our methodology may also be applicable for inventorying and monitoring AGB changes to support REDD+ monitoring efforts in selective logging elsewhere across the tropics.

References

Asner, G.P.; Knapp, D.E.; Broadbent, E.N.; Oliveira, P.J.; Keller, M.; Silva, J.N. (2005). Selective logging in the brazilian Amazon. *Science*, *310*, 480–482, doi:10.1126/science.1118051.

Andersen, H.E.; Reutebuch, S.E.; McGaughey, R.J.; d'Oliveira, M.V.N.; Keller, M. (2014). Monitoring selective logging in western Amazonia with repeat lidar flights. *Remote Sens. Environ.*, *151*, 157–165, doi:10.1016/j.rse.2013.08.049

Asner, G.P.; Mascaro, J. (2014). Mapping tropical forest carbon: Calibrating plot estimates to a simple lidar metric. *Remote Sens. Environ.*, *140*, 614–624, doi:10.1016/j.rse.2013.09.023.

Alvares, C.A.; Stape, J.L.; Sentelhas, P.C.; Gonçalves, J.L.M. (2013). Modeling monthly mean air temperature for Brazil. *Theor. Appl. Climatol.*, *113*, 407–427, doi:10.1007/s00704-012-0796-6.

Chave, J., M. Rejou-Mechain, A. Burquez, E. Chidumayo, M. S. Colgan, W. B. Delitti, A. Duque et al. (2014) Improved allometric models to estimate the aboveground biomass of tropical trees. Global Change Biology, 20, 3177–3190, doi: 10.1111/gcb.12629

Drake, J.B.; Dubayah, R.O.; Clark, D.B.; Knox, R.G.; Blair, J.B.; Hofton, M.A.; Chazdon, R.L.; Weishampel, J.F.; Prince, S. (2002). Estimation of tropical forest structural characteristics using large-footprint lidar. *Remote Sens. Environ.*, *79*, 305–319, doi:10.1016/S0034-4257(01)00281-4.

Drake, J.B.; Dubayah, R.O.; Knox, R.G.; Clark, D.B.; Blair, J.B. (2002). Sensitivity of large-footprint lidar to canopy structure and biomass in a neotropical rainforest. *Remote Sens. Environ.*, *81*, 378–392, doi:10.1016/S0034-4257(02)00013-5.

Dubayah, R.O.; Sheldon, S.L.; Clark, D.B.; Hofton, M.A.; Blair, J.B.; Hurtt, G.C. (2010). Estimation of tropical forest height and biomass dynamics using lidar remote sensing at La Selva, Costa Rica. *J. Geophys. Res.*, *115*, doi:10.1029/2009JG000933.

d'Oliveira, M.V.N.; Reutebuch, S.E.; McGaughey, R.J.; Andersen, H.E. (2012). Estimating forest biomass and identifying low-intensity logging areas using airborne scanning lidar in Antimary State Forest, Acre State, Western Brazilian Amazon. *Remote Sens. Environ.*, *124*, 479–491, doi:10.1016/j.rse.2012.05.014.

Garcia, M.; Saatchi, S.; Ferraz, A.; Silva, C.A.; Ustin, S.; Koltunov, A.; Balzter, H. (2017). Impact of data model and point density on aboveground forest biomass estimation from airborne lidar. *Carbon Balance Manag.*, *12*, 4, doi:10.1186/s13021-017-0073-1.

Garcia, M.; Saatchi, S.; Casas, A.; Koltunov, A.; Ustin, S.; Ramirez, C.; Garcia-Gutierrez, J.; Balzter, H. (2017). Quantifying biomass consumption and carbon release from the California Rim fire by integrating airborne lidar and Landsat OLI data. *J. Geophys. Res. Biogeosci.*, *122*, 340–353.

Hansen, E.; Gobakken, T.; Næsset, E. (2015). Effects of pulse density on digital terrain models and canopy metrics using airborne laser scanning in a tropical rainforest. *Remote Sens. 7*, 8453–8468, doi:10.3390/rs70708453.

Hansen, M.C.; Potapov, P.V.; Moore, R.; Hancher, M.; Turubanova, S.A.; Tyukavina, A.; Thau, D.; Stehman, S.V.; Goetz, S.J.; Loveland, T.R. (2013). High-resolution global maps of 21st-century forest cover change. *Science*, *342*, 850–853, doi:10.1126/science.1244693.

Hudak, A.T.; Crookston, N.L.; Evans, J.S.; Falkowski, M.J.; Smith, A.M.S.; Gessler, P.E. (2006). Regression modeling and mapping of coniferous forest basal area and tree density from discrete-return lidar and multispectral satellite data. *Can. J. Remote Sens.*, *32*, 126–138, doi:10.5589/m06-007.

Hudak, A.T.; Strand, E.K.; Vierling, L.A.; Byrne, J.C.; Eitel, J.U.H.; Martinuzzi, S.; Falkowski, M.J. (2012). Quantifying aboveground forest carbon pools and fluxes from repeat lidar surveys. *Remote Sens. Environ.*, *123*, 25–40, doi:10.1016/j.rse.2012.02.023.

Hummel, S.; Hudak, A.T.; Uebler, E.H.; Falkowski, M.J.; Megown, K.A. (2015). A comparison of accuracy and cost of lidar versus stand exam data for landscape management on the Malheur national forest. *J. For.*, *109*, 267–273.

Isenburg, M. (2016). LAStools—Efficient Tools for Lidar Processing. Available online: http://www.cs.unc.edu/~isenburg/lastools/ (accessed on 3 October 2016).

Jakubowski, M.K.; Guo, Q.H.; Kelly, M. (2013). Tradeoffs between lidar pulse density and forest measurement accuracy. *Remote Sens. Environ.*, *130*, 245–253, doi:10.1016/j.rse.2012.11.024 10.1016/j.rse.2012.11.024.

Le Quéré, C.; Moriarty, R.; Andrew, R.M.; Canadell, J.G.; Sitch, S.; Korsbakken, J.I.; Friedlingstein, P.; Peters, G.P.; Andres, R.J.; Boden, T.A. (2015). Global Carbon Budget. *Earth Syst. Sci. Data*, *7*, 349–396, doi:10.5194/essd-7-349-2015.

Leitold, V.; Keller, M.; Morton, D.C.; Cook, B.D.; Shimabukuro, Y.E. (2015). Airborne lidar-based estimates of tropical forest structure in complex terrain: Opportunities and trade-offs for REDD+. *Carbon Balance Manag.*, *10*, 2-12, doi:10.1186/s13021-015-0013-x.

Lovell, J.L.; Jupp, D.L.B.; Newnham, G.J.; Coops, N.C.; Culvenor, D.S. (2005). Simulation study for finding optimal lidar acquisition parameters for forest height retrieval. *For. Ecol. Manag., 214*, 398–412, doi:10.1016/j.foreco.2004.07.077.

Longo, M.; Keller, M.; dos-Santos, M.N.; Leitold, V.; Pinagé, E.R.; Baccini, A.; Saatchi, S.; Nogueira, E.M.; Batistella, M.; Morton, D.C. (2016). Aboveground biomass variability across intact and degradedforests in the Brazilian Amazon. *Glob. Biogeochem. Cycles, 30*, 1639–1660, doi:10.1002/2016GB005465.

Magnussen, S.; Næsset, E.; Gobakken, T. (2010). Remote sensing of environment reliability of lidar derived predictors of forest inventory attributes: A case study with Norway spruce. *Remote Sens. Environ., 114*, 700–712, doi:10.1016/j.rse.2009.11.007.

Meyer, V.; Saatchi, S.S.; Chave, J.; Dalling, J.W.; Bohlman, S.; Fricker, G.A.; Robinson, C.; Neumann, M.; Hubbell, S. (2013). Detecting tropical forest biomass dynamics from repeated airborne lidar measurements. *Biogeosciences*, *10*, 5421–5438, doi:10.5194/bg-10- 5421-2013.

Magnusson, M.; Fransson, J.E.S.; Holmgren, J. (2007). Effects on estimation accuracy of forest variables using different pulse density. *For. Sci., 53*, 619–626.

Matricardi, E.A.T.; Skole, D.; Pedlowski, M.A.; Fernandes, L.C. (2010). Assessment of tropical forest degradation by selective logging and fire using Landsat imagery. *Remote Sens. Environ*., *114*, 1117–1129.

McGauchey, R.J. (2015). FUSION/LDV: Software for lidar Data Analysis and Visualization. Forest Service Pacific Northwest Research Station USDA, Seattle. Available online: http://forsys.cfr.washington.edu/fusion/FUSION_manual.pdf (accessed on 15 October 2016).

McRoberts, D.E.; Bollandsås, O.M.; Næsset, E. (2014). Modeling and estimating change. In *Forestry Applications of Airborne Laser Scanning*; Concepts and Case Studies; Maltamo, M., Naesset, E., Vauhkonen, J., Eds.; Springer: Dordrecht, The Netherlands, 293–313.

McRoberts, D. (2006). A model-based approach to estimating forest area. *Remote Sens. Environ., 103*, 56–66.

Næsset, E.; Bjerknes, K.O. (2001). Estimating tree heights and number of stems in young forest stands using airborne laser scanner data. *Remote Sens. Environ., 78*, 328–340, doi:10.1016/S0034-4257(01)00228-0.

Næsset, E. Predicting forest stand characteristics with airborne scanning laser using a practical two-stage procedure and field data. (2002). *Remote Sens. Environ., 80*, 88–99, doi:10.1016/S0034-4257(01)00290-5.

Naesset, E.; Gobakken, T. (2008). Estimation of above- and below-ground biomass across regions of the boreal forest zone using airborne laser. *Remote Sens. Environ.*, *112*, 3079–3090, doi:10.1016/j.rse.2008.03.004.

Nepstad, D.; McGrath, D.; Stickler, C.; Alencar, A.; Azevedo, A.; Swette, B.; Bezerra, T.; DiGiano, M.; Shimada, J.; Motta, R.S. (2014). Slowing Amazon deforestation through public policy and interventions in beef and soy supply chains. *Science*, *344*, 1118–1123, doi:10.1126/science.1248525.

Ota, T.; Kajisa, T.; Mizoue, N.; Yoshida, S.; Takao, G.; Hirata, Y.; Furuya, N.; Sano, T.; Ponce-Hernandez, R.; Ahmed, O.S. (2015). Estimating aboveground carbon using airborne lidar in Cambodian tropical seasonal forests for REDD+ implementation. *J. For. Res.*, *20*, 484–492, doi:10.1007/s10310-015-0504-3.

Radambrasiz (1983). *Projeto RADAMBRASIL: 1973–1983—Levantamento de Recursos Naturais*; Ministério das Minas e Energia, Departamento Nacional de Produção Mineral: Rio de Janeiro, Brazil; Volume 1–23.

R Core Team. R: A Language and Environment for Statistical Computing (2015). R Foundation for Statistical Computing, Vienna, Austria. Available online: https://www.r-project.org/ (accessed on 15 May 2016).

Silva, C.A.; Klauberg, C.; Hudak, A.T.; Vierling, L.A.; Liesenberg, V.; Carvalho, S.P.C.; Rodriguez, L.C.E. (2016). Principal component approach for predicting the stem volume in Eucalyptus plantations in Brazil using airborne lidar data. *Forestry*, *89*, 1–12, doi:10.1093/forestry/cpw016.

Silva, C.A.; Klauberg, C.; Hudak, A.T.; Vierling, L.A.; Jaafar, W.S.W.M.; Mohan, M.; Garcia, M.; Ferraz, A.; Cardil, A.; Saatchi, S. (2017). Predicting Stem Total and Assortment Volumes in an Industrial *Pinus taeda* L. Forest Plantation Using Airborne Laser Scanning Data and Random Forest. *Forests*, *8*, 254.

Silva, C.A.; Hudak, A.; Vierling, L.A.; Loudermilk, L.; O'brien, J.J.; Hiers, J.; Jack, J.; Gonzalez-Benecke, C.A.; Lee, H.; alkowskie, M.J. (2016). Imputation of individual longleaf pine (Mill.) Tree attributes from field and lidar Data. *Can. J. Remote Sens.*, 42, 554–573.

Silva, C.A.; Klauberg, C.; de Pádua, S.; Hudak, A.T.; Rodriguez, L.C. (2014). Mapping aboveground carbon stocks using lidar data in Eucalyptus spp. plantations in the state of São Paulo, Brazil. *Sci. For.*, *42*, 591–604.

Silva, C.A.; Hudak, A.T.; Klauberg, C.; Vierling, L.A.; Gonzalez-Benecke, C.; de Padua Chaves Carvalho, S.; Rodriguez, L.C.E.; Cardil, A. (2017b). Combined effect of pulse density and grid cell size on predicting and mapping aboveground carbon in fast-

growing Eucalyptus forest plantation using airborne lidar data. *Carbon Balance Manag.*, *12*, 13.

Singh, K.K.; Chen, G.; McCarter, J.B.; Meentemeyer, R.K. (2015). Effects of lidar point density and landscape context on estimates of urban forest biomass. *ISPRS J. Photogramm. Remote Sens.*, *101*, 310–322, doi:10.1016/j.isprsjprs.2014.12.021.

Shenkin, A.; Bolker, B.; Peña-Claros, M.; Licona, J.C.; Putz, F.E. (2015). Fates of treesdamaged by logging in Amazonian Bolivia. *For. Ecol. Manag.*, *357*, 50–59, doi:10.1016/j.foreco.2015.08.009.

Strunk, J.; Temesgen, H.; Andersen, H.E.; Flewelling, J.P.; Madsen, L. (2012). Effects of lidar pulse density and sample size on a model-assisted approach to estimate forest inventory variables. *Can. J. Remote Sens.*, *38*, 644–654, doi:10.5589/m12-052.

Tesfamichael, S.G.; Ahmed, F.B.; van Aardt, J.A.N. (2010). Investigating the impact of discrete-return lidar point density on estimations of mean and dominant plot-level tree height in Eucalyptus grandis plantations. *Int. J. Remote Sens.*, *31*, 2925–2940, doi:10.1080/01431160903144086.

Vidal, E.; West, T.A.P.; Putz, F.E. (2016). Recovery of biomass and merchantable timber volumes twenty years after conventional and reduced-impact logging in amazonian Brazil. *For. Ecol. Manag*., *376*, 1–8, doi:10.1016/j.foreco.2016.06.003.

Watt, M.S.; Meredith, A.; Watt, P.; Gunn, A. (2014). The influence of lidar pulse density on the precision of inventory metrics in young unthinned Douglas-fir stands during initial and subsequent lidar acquisitions. *N. Z. J. For. Sci.*, *44*, 2–9, doi:10.1186/s40490-014-0018-3.

Wilkes, P.; Jones, S.D.; Suarez, L.; Haywood, A.; Mellor, A.; Woodgate, W.; Soto-berelov, M.; Skidmore, A.K. (2015). Understanding the effects of ALS pulse density for metric retrieval across diverse forest types. Photogramm. *Eng. Remote Sens.*, *81*, 625–635.

Weisbin, C.R.; Lincoln, W.; Saatchi, S. (2014). A systems engineering approach to estimating uncertainty in above-ground biomass (AGB) derived from remote-sensing data. *Syst. Eng.*, *17*, 361–373.

Table 3.1. Summary of the AGB stocks at the sample plots.

Field Attributes	min	max	mean	sd
dbh (cm)	10.00	186.00	32.70	20.16
AGB (kg·tree^{-1})	22.46	73700	1804	3684
AGB (Mg·ha^{-1})	65.34	525.79	238.11	86.48

Table 3.2. Details of lidar data acquisitions.

Data Attributes	2012	2014
Lidar system	ALTM 3100	ALTM300
Flight Altitude (m)	850	850
Acquisition Date	27–29 July 2012	26–27 December 2014
Scan Angle (°)	11	12
Scanning Frequency (Kz; Hz)	59.8	83.0
Pulse Density (pulses·m^{-2})	13.8	37.5
Datum	Sirgas 2000	Sirgas 2000

Table 3.3. Mean and standard deviation of the parameters a_{2014} and b_{2014} for the AGB models in 2014. DS1: DTM Scenario 1; DS2: DTM Scenario 2.

DTM Scenario	Model Parameter Estimates	Lidar Pulse Density (pulse·m^{-2})									
		0.2	**0.4**	**0.6**	**0.8**	**2**	**4**	**6**	**8**	**10**	**12**
DS1	a_{2014}	0.50 ± 0.35	0.22 ± 0.05	0.20 ± 0.03	0.18 ± 0.02	0.16 ± 0.01	0.16 ± 0.01	0.16 ± 0.00	0.16 ± 0.00	0.15 ± 0.00	0.15 ± 0.00
	b_{2014}	2.08 ± 0.19	2.29 ± 0.07	2.33 ± 0.05	2.36 ± 0.03	2.39 ± 0.02	2.40 ± 0.01	2.41 ± 0.01	2.41 ± 0.01	2.41 ± 0.01	2.41 ± 0.01
DS2	a_{2014}	0.19 ± 0.03	0.17 ± 0.02	0.17 ± 0.01	0.16 ± 0.01	0.16 ± 0.01	0.16 ± 0.00	0.16 ± 0.00	0.15 ± 0.00	0.15 ± 0.00	0.15 ± 0.00
	b_{2014}	2.35 ± 0.05	2.38 ± 0.04	2.39 ± 0.02	2.39 ± 0.02	2.41 ± 0.01	2.41 ± 0.01	2.41 ± 0.01	2.41 ± 0.01	2.41 ± 0.01	2.41 ± 0.01

Table 3.4. Mean and standard deviation (Sd) of the parameters a and b for the AGB models in 2014. DS1: DTM Scenario 1; DS2: DTM Scenario 2. Std Error is the estimated standard error derived from the uncertainty analysis.

Pulse Density (pulse ·m^{-2})	AGB 2012 (Mg·ha^{-1})		AGB 2014 (Mg·ha^{-1})		ΔAGB (Mg·ha^{-1})	
	Mean + Sd	Std Error	Mean + Sd	Std Error	Mean + Sd	Std Error
			DTM Scenario 1 (DS1)			
0.2	262.54 ± 78.93	1.12	278.42 ± 84.7	1.19	15.88 ± 33.09	2.64
0.4	266.56 ± 87.63	1.23	284.49 ± 94.59	1.31	17.93 ± 36.04	2.80
0.6	267.46 ± 89.5	1.25	286.00 ± 96.9	1.33	18.54 ± 36.61	2.80
0.8	268.18 ± 90.7	1.27	287.08 ± 98.39	1.35	18.9 ± 37.03	2.82
2	268.88 ± 92.26	1.29	288.41 ± 100.53	1.37	19.53 ± 37.71	2.84
4	268.96 ± 92.61	1.29	288.66 ± 100.98	1.37	19.69 ± 37.86	2.84
6	269.03 ± 92.79	1.29	288.74 ± 101.17	1.38	19.7 ± 37.92	2.85
8	269.11 ± 92.85	1.29	288.70 ± 101.16	1.38	19.59 ± 37.96	2.88
10	269.26 ± 93.01	1.29	288.70 ± 101.21	1.38	19.44 ± 38.08	2.93
12	269.45 ± 93.17	1.30	288.73 ± 101.28	1.38	19.28 ± 38.22	2.97
			DTM Scenario 2 (DS2)			
0.2	268.09 ± 90.32	1.26	291.3 ± 99.16	1.35	22.58 ± 37.22	2.41
0.4	268.43 ± 91.41	1.28	291.90 ± 100.42	1.37	22.84 ± 37.61	2.44
0.6	268.54 ± 91.8	1.28	292.14 ± 100.91	1.37	22.97 ± 37.8	2.44
0.8	268.87 ± 92.25	1.29	292.59 ± 101.43	1.38	23.08 ± 37.98	2.45
2	269.07 ± 92.77	1.29	292.92 ± 102.08	1.38	23.21 ± 38.22	2.47
4	269.05 ± 92.81	1.29	292.95 ± 102.13	1.38	23.25 ± 38.22	2.47
6	269.12 ± 92.92	1.29	293.02 ± 102.25	1.38	23.26 ± 38.25	2.48
8	269.18 ± 92.96	1.29	292.98 ± 102.21	1.38	23.16 ± 38.29	2.49
10	269.31 ± 93.1	1.30	292.98 ± 102.25	1.38	23.04 ± 38.4	2.52
12	269.48 ± 93.23	1.30	292.99 ± 102.29	1.38	22.89 ± 38.52	2.56

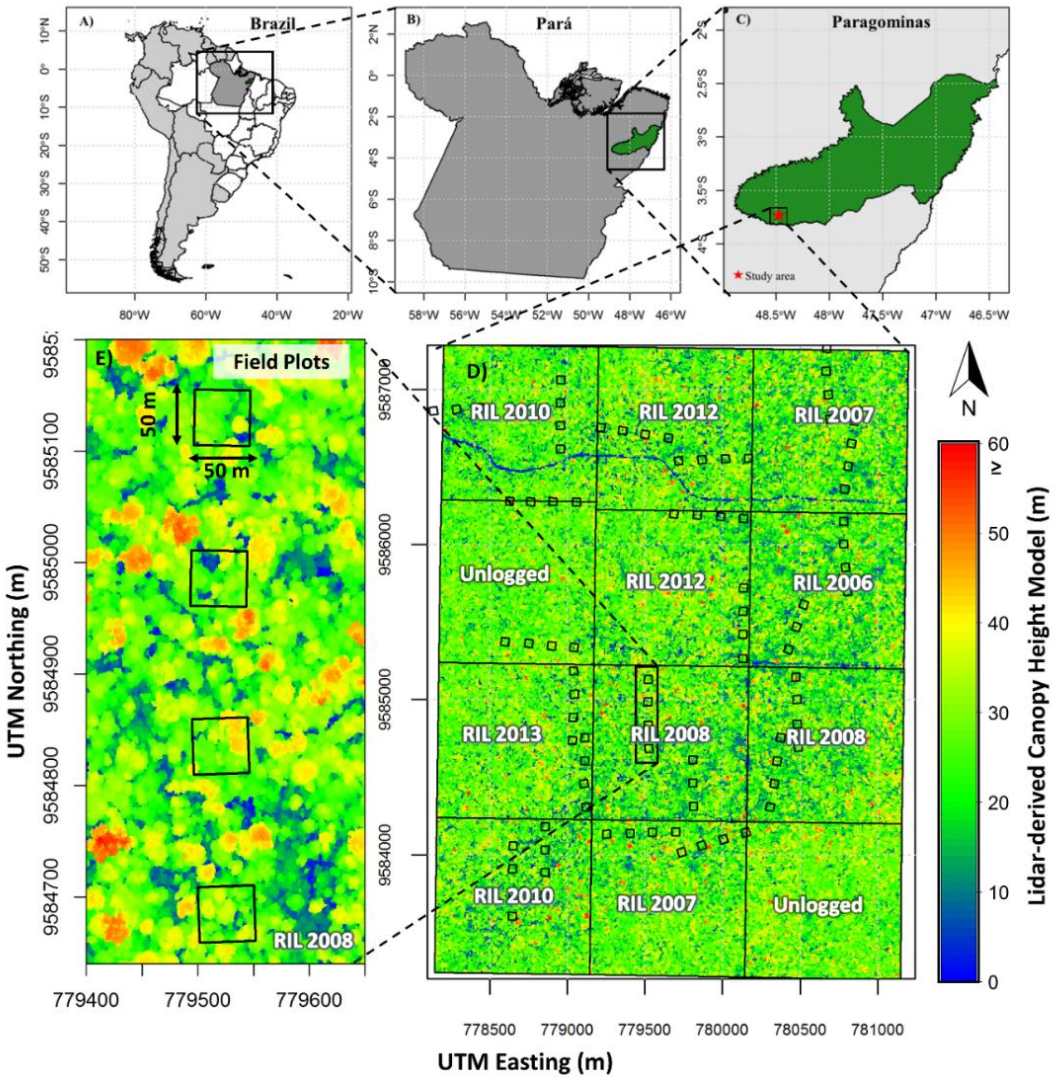

Figure 3.1. Location of the study area. (A) South America and Brazil; (B) States of Pará and Paragominas city; (C) Paragominas city; (D) Airborne lidar coverage; (E) Field plots on the lidar-derived CHM. Reduced-impact logging (RIL).

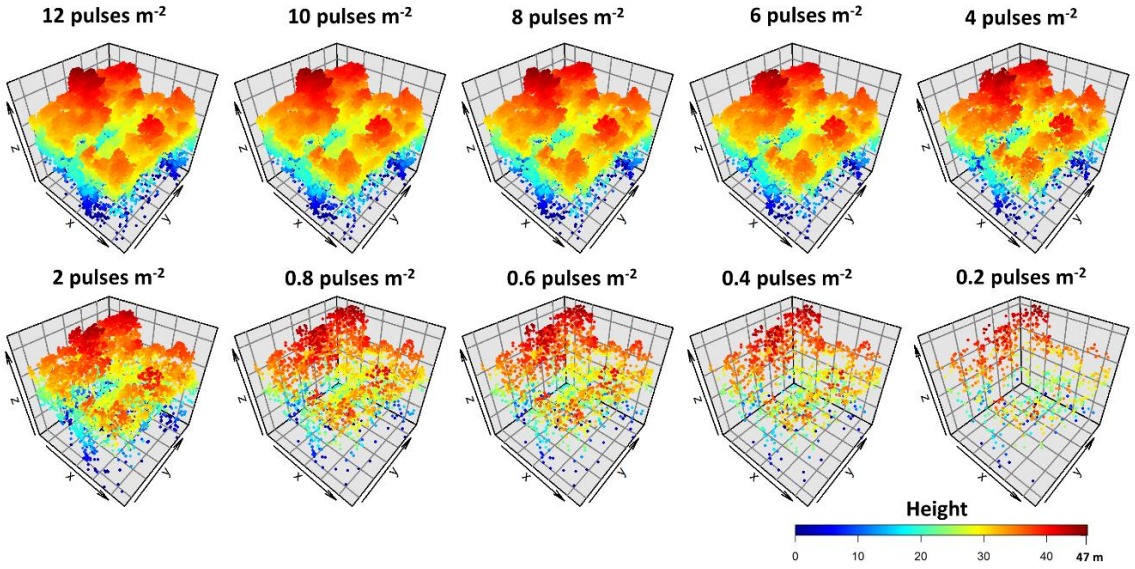

Figure 3.2. A 3D illustration of airborne lidar pulse density reduction at the plot level (0.25 ha) in 2014.

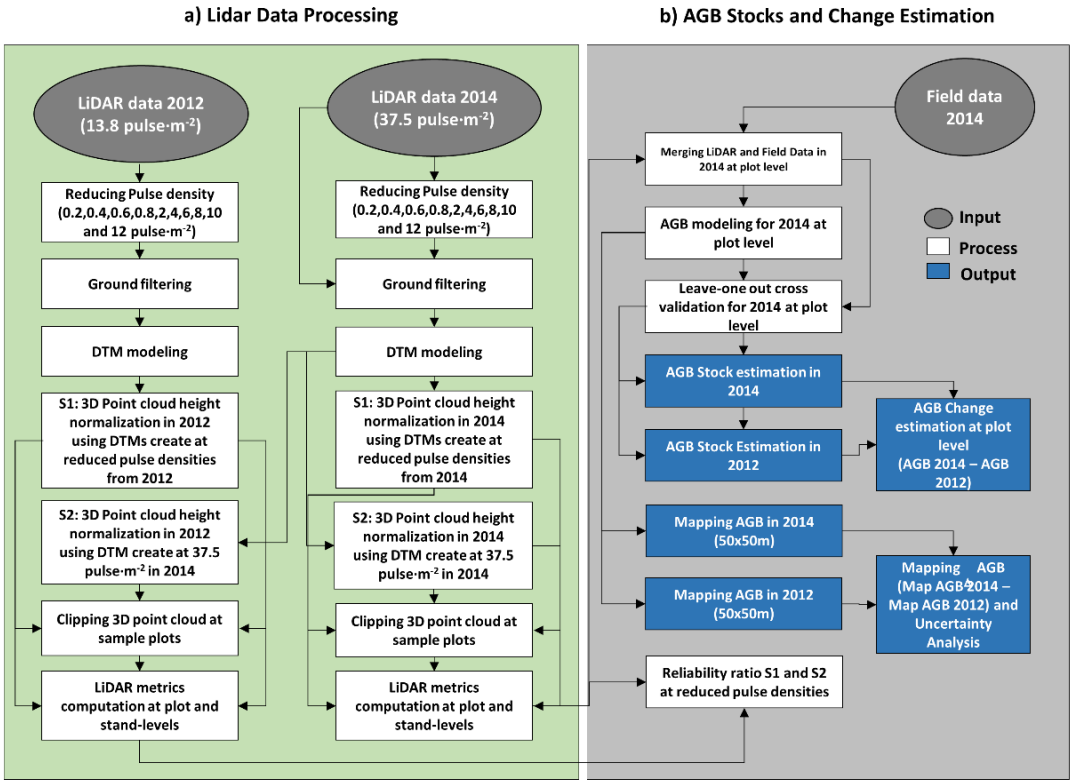

Figure 3.3. Flowchart of the lidar data processing for AGB stocks and AGB change estimation in tropical forest. The green panel to the left shows the lidar data processing (a) and the gray panel to the right shows the AGB stocks and change estimation steps (b).

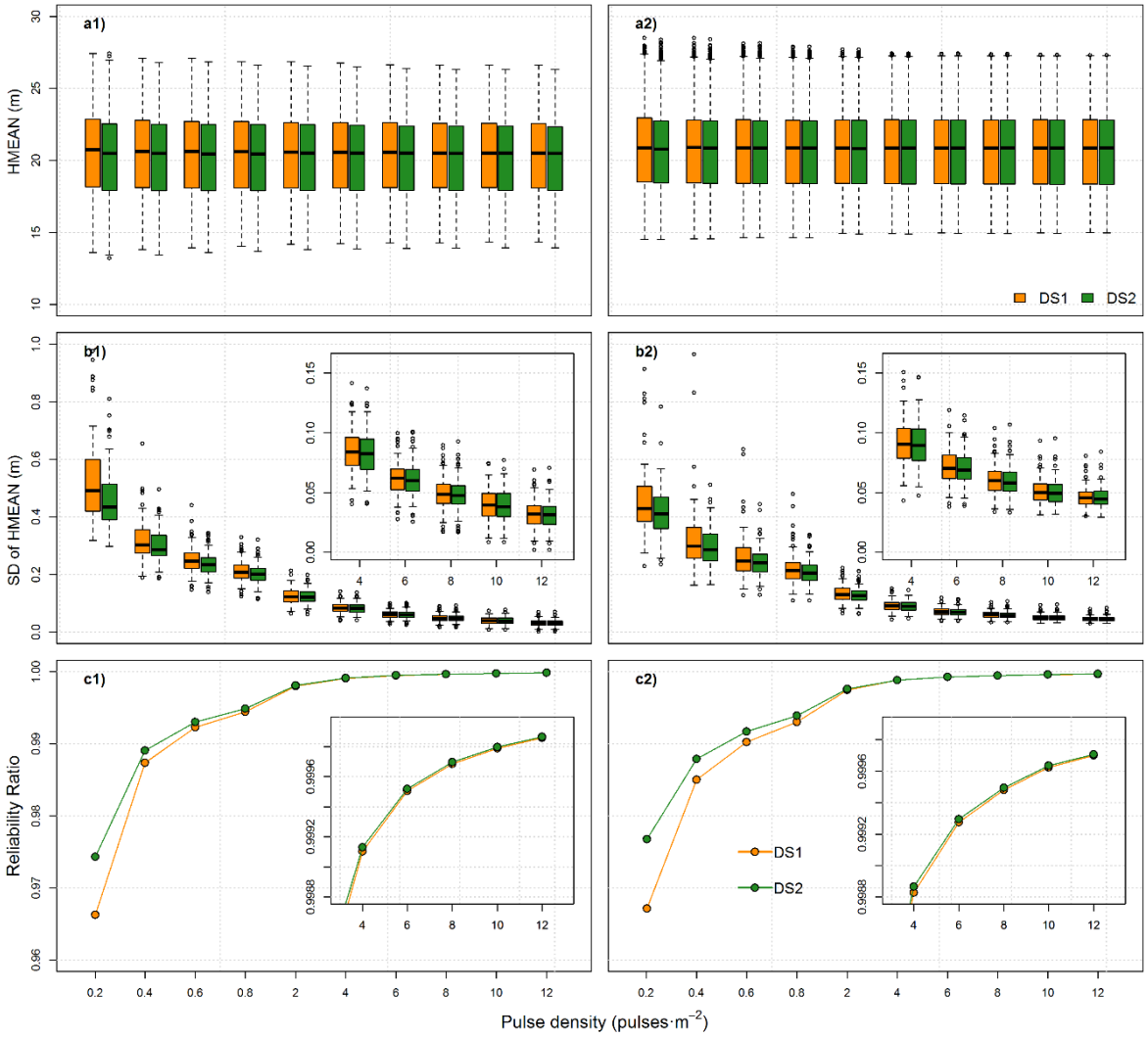

Figure 3.4. Lidar-derived HMEAN (m) (a1-2); Standard deviation of HMEAN (m) for the sample plots (30 repetitions) (b1-2); Reliability Ratio for HMEAN (c1-2); 2012 (a1–c1) and 2014 (a2–c2); (n = 84). DS1 (orange): DTM scenario 1; DS2 (green): DTM scenario 2.

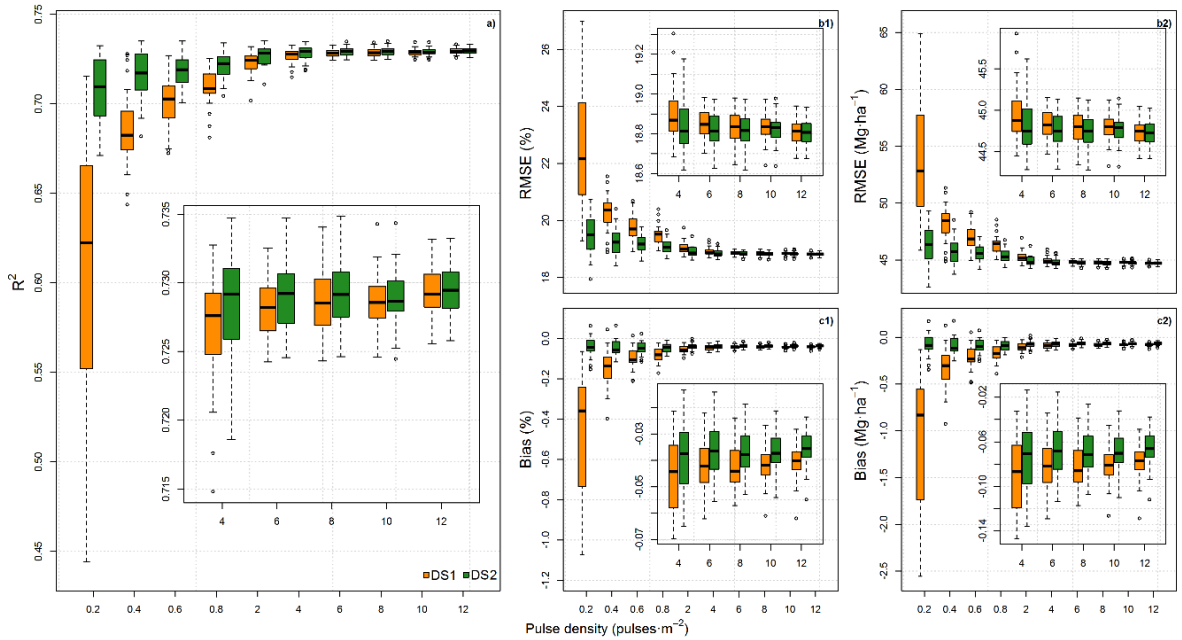

Figure 3.5. Boxplot of R2 (a), relative (b1–c1) and absolute (b2–c2) RMSE and bias for the AGB leave-one-out cross validation – LOOCV models. DS1 (orange): DTM Scenario 1; DS2 (green): DTM Scenario 2.

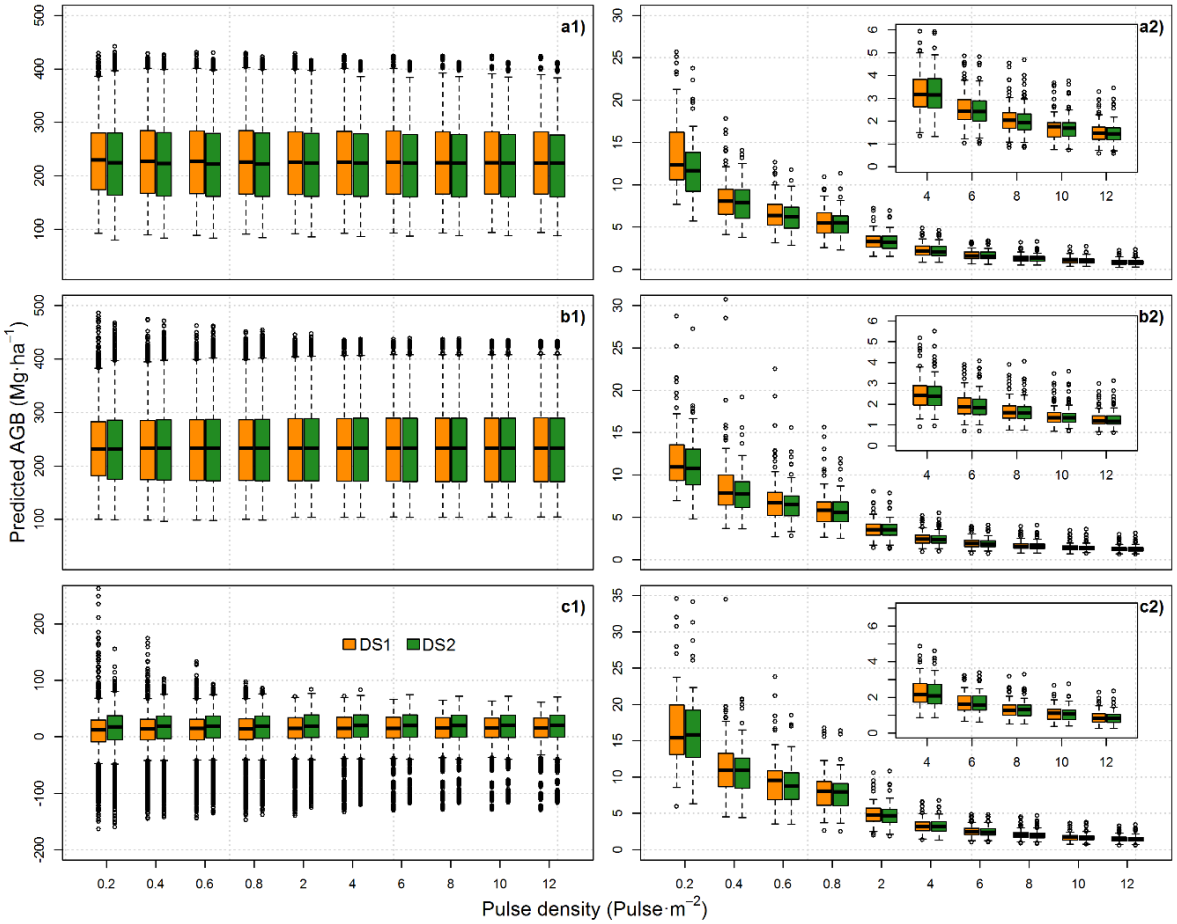

Figure 3.6. Boxplot of the AGB estimates for 2012 and 2014 (a1,b1), and AGB change (c1). Standard deviation of AGB stock in 2012 (a2), 2014 (b2) and AGB change (c2) (30 repetitions) (n = 84).

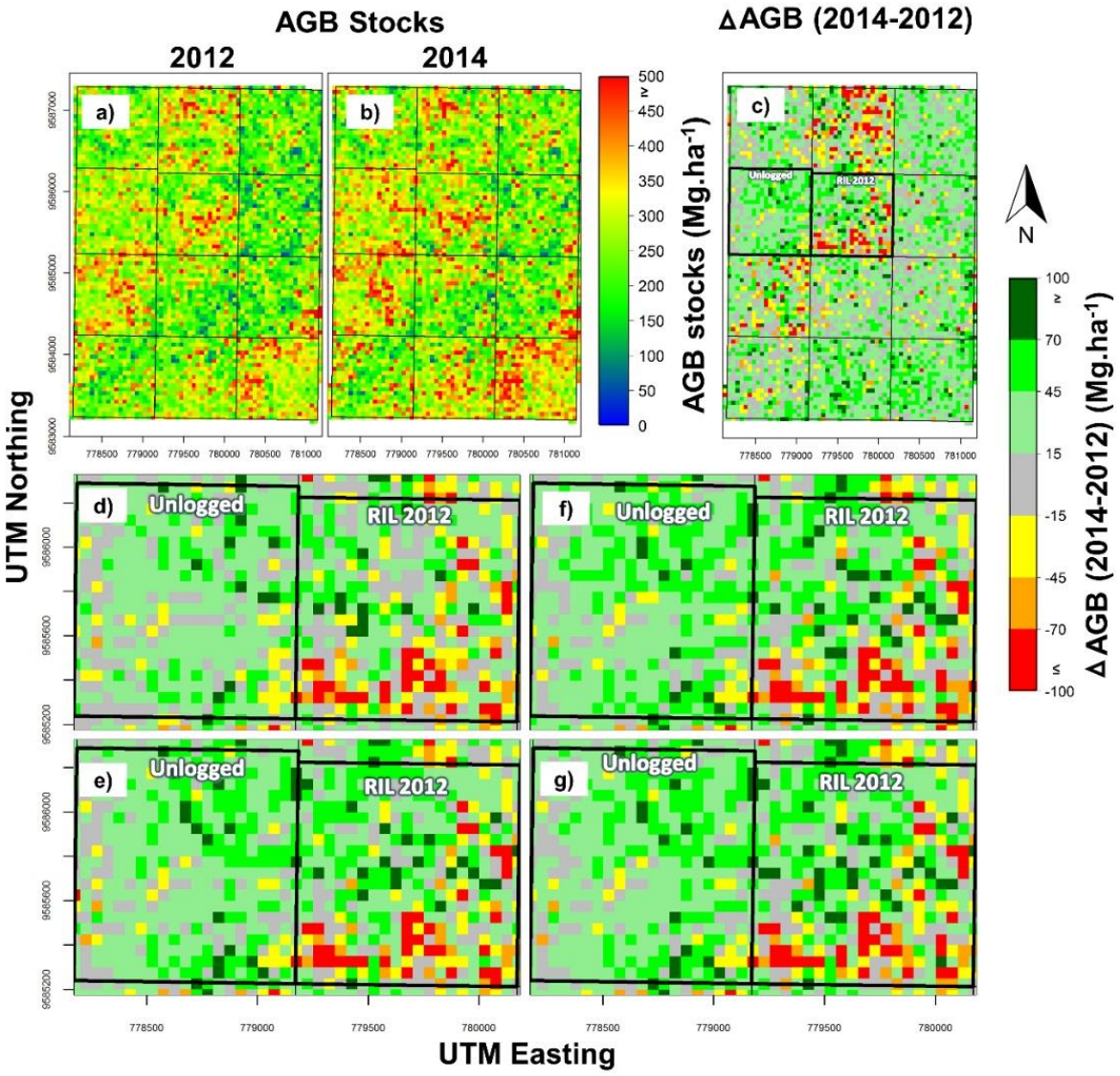

Figure 3.7. Map of AGB stock in 2012 (a), 2014 (b) and AGB change (c) at 12 pulse·m^{-2} in DS2. Zoom in the AGB change maps derived at 0.2 and 12 pulse·m^{-2} in DS1 (d,e) and DS2 (f,g) in an unlogged and logged unit. The maps were calculated as the mean of the 30 replicates.

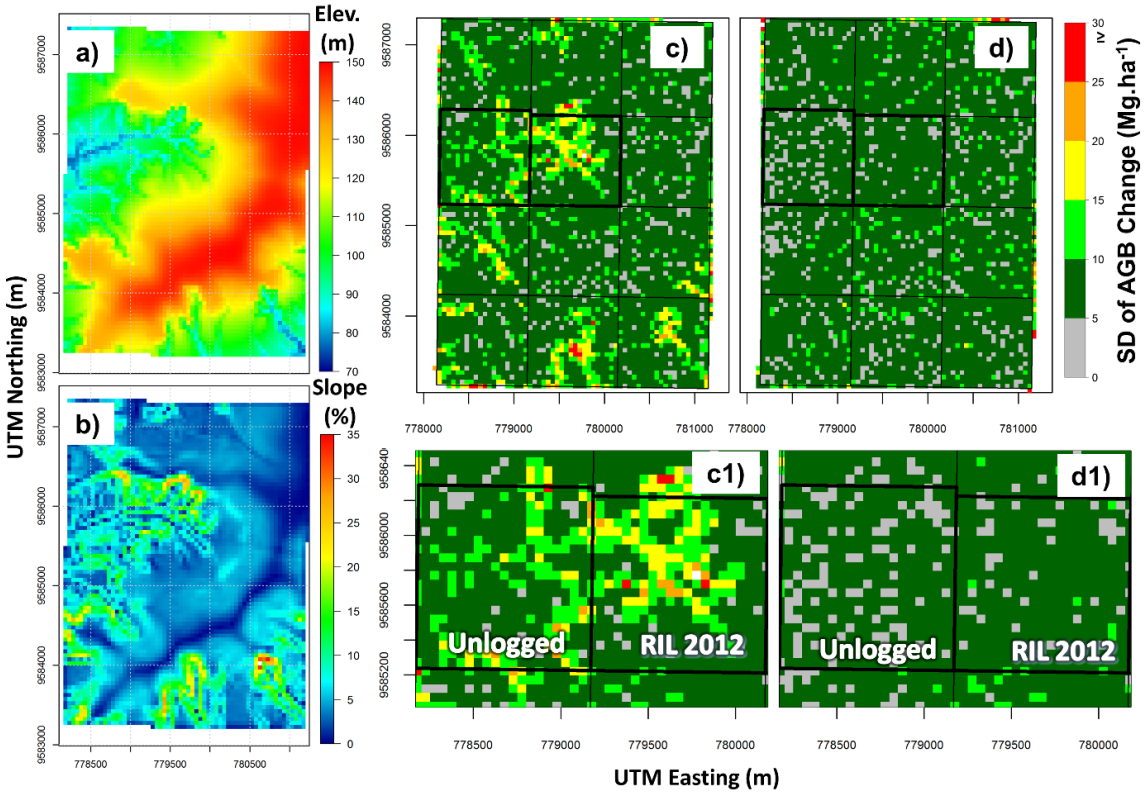

Figure 3.8. Digital terrain model (a) and Slope (%) (b) maps of the study area at 12 pulses·m^{-2} in 2012; Standard deviation of AGB change at 0.2 pulses·m^{-2} for DS1 (c–c1) and DS2 (d–d1).

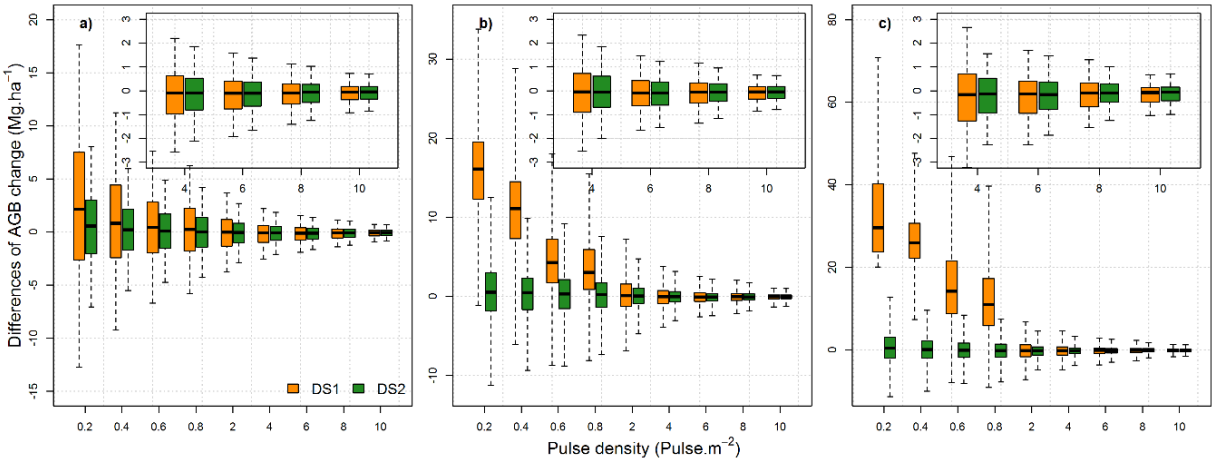

Figure 3.9. Boxplot of the differences in predicted AGB change at stand level of 12 m^{-2} degraded to 0.2, 0.4, 0.6, 0.8, 2, 4, 6, 8 and 10 pulses·m^{-2} in areas with slopes ranging from 0 to 12% (a), 12–24% (b) and 24–36% (c), under DS1 (orange) and DS2 (dark green).

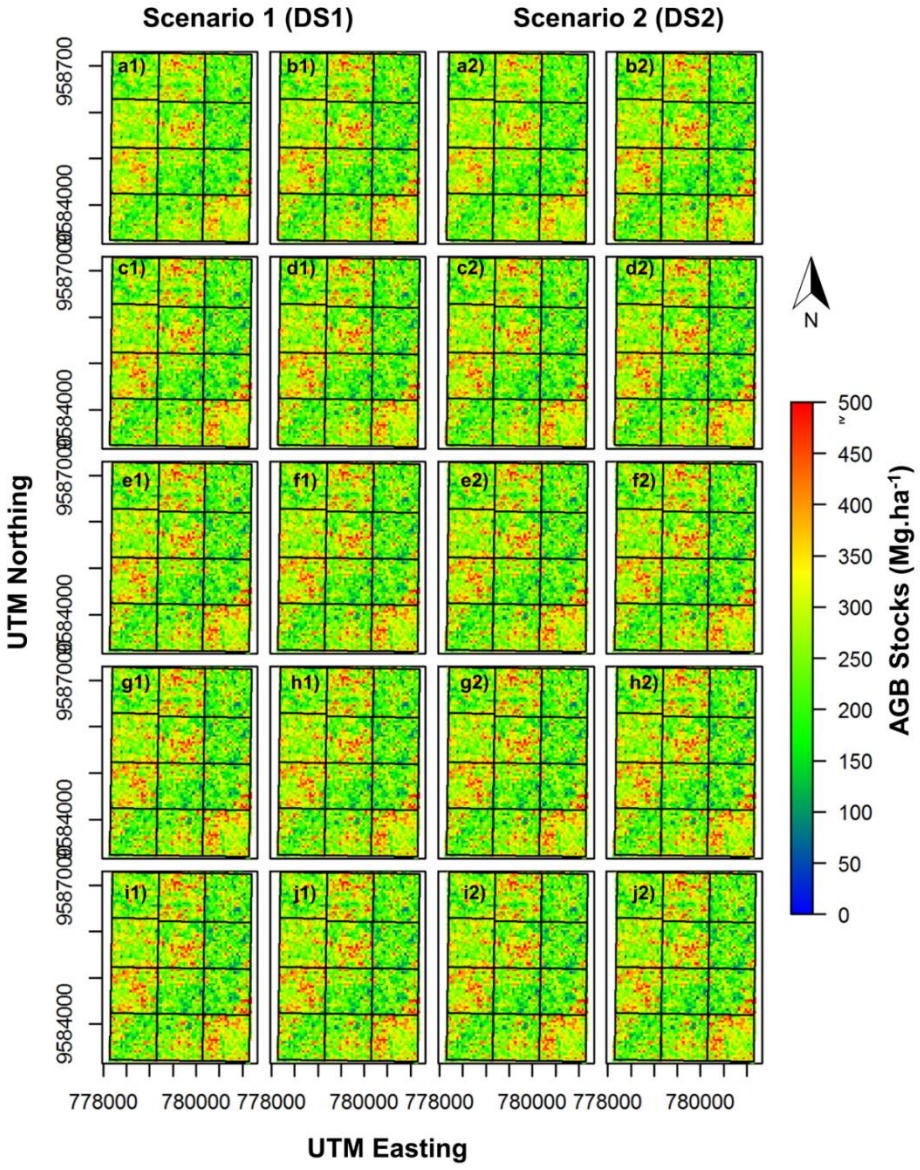

Figure S3.1. Mean of the 30 replicates AGB stocks in 2012 at pulse density ranging from 0.2 to 12 pulse·m^{-2} in DS1 (a1–j1) and DS2 (a2–j2).

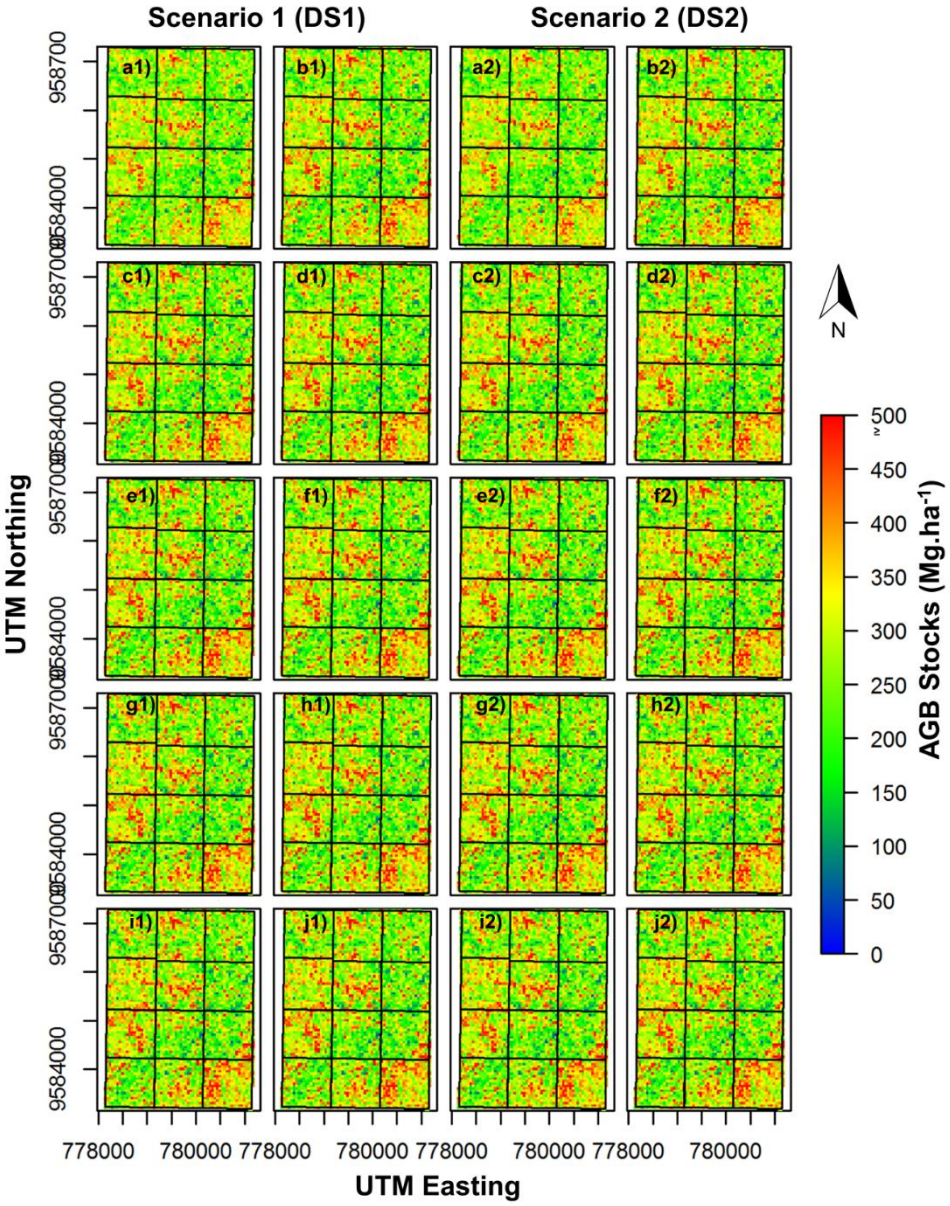

Figure S3.2. Mean of the 30 replicates AGB stocks in 2014 at pulse density ranging from 0.2 to 12 pulse·m^{-2} in DS1 (a1–j1) and DS2 (a2–j2).

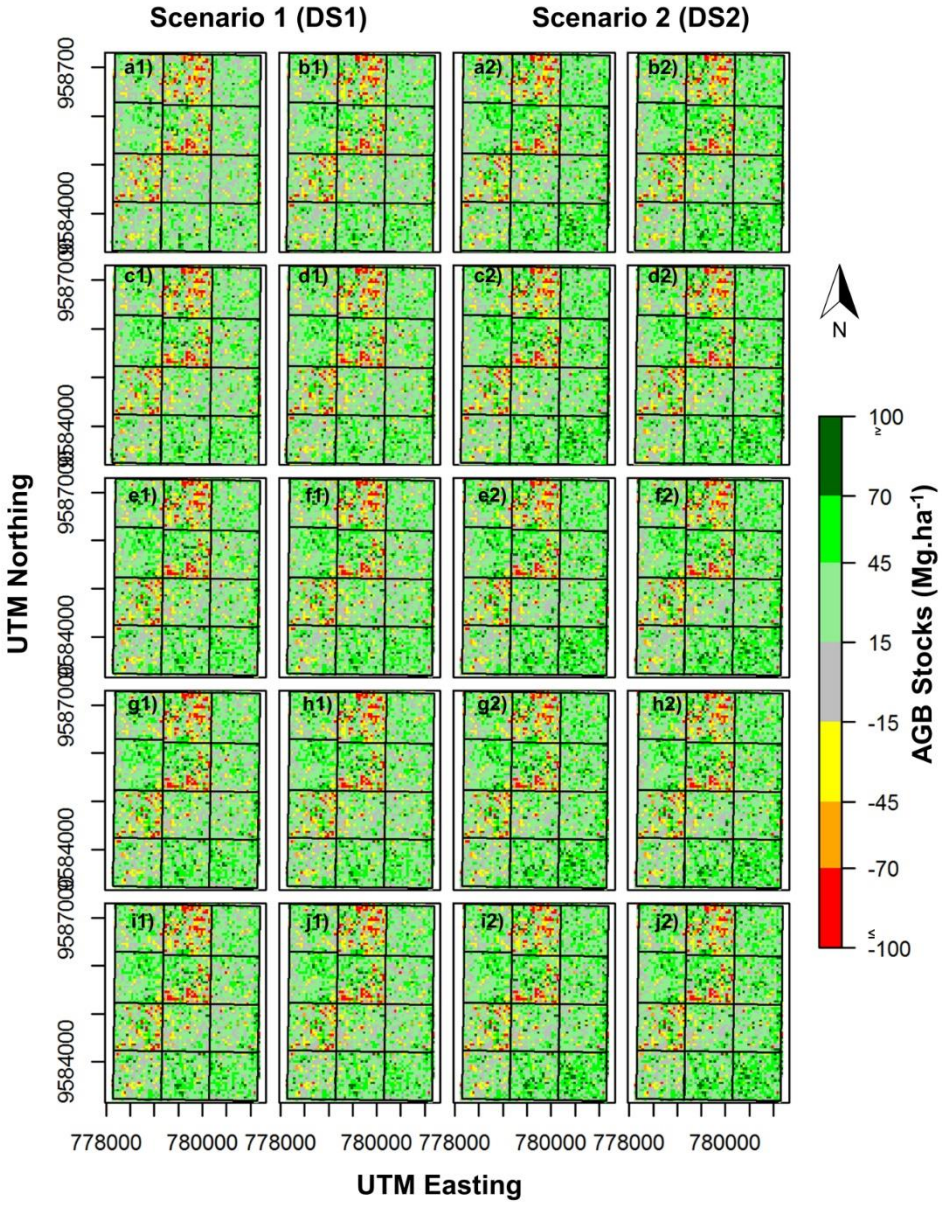

Figure S3.3. Mean of the 30 replicates of AGB change at pulse density ranging from 0.2 to 12 pulse·m^{-2} in DS1 (a1–j1) and DS2 (a2–j2).

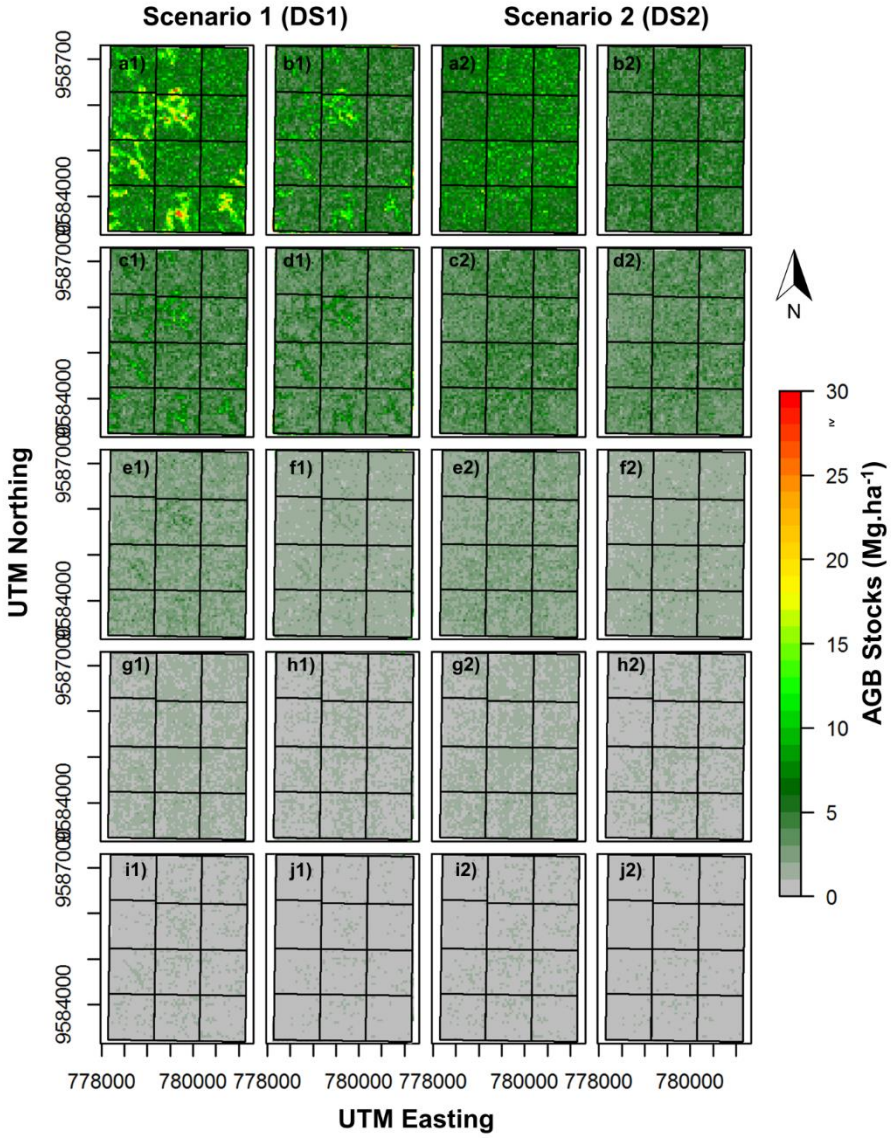

Figure S3.4. Standard deviation of the 30 replicates of AGB change at pulse density ranging from 0.2 to 12 pulse·m^{-2} in DS1 (a1–j1) and DS2 (a2–j2).

Chapter 4. Comparison of Small- and Large-Footprint Lidar Characterization of Tropical Forest Aboveground Structure and Biomass: A Case Study from Central Gabon

Silva, C.A.; Saatchi, S.; Garcia, M.; Labrière, N.; Klauberg, C.; Ferraz, A.; Meyer, V.; Jeffery, K. J.; Abernethy, K.; White, L.; Zhao, K.; Lewis, S.; Hudak, A. T. IEEE Journal of Selected Topics in Applied Earth Observations and Remote Sensing, under consideration.

Abstract

The NASA Global Ecosystem Dynamic Investigation (GEDI) has been designed to capture variation in forest structure using large-footprint lidar waveform sampled as it orbits the Earth while aboard the International Space Station. In this paper, we compared the retrieval of ground elevation, vegetation height and biomass from airborne small-footprint (SF) and large-footprint (LF) lidar sensors. The study focuses on Lope National Park in Central Gabon, in an area that encompasses a gradient of successional stages of forest development with different height, canopy density and topography. Airborne and ground data were collected during the AfriSAR campaign in Gabon. The comparison of the two sensors shows that LF lidar waveforms are equivalent to simulated waveforms from SF lidar for retrieving ground elevation (RMSE=0.5 m, bias=0.29 m) and maximum forest height (RMSE=2.99 m; bias=0.24 m). Comparison of gridded LF lidar height with ground plots showed that an unbiased estimate of aboveground biomass at 1-ha can be achieved with sufficient number of large footprints (> 3). Our results confirm the capability of LF lidar, as planned for the GEDI mission, to measure the complex structure of humid tropical forests and to provide estimates of forest aboveground biomass comparable to SF.

Keywords: Lidar, LVIS, GEDI, Gabon, Tropical Forest, AfriSAR

4.1 Introduction

The NASA Global Ecosystem Dynamics Investigation Lidar (GEDI) space mission is planned to be onboard the International Space Station (ISS) for two years beginning late 2018. The sensor will collect 25m diameter footprint full-waveform lidar data to help characterize vegetation structure and aboveground biomass globally, and report on aboveground biomass dynamics across landscapes. Lidar is an active remote sensing technique that is well-suited to providing high resolution, three-dimensional information on vertical and horizontal forest structures and underlying topography (Maltamo et al., 2014). Over the past few decades, lidar has been used to accurately retrieve ground and aboveground forest attributes, such as aboveground biomass (AGB), in temperate (e.g., García et al., 2010; Hudak et al., 2012), boreal (e.g. Næsset 1997; Næsset 2002) and tropical forests (e.g., Drake et al., 2002a; Clark et al., 2004; Saatchi et al., 2011). Lidar systems for forestry applications are distinguished based on platform type (e.g., terrestrial, airborne or spaceborne), signal recording (discrete return or full-waveform), footprint size (e.g. small i.e., < 1m or large i.e., 10-25m in diameter) and sample scanning pattern (profiling or scanning) (Dubayah et al., 2000; Lu et al., 2012). The most common lidar systems used in forestry applications have been small-footprint (SF) discrete return lidar and large-footprint (LF) full-waveform (FW) lidar. SF lidar sensors record discrete heights at peak return of light and are typically flown on airborne platforms or operated on the ground, while LF FW lidar sensors record a continuous height distribution of surfaces illuminated by the laser pulse and are found mainly on spaceborne platforms, such as the GLAS (Geoscience Laser Altimeter System) sensor (Lefsky et al., 2012). LVIS (Land, Vegetation, and Ice Sensor) is a LF lidar sensor on airborne platforms that provides coverage of large areas and can be used to simulate the characteristics of spaceborne observations such as GEDI (Qi et al., 2016). In both LF and SF systems, canopy height metrics (i.e., maximum height, height percentiles and canopy cover) can be derived from the recorded returned signals and may be used to retrieve aboveground forest structural properties. For example, Lefsky et al., (2010) used the GLAS data to produce a global map of forest height and Saatchi et al., (2011) converted the GLAS height metrics to aboveground biomass to produce a benchmark map of carbon

stocks of tropical forests across three continents. Drake et al., (2002a) and Drake et al., (2002b) used metrics derived from LVIS to estimate a variety of forest attributes, including AGB, over a tropical forest area at the La Selva Biological Station, Costa Rica. Asner and Mascaro (2014), using SF lidar, developed a series of aboveground carbon density models by calibrating the plot estimates to simple lidar metrics. The LF and SF lidar sensors have been compared over temperate forests to demonstrate the similarity and differences in measuring the structural characteristics of forests, such as canopy height (Blair et al., 1999; Popescu et al., 2011). However, examples of such studies over tropical forests with dense and structurally complex canopy cover are scarce. Meyer et al., (2013) used the two lidar datasets to examine changes in forest biomass over time, and Fricker et al. (2012) used the two types of observations to develop techniques to correct for LF lidar observations over topographically complex terrain in the tropics.

Here, compare SF and LF lidar performance in quantifying the vertical structure and biomass across a forest-savanna boundary region encompassing a natural transition from grasslands (very low AGB) to very high aboveground biomass and structurally complex ancient afrotropical forests (>18,000 years), including many very large trees (>60m), located in central Gabon. The study focuses on variations of 3-D forest structure at the footprint and landscape scales. LF lidar and commercial SF lidar for the study site were collected as part of the NASA and European Space Agency (ESA) AfriSAR campaign with the goal of verifying the performance of future spaceborne lidar (GEDI) and radar sensors such as ESA's BIOMASS mission and NASA-ISRO Synthetic Aperture Radar (NISAR) systems for ecosystem studies (Le Toan et al., 2011; Saatchi et al., 2011b) in quantifying vertical forest structure and AGB. The paper reports on the comparison of LF and SF data over Lopé National Park in central Gabon and examines the performance of LF simulated waveforms in detecting structure and estimating forest aboveground biomass.

4.2 Material and method

4.2.1 Study Area

The study area is located in north Lopé National Park (LNP) in central Gabon (Figure 4.1) and covers an area of approximately 50 km^2 within the swath that will be surveyed by

the proposed BIOMASS satellite. LNP is located in the western Lower Congolian semi-evergreen forests of central Africa (White et al., 1983) and is made up of dynamic, diversified vegetation types. Forest boundaries have been advancing, invading savanna grasslands under the influence of post-Pleistocene climate (White et al., 1983; White et al., 1987, Maley et al., 1996), yet anthropogenic uses of fire (Ngomanda et al., 2009), together with the presence of elephant seed dispersal and browsing (Blake et al., 2009) have been modifying and maintaining the Lopé forest edge configuration and creating a complex system of forest types across the forest-savanna boundary.

Annual rainfall at the study area averages 1500 mm (SEGC data, 1984–2016), and there are two rainy seasons and two dry seasons. The longer dry season extends from June to mid-September, followed by the longer rainy season from mid-September to mid-December. The shorter dry and rainy seasons are less regular and can vary in duration and intensity. The savanna and forest vegetation are on undulating terrain ranging from 230 to 470 m a.s.l. within slopes that can reach more than 30 degrees in the western region of the study area.

Most of the vegetation in the study area can be divided into four categories of structural characteristics: 1) savanna grasslands (SAV) dominated by herbaceous plants and fire-resistant woody shrubs. Two types of forest patch occur in the savanna-dominated areas: gallery forests over rocky or sandy soil along small watercourses; and isolated patches or "bosquets" of anthropogenic origin, mainly found on hilltops. In this study, within the continuous forest extent, forest cover can be categorized as: 2) Young colonizing forests that grow as a result of fire suppression at the edge of forest-savanna boundary (YCF), and 3) Okoumé (Aucoumea klaineana) dominated forests (ODF), containing mainly Okoumé and Azobe (Lophira alata) trees. 4) Marantaceae and Mature old growth forests (OGF) are found a greater distance from the current savanna edge and have greater species diversity and structure complexity (White et al., 1997; Blake et al., 2009). These old forests are mainly located in the western portion of the study area at the edge of the Massif du Chaillu Pleistocene forest refuge and cover a more complex, steeply hilly terrain. Based on the SF lidar-derived canopy height model (CHM), we manually delimited four sub-areas across the site to represent the four major vegetation types for their variations in structure and aboveground biomass (Figure 4.1).

4.2.2 Field data collection

Forest inventory data were collected in field plots of either 1 ha (ODF, OGF, SAV; n=9) or 0.5 ha (YCF; n=3) that were designed to span a gradient of aboveground biomass from very low to high biomass values. In each plot, all stems greater than 10 cm in diameter at breast height (dbh, at 1.30 m), or above stem irregularity and buttresses, were labelled and diameters and heights were measured. For the plots in SAV and YCF, stems 5–10 cm in dbh were also measured as they can represent a substantial portion of aboveground biomass in such vegetation types. In all plots, trees were identified to genus level and where possible to species level. Wood density values were extracted from global data sets. Using diameter, height, and wood density of trees, we calculated the aboveground biomass (dry weight) of each stem using the Chave et al., (2014) pantropical moist tropical forest allometric equation (eq 4.1).

$$\mathrm{AGB\ (kg)} = 0.0673 \times (\rho \times \mathrm{dbh}^2 \times \mathrm{ht})^{0.976} \qquad (4.1)$$

were dbh is in cm, ht is in m, and ρ is the wood density in $g.cm^{-3}$. The total AGB at plot level was then obtained by summing individual stem biomass estimates and converting it to $Mg \cdot ha^{-1}$.

4.2.3 Lidar data and processing

4.2.3.1 Small-footprint lidar

The SF DR lidar data were collected using a Riegl VQ480U sensor mounted on a helicopter model EC 135 in July 2015 with a variable point density and footprint diameter of ~10 cm. Data were pre-processed to remove artefacts due to helicopter motion. This provided a more uniform point density of ~10 $points.m^{-2}$ for vegetation characterization. In this study, digital terrain model (DTM), slope, canopy height model (CHM) and canopy metrics derived from simulated pseudo-waveforms were computed based on the following steps: first, ground returns were classified using the Progressive Triangulated Irregular Network (TIN) densification algorithm (Axelsson et al., 2000), and a 1-m DTM was created.

Slope (%) maps were derived from the DTM. Second, normalized height (i.e. the height above ground) was obtained for each point of the point cloud by subtracting ground elevation (obtained from the DTM) from the raw point elevation value, and the 1-m CHM was then computed using the highest points. Lastly, within each LVIS footprint, the SF lidar point cloud was clipped and pseudo-waveforms were simulated by convoluting the returns within each footprint (Figure 4.2a) (Popescu et al., 2011):

$$WV(z) = \left[\sum_{i \in U} I_i \cdot w_h(x_i, y_i)\right] \circledast w_v\left(\frac{2 \cdot z}{c}\right) \tag{4.2}$$

$$U = \left\{i: \sqrt{(x_i - x_0)^2 + (y_i - y_0)^2} \leq r \text{ and } |z_i - z| \leq \frac{\Delta h}{2}\right\} \tag{4.3}$$

where (xi, yi, zi) are the coordinates of each discrete return, (x0, y0) refer to the coordinates of the footprint center, r is the footprint radius (i.e., defined as half of the $e^{(-2)}$ width rather than half of the full width at half maximum), Δh is the sensor discretization interval (15 cm for LVIS), U denotes the set of those SF lidar returns within the SF footprint (25m in diameter), Ii is the intensity of each return, and ⊛ denotes the convolution operator. The Gaussian distribution of energy both along and across the laser beam was approximated by wv and wh:

$$w_h(x, y) = \exp\left[-2\frac{(x_i - x_0)^2 + (y_i - y_0)^2}{r^2}\right], \tag{4.5}$$

$$w_v(t) = \exp\left[-2\frac{(t - t_0)}{\sigma_t^2}\right], \tag{4.6}$$

where t_0 is a reference time corresponding to the peak of an emitted pulse, and σ_t is the interval from t_0 to the time at which the intensity along the beam drops to $e^{(-2)}$ of the maximum. The pulse duration was set to 10 ns (Blair et al. 1999).

After simulating the LVIS waveforms, canopy relative height metrics (SF RH) were calculated based on the cumulative waveform energy (i.e., 10%, 25%, 50%, 75%, 98% and 100%; RH10, RH25, R50, RH75, RH98 and RH100). The SF data processing was done using FUSION/LDV (McGaughey 2017), Lastools (Isenburg 2017), R (R Core Team 2017) and Matlab (Matlab 2017) softwares.

4.2.3.2 Large-footprint lidar

The LF full-waveform lidar data were acquired in February 2016 using the LVIS sensor, developed and operated by the Laser Remote Sensing Laboratory at NASA's Goddard Space Flight Center. In this study, LVIS was mounted on the NASA Langley B200 aircraft and flown at ~7315 m with a footprint diameter of 25 m and nominal spacing of ~10 m both along and across track. LVIS footprints were geo-located to the global reference ellipsoid WGS 84, using a combination of GPS and Inertial Navigation System (INS) information (Blair et al. 1999; Hofton et al., 2002). Our preliminary analyses indicate that LVIS data geolocation match very well with that of SF DR lidar data and that sensor comparison did not require any further geolocation correction.

LVIS is a full-waveform digitizing system that records the vertical distribution of nadir-intercepted surfaces at 15 cm vertical resolution (Hyde et al., 96) using the return energy of Gaussian-shaped optical pulses at a wavelength of 1064 nm (Blair et al., 1999) (Fig. 2b). Essentially, the amplitude of a LVIS waveform signal is proportional to the energy reflected from canopy-intercepted surfaces and the ground (Swatantran et al., 2011). For each LVIS waveform, ground elevation (ZG) was defined as the center of the lowest mode in the waveform greater than mean signal noise (Swatantran etal., 2011; Blair et al., 2006), and height metrics relative to ground elevation (LF RH) were calculated based on the normalized cumulative return energy (Swatantran et al., 2011; Huang et al., 2013). In general, RH100 is considered a noisy metric because it is associated with the first return and depends strongly on the signal to noise ratio setup in LF lidar measurements. In comparing LF to SF lidar measurements, RH98 (heights at 98 percentiles of energy) was found to be more precise. Other metrics such as canopy cover can be computed based on the LVIS waveform. However, for this study, we only used ZG, RH75 and RH98 (representing ground

elevation, canopy height at 75% and 98% of the laser return energy, respectively) for comparison purposes and AGB modeling.

4.2.4 Comparison of small- vs. large-footprint lidar-derived metrics for ground and forest structure attribute retrieval

4.2.4.1 Ground and Canopy Height Comparison

We compared ground elevation (ZG) and top-of-canopy height (RH98) retrieved from small- and large-footprint lidar at different spatial levels (LVIS footprint and grid) over the sub-areas selected to represent the gradient of successional stages of vegetation found in the study area (see section 4.2.1). For each metric, the comparison was performed using the two-sided Wilcoxon–Mann–Whitney rank-sum (Bauer 1972) and equivalence tests (Robinson 2005), at a significance level of 0.05 in R (R Core Team 2017). At the footprint level, SF ZG was computed as the mean of ground elevation from DTM within the footprint area. At the grid level, SF and LF lidar-derived ground elevation and top-of-canopy height were averaged at 25-m, 50-m and 100-m spatial resolutions leading to mean ZG (SF_ZG_MEAN and LF_ZG_MEAN) and mean RH98 (SF_RH98_MEAN and LF_RH98_MEAN). The grid cell resolutions were tested to quantify (i) how well the two observations characterize the landscape scale variations of aboveground forest structure and (ii) how differences between the two systems scales with grid cell resolutions. This approach will also allow us to understand how many footprints from LF sensors are required to capture landscape variability in forest structure and biomass. This, in turn, will provide useful information regarding GEDI projected sampling densities to accurately retrieve canopy height and biomass over complex tropical landscapes.

4.2.4.2 Small-footprint discrete return lidar

We developed relationships between SF and LF height metrics and ground-derived AGB. In this study, we used the *nls* function in R (R Core Team 2017) to calibrate a non-linear relationship between AGB and lidar metrics at plot level. For each sample plot, the mean of SF lidar-derived CHM and LF lidar–derived RH75 were computed (SF_MCH; LF_RH75_MEAN) and used as independent variables for modeling AGB. We developed a

power-law relationship between the corresponding height metric and AGB. The accuracy of the model predictions was evaluated in terms of the coefficient of determination (R^2), Root Mean Square Error (RMSE) and Bias in $Mg \cdot ha^{-1}$:

$$AGB = \beta_0 \cdot \overline{H_L}^{\beta_1} + \varepsilon \quad \text{with } \varepsilon \sim N(0, \sigma^2) \tag{4.7}$$

$$RMSE = \sqrt{\frac{\sum_{i=1}^{n}(\hat{y}_i - y_i)^2}{n}} \tag{4.8}$$

$$Bias = \frac{1}{n}\sum_{i=1}^{n}(\hat{y}_i - y_i) \tag{4.9}$$

where AGB is the aboveground biomass in $Mg\ ha^{-1}$, ($\overline{H_L}$) is the lidar-derived mean forest canopy height metric (either SF_MCH_MEAN or LF_RH75_MEAN), n is the number of plots, y_i is the observed value for plot i, and $\hat{y}_i$ is the predicted value for plot i. Moreover, relative RMSE and biases were calculated by dividing the respective absolute values (eqs. 4.8 and 4.9) by the mean of predictions.

For validation purposes, the AGB models were embedded in a bootstrap procedure with 100 iterations. In each bootstrap iteration, we drew 12 times with replacement from the 12 available samples. In this procedure, on average 44% of the total number of samples (~5 samples) are not drawn. These samples were subsequently used as holdout samples for independent validation. In each bootstrap iteration, Adj.R^2 and relative and absolute RMSE and bias were computed based on the linear relationship between observed and predicted AGB using the holdout samples. Wilcoxon–Mann–Whitney rank-sum and equivalence tests were also used to assess if the mean of predicted AGB from the 100 iterations and the observed AGB mean differ at a significance level of 5%.

SF_MCH and LF_RH75_MEAN were computed for the entire site at a spatial resolution of 100 m, and the fitted models were applied to map AGB at landscape level. SF- and LF-derived AGB estimates were then compared at landscape level and summarized for the four vegetation types described in Section 2.1.

An uncertainty analysis was also performed at the landscape level for the entire site and for each subarea (Section 2.1) by integrating the pixel level errors over the regions of interest and accounting for spatial autocorrelation of the errors as follows (McRoberts 2006; Weisbin et al., 2014):

$$\sigma^2_{AGB}(ROI) = \frac{1}{m^2}\sum_{i=1}^{m}\sum_{j=1}^{m} cov(\sigma_{i,}\sigma_j) = \frac{1}{m^2}\left(\sum_{i=1}^{m}\sigma_i^2 + 2\sum_{i=1}^{m}\sum_{i<j}^{m}\rho(d)\,\sigma_i\sigma_j\right) \quad (4.9)$$

where σ^2_{AGB} (ROI) is the variance of the estimator for the mean AGB for the regions of interest (entire study area or subareas), *m* is the number of pixels; cov represents the covariance of pixel errors, σ_i is the estimated standard error of AGB values at the i-th pixel, and $\rho(d)$ is the spatial correlation function based on an exponential semivariogram model depending on the distance d between pixels *i* and *j* (Weisbin et al., 2013). The square root of the variances (σ^2_{AGB}) results in the standard error (SE), which was used as the uncertainty.

4.2.5 Impacts of Sample Size on AGB Estimation

The GEDI instrument will operate with a footprint of 25 m similar to LVIS LF, but each footprint will be separated by 60 m along track and 500 m across track between each of 10 tracks. In order to evaluate the performance of GEDI for modelling AGB in tropical forests, we examine the number of footprints required to have a relatively unbiased estimate of AGB at 1-ha. By subsampling the LVIS LF footprints, we assessed the impacts of LF sample size on AGB modelling at the plot level. The footprint density from LVIS varied at different locations in the study area because of the spatial variation of overlapping flight lines during the campaign. On average, 72 ± 23 (sd) footprints were registered over each field plot. We randomly downscaled the number of footprint to 10, 5, 3 and 1 for each plot, and LF_RH75_MEAN was then computed for AGB modeling. For the simulation where only one footprint shot was kept, we used the LF RH75 value for AGB modelling. Simulations were repeated 100 times and distribution histograms of R^2, RMSE, Bias and model parameters were computed for each subsampling case. Thus, we were able to assess

how well one GEDI footprint randomly located within a 1-ha plot will be able to retrieve plot AGB.

4.3 Results and discussion

4.3.1 Comparison of SF and LF lidar-derived ground elevation and canopy height at footprint level

SF and LF lidar-derived ground elevation were strongly correlated (Adj.R^2=0.99; Figure 4.3). The mean difference in ground elevation across all vegetation types was 1.01 ± 0.99 m (n.s.; p-value = 0.78; Wilcoxon–Mann–Whitney rank-sum test). Difference in ground elevation between SF and LF was highest in the most structurally complex OGF subarea (RMSE=2.46 m, RMSE=0.63%). LF and SF lidar-derived RH98 showed significant differences at footprint level for ODF, YCF and SAV (mean RMSE= 2.06 ± 1.20 m, mean bias=0.81 ± 0.71 m). Even though differences in RH98 could be higher than 10 m (RMSE ~ 4 m) in OGF, it was not significant for the four sub regions combined and did not show a bias across the height range (bias=0.47m). Yet, based on equivalence tests, SF and LF lidar-derived ground elevation (ZG) and top-of-canopy height (RH98) at footprint level were found equivalent across all vegetation types.

Although we did not find significant differences between the two measurements when analysing all footprints within the sub regions, there were some large differences between the two datasets at individual footprint level (Figure 4.3). These differences reached up to 10 and 20 m for ground elevation and top-of-canopy height detection, respectively. Errors remained random though across footprints. By analysing individual footprints with large differences in ZG and RH98, we found several potential sources of uncertainty in individual measurements when comparing the two data sets:

i) Ground topography is a significant source of error in LF lidar quantification of ZG and RH98. Slope (both its variations within a LF lidar footprint and its orientation against lidar observation) has been shown to induce errors in ground elevation retrieval (Hofton et al., 2002a; Lee et al., 2015; Hofton et al., 2002b; Park et al., 2014). In our study site, particularly under dense canopy, the individual LF lidar ZG values may have large errors

(Figure 4.4). However, similar errors may also appear in SF retrieval of ZG. Depending on pulse density and observation geometry (i.e., viewing angles), there may be no ground-classified points over slopes and the interpolated DTM may miss micro-topographical variations across the landscape. If the individual LF lidar and the simulated SF lidar footprint fall over complex terrains with dense forest cover, the errors from both measurements can introduce large differences in the footprint level ZG values. In most studies, the difference in ZG is often attributed to uncertainties associated with LF measurements (Popescu et al., 2011). However, in dense tropical forests, SF measurements may also have errors in detecting ZG depending on the pulse density and ground interpolation method (Silva et al., 2017).

ii) Canopy structure might also introduce uncertainty when calculating canopy height from LF lidar. In a study carried out in Sierra National Forest, Hyde et al., (2005) reported that differences between field and LVIS measurements of canopy height and biomass were mainly attributable to the spatial configuration of canopy elements and were less sensitive to topography, crown shape, or canopy cover. For instance, in our study, we identified that most of the large differences in RH98 were found in footprints located at higher slopes and across the transition from savanna to forest. In this case, taller trees located at the edges were detected by the SF lidar, but not detected from the LF lidar because of the low laser intensity at the edge of the footprint. In LF systems, Gaussian waveforms drop off in power across the footprint, resulting in a lack of sensitivity to canopy material progressively towards the edges of the footprint (Hyde et al., 2005). Figure 4.5 shows examples of footprints and geometry of canopy within the footprint from SF simulations over three different terrains and conditions where RH98 from LF may be very similar (Figure 4.5 a1-d1), larger (Figure 4.5 a2-d2) or smaller (Figure 4.5 a3-d3) than SF. In most comparisons between LF and SF data, it is considered that SF lidar derived RH98 must be higher than LF lidar. SF measurements may have a return from a small leaf on the top of the canopy but LF requires enough leaves on the top of the canopy to have a significant return higher than SNR. However, when simulating the LF canopy height metrics from SF measurements, the difference may be in both directions.

iii) Simulation of LF data from SF measurements may also be a source of error in comparing RH98 at individual footprint level. Our result in Figure 4.3b shows that this error can be large and without any preference or bias towards one lidar measurement type. Simulation of LF footprint waveforms from SF measurements may include errors associated with the geometry of measurements, the form of Gaussian weighting of the small footprint data, and small geolocation error that may partially include or exclude large trees around the footprint edges.

4.3.2 Comparison of SF- and LF-derived ground elevation and canopy height at grid levels

SF_ZG_MEAN and LF_ZG_MEAN were strongly correlated (Adj.R^2=0.99) with RMSE ≤ 1.02 m (0.31%) and bias ≤ 0.31 m (0.09%) whatever the spatial resolution (Figure 4.5). Moreover, LF_RH98_MEAN and SF_RH98_MEAN were also strongly correlated at all spatial scales with RMSE ≤ 1.66 m (6.14%) and bias ≤ 0.62 m (2.94%). The difference between SF and LF measurement of ZG_MEAN and RH98_MEAN decreased ~32% in relative RMSE from 25 to 100 m resolutions. Equivalence tests showed that SF and LF for both ZG_MEAN and RH98_MEAN were equivalent across all spatial resolutions, but Wilcoxon–Mann–Whitney rank-sum tests showed significant differences in SF and LF lidar-derived RH98 at spatial resolutions of 25 and 50 m (Figure 4.5 a2, b2).

LF predominantly overestimated ground elevation when compared with SF lidar, yet differences exceeding 2 m were only found in the OGF area (Figure 4.6). For RH98_MEAN, we observed both under and overestimation, and differences ≥ 1.5 m were also found in the OGF area. As the grid cell size of the maps coarsened from 25 to 100 m, the spread of the differences of SF and LF also decreased as shown by the distribution of their differences (Figure 4.6a-g1.2-3.2). The comparison of the two sensors at grid cells revealed the importance of aggregated measurements to capture the landscape variations of the forest structure. By averaging several LF lidar footprints within a 1-ha area, random errors between the two measurements were reduced significantly, allowing the measurements to converge in representing the landscape characteristics of the forests in the study area. Comparison of Figures 4.3 and 4.5 readily shows the impact of LF footprint aggregation even with 25 m grid cells.

4.3.3 Comparison of SF and LF Aboveground Biomass Models

4.3.3.1 Biomass model performance

SF_MCH and LF_RH75_MEAN were significantly correlated with AGB at plot levels. AGB was overestimated in both SF (Bias: 1.24 $Mg \cdot ha^{-1}$) and LF (bias: 2.47 $Mg \cdot ha^{-1}$) models after bootstrapping the performance with 100 repetitions. However, the Wilcoxon–Mann–Whitney rank-sum and equivalent tests showed that SF and LF AGB estimates at plot level are both equivalent to the ground-estimated AGB (p-value ≥ 0.93). Figure 4.7 shows the SF and LF derived AGB estimates from the bootstrap procedure. According to these tests, the mean AGB estimates from the bootstrapping procedure are equivalent with ground-estimated AGB (p-value ≥ 0.89) as well. SF and LF AGB estimates at plot level, both from the model and bootstrapping procedure, are also equivalent (p-value ≥ 0.88).

At the 1-ha scale, the number of plots was limited to 12, and although this captures variation in biomass across the forest types, it may not be enough to develop a more robust cross-validation test of model performance. However, the accuracies, both for training and validation models, presented herein were similar to those reported in previous studies (Drake et al., 2002a; Meyer et al., 2013). This analysis can be done at different spatial scales to allow more GEDI footprints over larger landscapes, but requires either large ground plots or a more complex error propagation if compared with SF lidar-derived AGB. A more complex sampling approach to exactly mimic the GEDI samples over the landscape was beyond the scope of this study and hence is not considered in this paper.

4.3.3.2 Aboveground biomass maps

Landscape-wide AGB estimates based on the models from Table 4.1 were mapped at 1-ha grid cells (100 m x 100 m) and are showed in the Fig.8. At the map scale, the equivalence test showed that LF and SF lidar AGB maps are equivalent at landscape level (p-value > 0.05). However, Wilcoxon–Mann–Whitney rank-sum tests showed significant RMSE and bias (p-value ≤ 0.01) of 6.34 $Mg \cdot ha^{-1}$ (2.84%) and 11.27 $Mg \cdot ha^{-1}$ (5.05%) between the two maps. The difference map (Figure 4.8b) showed LF-derived AGB was larger across all old growth forest types that appear to be distributed across areas with slopes larger than 10 degrees (Figure 4.8c). The uncertainty of the AGB estimates at landscape

level for the entire study area and for the four regions of interest are derived by taking into account the pixel base model errors from the bootstrapping approach and the spatial correlation of errors as presented in Table 4.2.

SF and LF lidar-derived biomass models are equivalent in performance based on Table 4.1, but different in coefficients and if used interchangeably to predict forest AGB over the landscapes can introduce larger random or systematic errors. However, individually they provide similar mean biomass density and similar uncertainty over the study area. Results shown in Table 4.2 also suggest that the difference between the two approaches is within the margin of error in AGB estimation for each lidar approach (Drake et al., 2002a; Hofton et al., 2002). The results suggest that models developed with SF lidar data at landscape scale (≥ 1-ha) may be used for LF lidar data as long as equivalent height metrics between the two sensors are identified (e.g., mean top canopy height).

4.3.4 Impacts of LF lidar sample size on AGB estimation

The impact of LF sample size on the AGB modeling and estimation was examined by randomly selecting 10, 5, 3 and 1 footprint out of more than 50 footprints in each 1-ha plot (Figure 4.9). Reduced sample size resulted in increased RMSE and bias values, but the effect was small until only 1 lidar footprint was selected (Figure 4.8 a1-2, b1-2). The variability of R^2 and parameters *a* and *b* of the AGB models increased slightly in reduced sample sizes (Figure 4.9 c1-2, d). The result suggests that a minimum of three samples can potentially provide an unbiased estimate of AGB of a 1-ha area.

GEDI lidar is expected to provide global (between ± 51° latitude) estimates of forest height structure at different spatial sampling schemas (Stavros et al., 2017) such that unbiased forest biomass estimates are provided at 1-km^2 (100 ha) resolution. However, by clustering the samples along tracks, there is a strong probability of having a minimum of 3 footprints within a 1-ha area. The spatial distribution of a large number of 1-ha biomass values can help us to improve the GEDI final product from 100-ha to 1-ha through geostatistical modeling or machine learning approaches (Xu et al., 2017).

4.4 Conclusion

In this paper, we performed a comparison of small and large footprint lidar measurements of ground and forest structure, including aboveground biomass, across an AGB transition zone in central Gabon. We showed that in the dense and complex tropical forests of Central Gabon, the LF lidar measurements are equivalent to SF lidar measurements in characterizing ground elevation and maximum forest height. In addition, comparison of gridded LF lidar height with ground plots showed that an unbiased estimate of aboveground biomass at 1-ha can be achieved with a sufficient number of large footprints ($n > 3$). The approach and results from this study can serve as a methodological basis for examining GEDI performance for estimating and mapping tropical forest structure and biomass. In addition, our results demonstrate that SF lidar measurements can be readily used for both calibration and validation of LF lidar measurements of structure and biomass over different tropical forest structures.

References

Asner, G. P., Mascaro, J .(2014). Mapping tropical forest carbon: Calibrating plot estimates to a simple lidar metric. Remote Sens. Environ., 140, 614-62 DOI:10.1016/j.rse.2013.09.023.

Axelsson, P. (2000). DEM generation from laser scanner data using adaptive TIN models, in International Archives of Photogrammetry and Remote Sensing, Netherlands: ISPRS, ch. XXXIII, 110–117.

Bauer, F. 1972. Constructing confidence sets using rank statistics, J. Americ. Stat. Assoc., 67, 687–690.

Blair, J. B., Hofton, M. A., Rabine, D. L. (2006). Processing of NASA LVIS elevation and canopy (LGE, LCE and LGW) data products, version1.01, 2006, NASA Goddard Space Flight Center, Greenbelt, MD, USA, Nov. 12, Available:<https://lvis.gsfc.nasa.gov>

Blair, J., Rabine, D., Hofton, M. (1999). The Laser Vegetation Imaging Sensor: a medium-altitude, digitisation-only, airborne laser altimeter for mapping vegetation and topography, ISPRS J. Photogramm. Remote Sens., 54, 115-122, DOI: 10.1016/s0924-2716(99)00002-7.

Blair, J. B., Hofton. M. A. (1999). Modeling laser altimeter return waveforms over complex vegetation using high-resolution elevation data. Geophys. Res. Lett., 26(16), 2509–2512, DOI:10.1029/1999GL010484.

Blake, S., Deem, S.L., Mossimbo, E., Maisels, F., Walsh, P. (2009). Forest elephants: tree planters of the Congo. Biotropica, 41 (4), 459-468, DOI: 10.1111/j.1744-7429.2009.00512.x.

Clark, M. L., Clark, D. B., Roberts, D. A. (2004). Small-footprint lidar estimation of sub-canopy elevation and tree height in a tropical rainforest landscape. Remote Sens. Environ., 91(1), 68-89, DOI: 10.1016/j.rse.2004.02.008.

Chave, J., M. Rejou-Mechain, A. Burquez, E. Chidumayo, M. S. Colgan, W. B. Delitti, A. Duque, P. Fearnside, R. Goodman, M. Henry, A. Martínez-Yrízar, W. Mugasha, H. Muller-Landau, M. Mencuccini, B. Nelson, A. Ngomanda, E. Nogueira, E. Ortiz-Malavassi, R. Pélissier, P. Ploton, C. Ryan, J. Saldarriaga, and G. Vieilledent. (2014). Improved allometric models to estimate the aboveground biomass of tropical trees. Glob. Chang. Biol., 20(10), 3177–3190, DOI:10.1111/gcb.12629.

Drake, J. B., Dubayah, R. O., Knox, R. G., Clark, D. B., Blair, J. B. Sensitivity of large-footprint lidar to canopy structure and biomass in a neotropical rainforest. (2002a). Remote Sens. Environ., 81(2-3), 378-392, DOI:10.1016/s0034-4257(02)00013-5.

Drake, J. B., Dubayah, R. O., Clark, D. B., Knox, R. G., Blair, J. B, Hofton, M. A., Chazdon, R. L., Weishampel, J. F. (2002b). Estimation of tropical forest structural characteristics, using large-footprint lidar. Remote Sens. Environ., 79 (2-3), 305-309, DOI:10.1016/S0034-4257(01)00281-

Dubayah, R. O., Drake, J. B. (2000). Lidar Remote Sensing for Forestry. J. For., 98 (6), 44-46.

Fricker, G. A., Saatchi, S. S., Meyer, V., Gillespie, T. W., Sheng. Y. (2012). Application of semi-automated filter to improve waveform lidar sub-canopy elevation model. Remote Sens., vol. 4, 6, 1494-1518, DOI: 10.3390/rs4061494.

García, M., Riaño, D., Chuvieco, E., Danson, F. (2010). Estimating biomass carbon stocks for a Mediterranean forest in central Spain using lidar height and intensity data, Remote Sens. Environ., 114, 4, 816–830, DOI: 10.1016/j.rse.2009.11.021.

Hudak, A.T.; Strand, E.K.; Vierling, L.A.; Byrne, J.C.; Eitel, J.U.H.; Martinuzzi, S.; Falkowski, M.J. (2012). Quantifying aboveground forest carbon pools and fluxes from repeat lidar surveys. *Remote Sens. Environ.*, *123*, 25–40, doi:10.1016/j.rse.2012.02.023.

Hofton, M., Blair, J. (2002). Laser altimeter return pulse correlation: a method for detecting surface topographic change, J. Geodyn., 34 (3-4), 477–489, DOI:10.1016/S0264-3707(02)00043-1.

Hyde, P., Dubayah, R., Peterson, B., Blair, J. B., Hofton, M., Hunsaker, C., Knox, R., Walker, W. (2005). Mapping forest structure for wildlife habitat analysis using waveform lidar: Validation of montane ecosystems, Remote Sens. Environ., 96(3-4), 427–437, DOI:10.1016/j.rse.2005.03.005.

Huang, W., Sun, G., Dubayah, R., Cook, B., Montesano, P., Ni, W., Zhang, Z. (2013). Mapping biomass change after forest disturbance: Applying lidar footprint-derived models at key map scales, Remote Sens. Environ., 134, 319–332, DOI: 10.1016/j.rse.2013.03.017.

Hofton, M., Rocchio, L., Blair, J., Dubayah, R. (2002). Validation of Vegetation Canopy Lidar sub-canopy topography measurements for a dense tropical forest, J. Geodyn., vol. 34(3-4), 491–502, DOI:10.1016/S0264-3707(02)00046-7.

Isenburg, M. (2017). Lastools-Efficient Tools for lidar Processing. Version 1.0-1.3, Nov. 15, 2017. Available: <http://lastools.org.>

Lee, S., Ni-Meister, W., Yang, W., Chen, Q. (2011). Physically based vertical vegetation structure retrieval from ICESat data: Validation using LVIS in White Mountain National Forest, New Hampshire, USA, Remote Sens. Environ., 115(11), 2776–2785, DOI: 10.1016/j.rse.2010.08.026.

Lefsky, M. A. (2010). A global forest canopy height map from the Moderate Resolution Imaging Spectroradiometer and the Geoscience Laser Altimeter System. Geophys. Res. Lett., 37(15), n/a, DOI:10.1029/2010GL043622.

Le Toan, T., Quegan, S., Davidson, M., Balzter, H., Paillou, P., Papathanassiou, K., Plummer, S., Rocca, F., Saatchi, S., Shugart, H., Ulander, L. (2011). The BIOMASS mission: Mapping global forest biomass to better understand the terrestrial carbon cycle. Remote Sens. Environ., 115(11), 2850-2860, DOI:10.1016/J.RSE.2011.03.020.

Lu, Q. Chen, G. Wang, E. Moran, M. Batistella, M. Zhang, G. V. Laurin, and D. Saah, (2012). Aboveground Forest Biomass Estimation with Landsat and lidar Data and Uncertainty Analysis of the Estimates, Int. J. For. Res., 2, 1-16, DOI: 10.1155/2012/436537.

Lefsky, M. A., Cohen, W. B., Parker, G. G., Harding, D. J. (2002). Lidar remote sensing for ecosystem studies. Bioscience, 52(1), 19-30.

Mascaro, J., Asner, G. P., Muller-Landau, H. C., van Breugel, M., Hall, J., Dahlin, K. (2011). Controls over aboveground forest carbon density on Barro Colorado Island, Panama. Biogeosciences, 8, 1615-1629, DOI: 10.5194/bg-8-1615-2011.

Maltamo, M., Erik, N., Vauhkonen, J. (2014). Forestry Applications of Airborne Laser Scanning: Concepts and Case Studies, Managing Forest Ecosystems, 1st ed. India: Delhi Book Store, pp. 1-464.

Matlab, Math. (2017). Graphs. Programming. Nov. 15. Available: <https://uk.mathworks.com/products/matlab.html>.

Meyer, V., Saatchi, S. S., Chave, J., Dalling, J. W., Bohlman, S., Fricker, G. A., Robinson, C., Neumann, M., Hubbell, S. (2013). Detecting tropical forest biomass dynamics from repeated airborne lidar measurements. Biogeosciences, 0, pp. n/a, DOI:10.5194/bg-10-5421-2013.

McRoberts, R. E. (2006). A model-based approach to estimating forest area, Remote Sens. Environ., 103(1), 56–66, DOI:10.1016/j.rse.2006.03.005.

Maley, J. (1996). The African rain forest: main characteristics of changes in vegetation and climate from the Upper Cretaceous to the Quaternary. Proc. Roy. Soc. Edinburgh, 104, 31-73.

McGaughey, R. (2017). FUSION/LDV: Software for LIDAR Data Analysis and Visualization 2015, Nov. 15. Available: http://forsys.cfr.washington.edu/fusion/fusionlatest.html.

Næsset, E. (1997). Estimating timber volume of forest stands using airborne laser scanner data. Remote Sens. Environ., 61(2), 246-253, DOI:10.1016/s0034-4257(97)00041-2.

Næsset, E. (2002). Predicting forest stand characteristics with airborne scanning laser using a practical two-stage procedure and field data. Remote Sens. Environ., 80(1), 88-99, DOI: 10.1016/S0034-4257(01)00290-5.

Nelson, R., Gobakken, T., Næsset, E., Gregoire, T. G., Stahl, G., Holm, S., Flewelling, J. (2005). Lidar sampling — Using an airborne profiler to estimate forest biomass in Hedmark County, Norway. Remote Sens. Environ., 123, 563-578, DOI: 10.1016/J.RSE.2011.10.036.

Ngomanda, A., Chepstow-Lusty, A., Makaya, M., Favier, C., Schevin, P., Maley, J., Fontugne, M., Oslisly, R., Jolly, D. (2009). Western equatorial African forest-savanna mosaics: a legacy of late Holocene climatic change?. Clim. Past., 5, 647-659, DOI: 10.5194/cp-5-647-2009.

Park, T., Kennedy, R. E., Choi, S., Wu, J., Lefsky, M. A., Bi, J., Mantooth, J. A., Myneni, R. B., Knyazikhin, Y. (2014). Application of physically-based slope correction for maximum forest canopy height estimation using waveform lidar across different footprint sizes and locations: Tests on LVIS and GLAS', Rem. Sens., 6(7), 6566–6586, DOI: 10.3390/rs6076566.

Popescu, S. C., Zhao, K., Neuenschwander, A., Lin, C. (2011). Satellite lidar vs. small footprint airborne lidar: Comparing the accuracy of aboveground biomass estimates and forest structure metrics at footprint level. Remote Sens. Environ., 115(11), 2796-2797, DOI:10.1016/j.rse.2011.01.026.

Qi, W., Dubayah, R. O. (2016). Combining Tandem-X InSAR and simulated GEDI lidar observations for forest structure mapping. Remote Sens. Environ., 187(15), 253–266, DOI: 10.1016/j.rse.2016.10.018.

R Core Team. (2017). A language and environment for statistical computing. Austria: R Foundation for Statistical Computing, Nov. 15, 2017. Available: <https://www.R-project.org/>.

Robinson, A.P.; Duursma, R.A.; Marshall, J.D. (2005). A regression-based equivalence test for model validation: Shifting the burden of proof. *Tree Physiol*., *25*,903–913.

Saatchi, S. S., Harris, N. L., Brown, S., Lefsky, M., Mitchard, E. T. A., Salas, W., Zutta, B. R., Buermann, W., Lewis, S. L., Hagen, S., Petrova, S., White, L., Silman, M., Morel, A. (2011a). Benchmark map of forest carbon stocks in tropical regions across three continents. Proc. Natl. Acad. Sci., 108(24), 9899–9904, DOI: 10.1073/pnas.1019576108.

Saatchi, S., Marlier, M., Chazdon, R., Clark, D., Russell, A. (2011b). Impact of spatial variability of tropical forest structure on radar estimation of aboveground biomass. Remote Sens. Environ., 115 (11), 2836-2849, DOI: 10.1016/j.rse.2010.07.015.

Silva, C.A.; Hudak, A.T.; Vierling, L.A.; Klauberg, C.; Garcia, M.; Ferraz, A.; Keller, M.; Eitel, J.; Saatchi, S. (2017). Impacts of Airborne Lidar Pulse Density on Estimating Biomass Stocks and Changes in a Selectively Logged Tropical Forest. Remote Sens., 9, 1068, DOI: 10.3390/rs9101068

Stavros, N., Schimel, D., Pavlick, R., Serbin, S., Swann, A., Duncanson, L., Fisher, J. B., Fassnacht, F., Ustin, S., Dubayah, R., Schweiger, A., Wennberg, P. (2017). ISS observations offer insights into plant function, Nat. Ecol. Evol., 1(194), pp. n/a, DOI:10.1038/s41559-017-0194.

Swatantran, A., Dubayah, R., Roberts, D., Hofton, M., Blair, J. B. (2011). Mapping biomass and stress in the Sierra Nevada using lidar and hyperspectral data fusion, Remote Sens. Environ., 115(11), 2917-2930, DOI:10.1016/j.rse.2010.08.027.

White, F. (1983). The vegetation of Africa: A descriptive memoir to accompany the Unesco/AETFAT/UNESCO vegetation map of Africa. France: Courvoisier S.A., pp. 1-325

White, L., Abernethy, K. (1997). Guide de la Végétation de la Réserve de la Lopé, 2nd ed. Gabon: ECOFAC, 1-224.

Weisbin, C. R., Lincoln, W., Saatchi, S. (2014). A Systems Engineering Approach to Estimating Uncertainty in Above-Ground Biomass (AGB) Derived from Remote-Sensing Data, Syst. Eng., 17(3), 361–373.

Xu, L., Saatchi, S. S., Shapiro, A., Meyer, V., Ferraz, A., Yang, Y., Bastin, J. F., Banks, N., Boeckx, P., Verbeeck, H., Lewis, S. L., Muanza, E., Bongwele, E., Kayembe, F., Mbenza, D., Kalau, L. A., Mukendi, F., Ilunga, F., Ebuta, D. (2017). Spatial distribution of carbon stored in forests of the Democratic Republic of Congo, Sci. Rep., vol. 7, no. 15030, 1-12, DOI: 10.1038/s41598-017-15050-z.

Table 4.1. Nonlinear Power-Law Aboveground Biomass Models (N=12)

Lidar	Models	R^2	RMSE		Bias	
			$Mg \cdot ha^{-1}$	%	$Mg \cdot ha^{-1}$	%
SF	$AGB_{SF} = 7.56 \times SF\_MCH^{1.06}$	0.94	34.28	17.32	1.24	0.63
LF	$AGB_{LF} = 6.40 \times LF\_RH75\_MEAN^{1.11}$	0.93	37.28	18.72	2.47	1.24

Table 4.2. Summary of SF And LF Lidar-derived AGB estimates and uncertainties at landscape level for the entire study area and regions of interest.

Class of Vegetation	Area (ha)	SF Lidar		LF Lidar	
		Mean ± Std ($Mg \cdot ha^{-1}$)	U ($Mg \cdot ha^{-1}$; %)	Mean ± Std ($Mg \cdot ha^{-1}$)	U ($Mg \cdot ha^{-1}$; %)
OGF	74.15	320.13 ± 31.56	3.69 (1.15)	322.79 ± 38.87	4.35 (1.34)
ODF	32.42	323.72 ± 32.51	7.47 (2.30)	316.52 ± 32.82	8.19 (2.59)
YCF	15.92	48.97 ± 22.91	15.29 (31.22)	40.79 ± 19.88	17.97 (44.0)
SAV	51.69	12.68 ± 20.74	4.46 (30.17)	14.94 ± 22.60	5.26 (35.2)
Entire Study Area	5044	223.01 ± 121.43	3.86 (1.73)	220.4 ± 120.77	4.16 (1.89)

Std: standard error; U: uncertainty

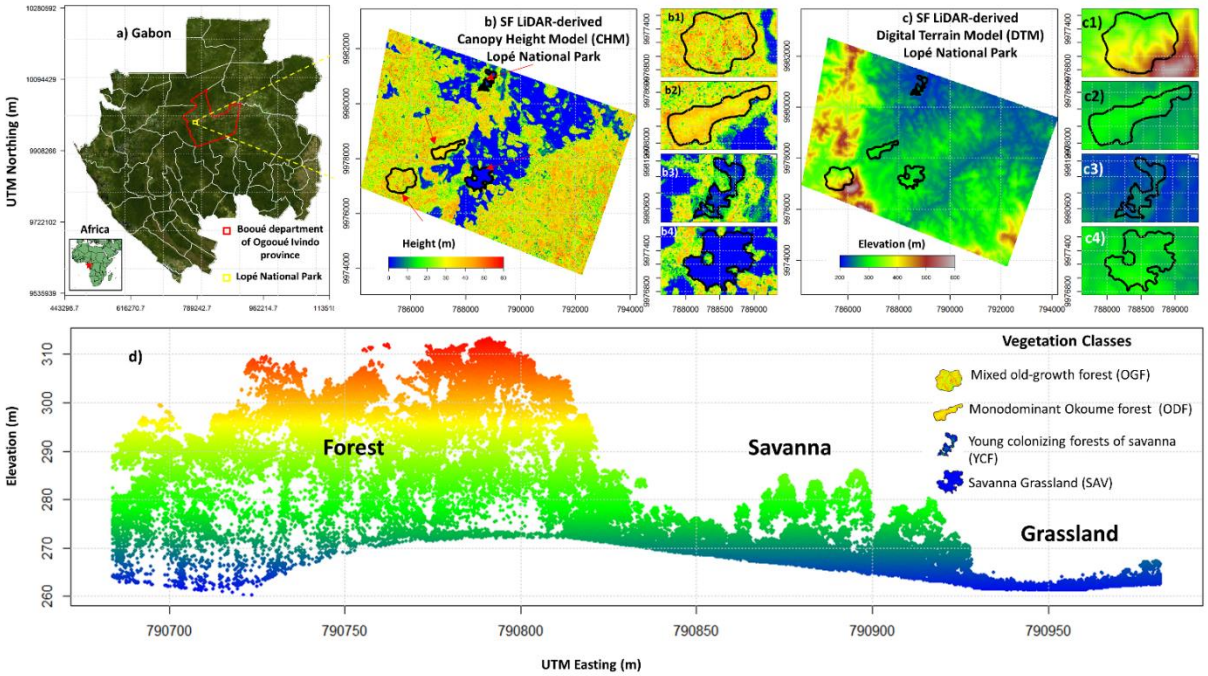

Figure 4.1. a) Study area, Gabon; b) SF lidar derived Canopy Height Model in Lopé National Park; c) SF-derived Digital Terrain Model in Lopé National Park; D) SF-derived point cloud profile across a forest-savanna transition zone; Mixed old-growth forest (OGF) b1-c1); Monodominant Okoumé forest (ODF) b2-c2); Young colonizing forests of savanna (YCF) b3-c3); and Grassland savanna (SAV) b4-c4)

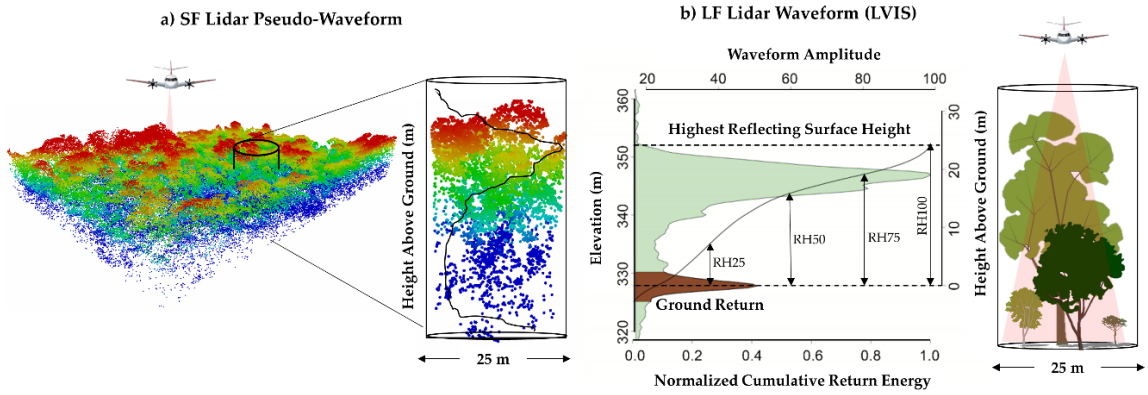

Figure 4.2. a) SF-derived pseudo-waveform (vertical black line) and b) LF-derived waveform. Canopy metrics, such as RH75, RH98 and RH100, were derived from the normalized cumulative return energy.

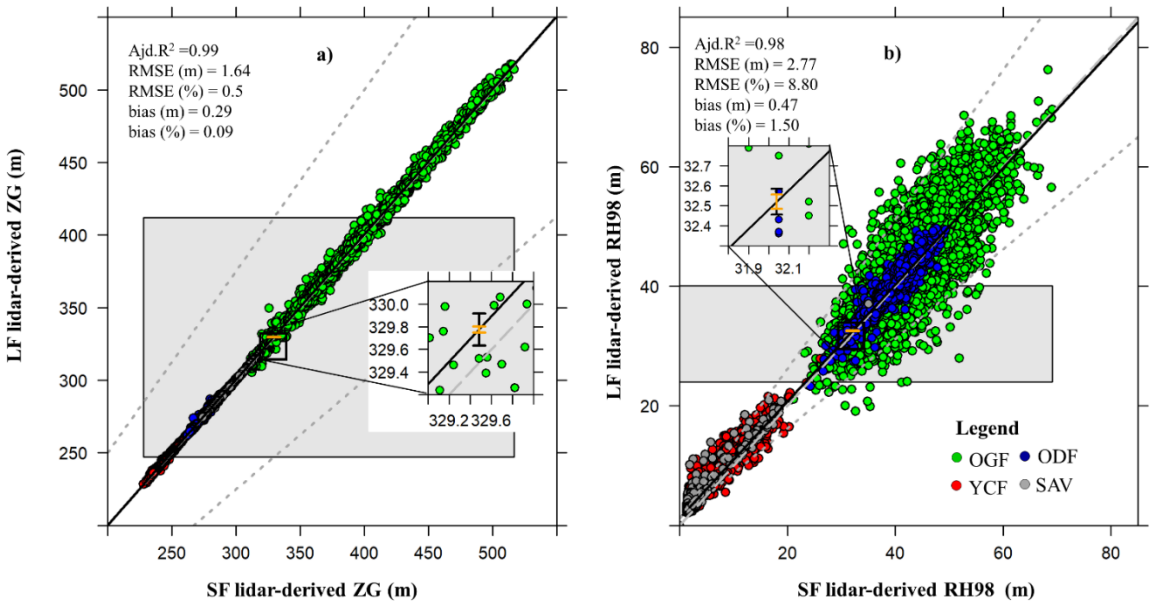

Figure 4.3. a) Comparison of small-footprint (SF) and large-footprint (LF) lidar-derived ground elevation and (b) top-of-canopy height at footprint level using the equivalence test. Mixed old-growth forest (OGF); Monodominant Okoumé forest (ODF); Young colonizing forests of savanna (YCF); and Grassland savanna (SAV). The equivalence plot design presented herein is an adaptation of the original equivalence plots presented by Robinson (2015), examples are showing in Silva et al. (2017). The grey polygon (SF in light grey and LF in dark grey) represents the ± 25% region of equivalence for the intercept, and the orange vertical bar represents a 95% confidence interval for the intercept. The LF ZG and RH98 are equivalent to SF ZG and RH98 on both intercept and slope as long as the orange bar remain completely within the grey polygon. If the grey polygon is lower than the orange vertical bar, the measurements would be negatively biased; and if it is higher than the orange vertical bar, the LF ZG and RH98 are positively biased. Moreover, the grey dashed line represents the ± 25% region of equivalence for the slope, the fit line is within the dotted lines and the black vertical bar is within the grey rectangle, indicating that the pairwise measurements are equivalent. An orange and black vertical bar that are wider than the region outlined by the grey dashed lines indicates high variance for SF measurements. The white dots are the pairwise measurements, and the solid line is a best-fit linear model for the pairwise measurements. The light grey dashed line represented the 1:1 relationship.

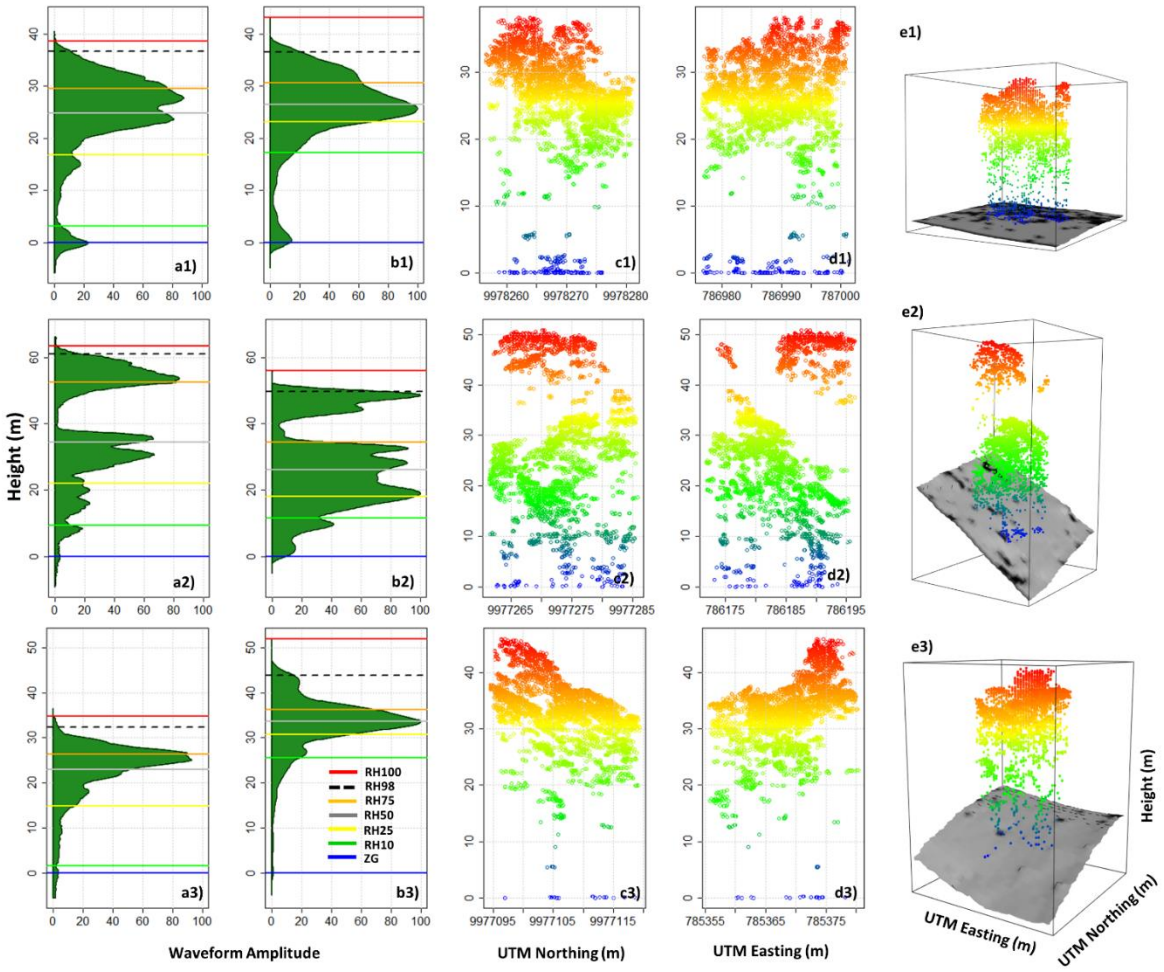

Figure 4.4. Comparison of LF and SF waveforms. LF (a1-a3) and SF (b1-b3) waveforms at footprint level. SF point cloud in 2D (c1-c3; d1-d3) and in 3D (e1-e3). a1-d1 footprint with difference in RH98 of 0.12 m (UTM E: 786989 N: 9978269). a2-d2 with difference in RH98 of 11.32 m (UTM E: 786184 N: 9977274). a3-d3 footprint with difference in RH98 of -11.48 m (UTM E: 785368 N: 9977107). The SF derived pseudo-waveform is smoothed for better display herein.

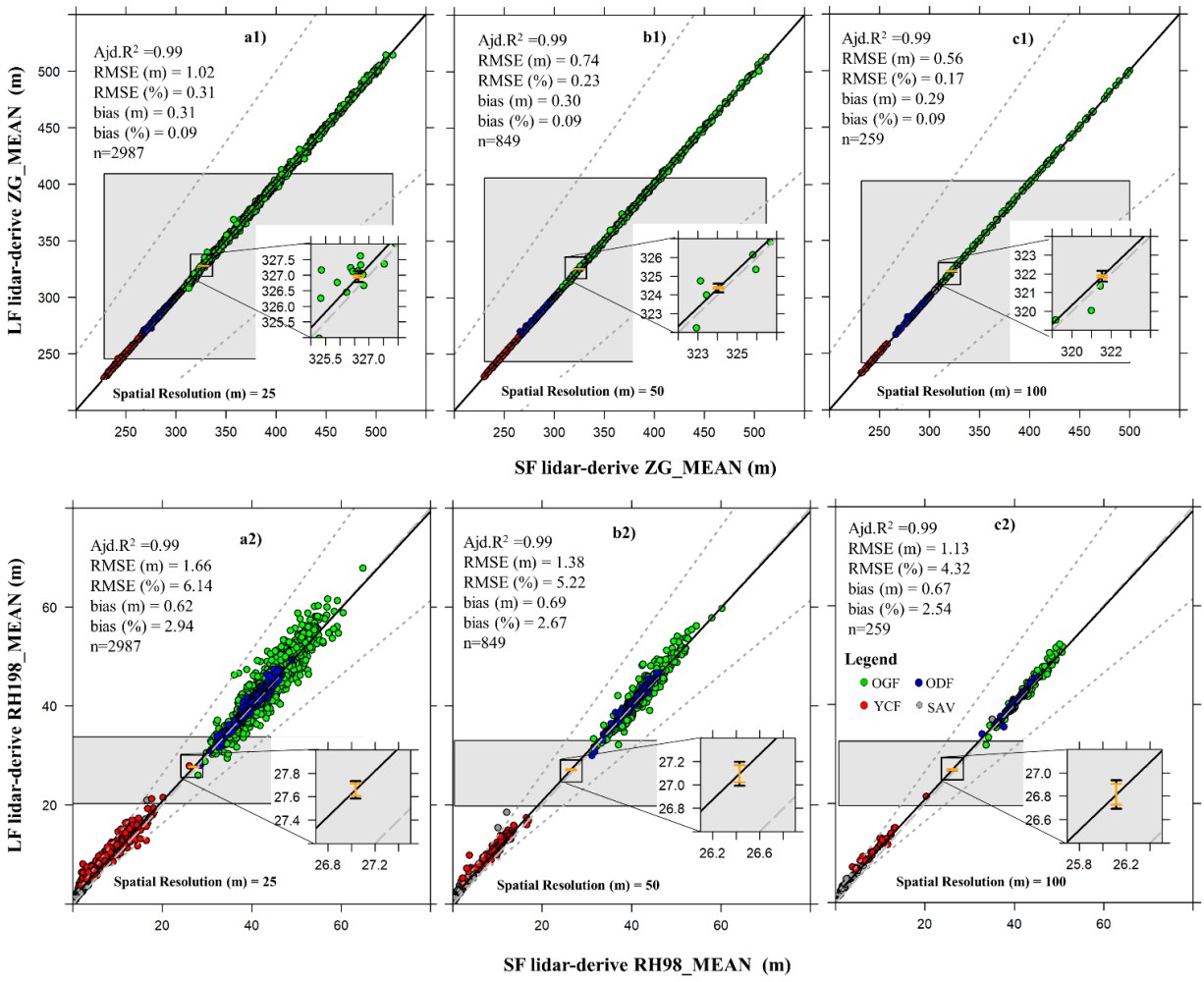

Figure 4.5. Equivalence test of mean ground elevation (ZG_MEAN) (a1-c1) and mean canopy height (RH98_MEAN) (a1-c2) at spatial resolution of 25 (a1-a2), 50 (b1-b2) and 100 m (c1-c2). Mixed old-growth forest (OGF); Monodominant Okoumé forest (ODF); Young colonizing forests of savanna (YCF); and Grassland savanna (SAV);

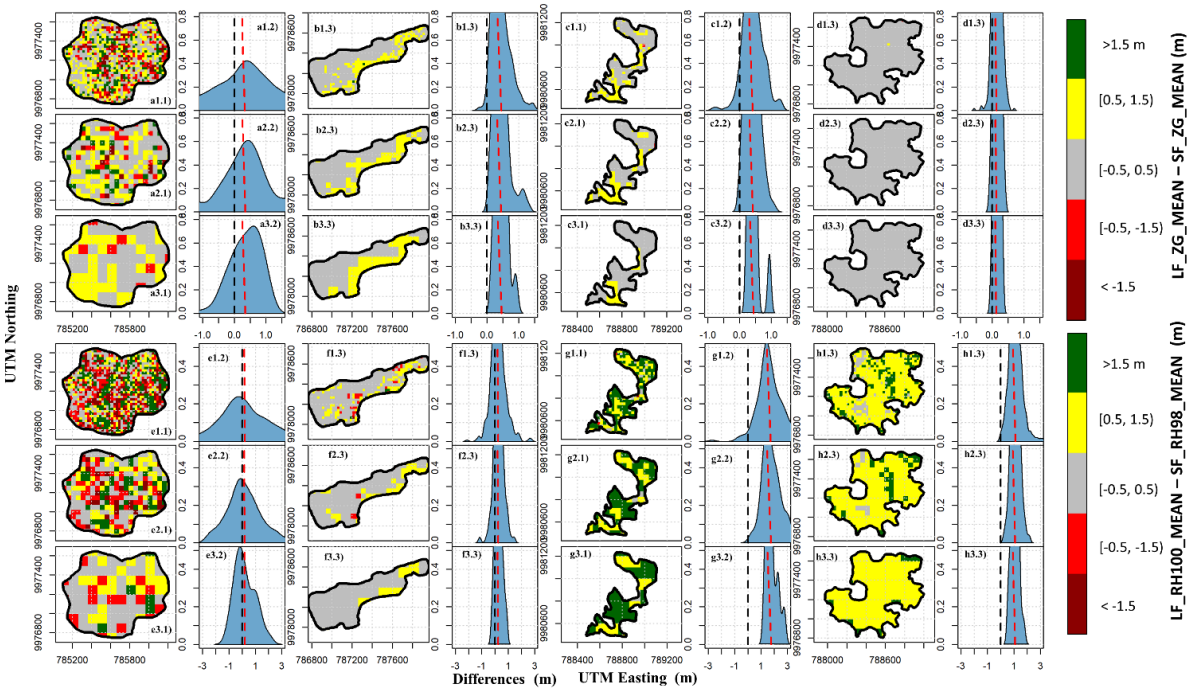

Figure 4.6. Spatial distribution of differences between SF and LF lidar-derived ground elevation (ZG_MEAN) and top-of-canopy height (RH98_MEAN) for different vegetation types and spatial resolutions. We focused on four vegetation types: mixed old-growth forest (OGF; a1.1-a3.2 and e1.1-e3.2); monodominant Okoumé forest (ODF; b1.1-b3.2 and f1.1-f3.2), young colonizing forests of savanna (YCF; c1.1-c3.2 and g1.1-g3.2); and grassland savanna (SAV; d1.1-d3.2 and h1.1-h3.2). Three spatial resolutions were considered: 25 m (a1.1-h1.1), 50 m (a2.1-h2.1), and 100 m (a3.1-h3.1). The blue graphs represent the distribution of differences between SF and LF lidar-derived ZG_MEAN and RH98_MEAN. The black and red dashed lines represent the 0 and mean of difference distribution, respectively.

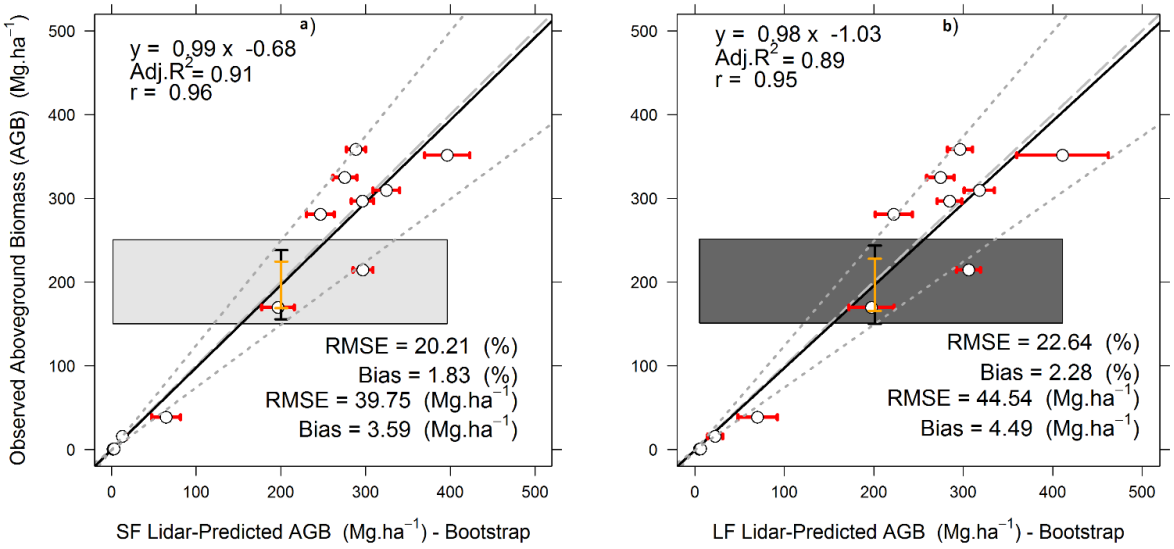

Figure 4.7. Equivalence plots of the observed and predicted AGB (Mg · ha^{-1}) obtained from the 100 bootstrapped model runs using SF_MCH (a) and LF_RH75MEAN (b) (N=12). The white dots are the pairwise measurements, and the solid line is a best-fit linear model for the pairwise measurements. The horizontal red bar is the standard deviation of AGB estimates from the bootstrapping procedure. The light grey dashed line represented the relationship 1:1. N=12

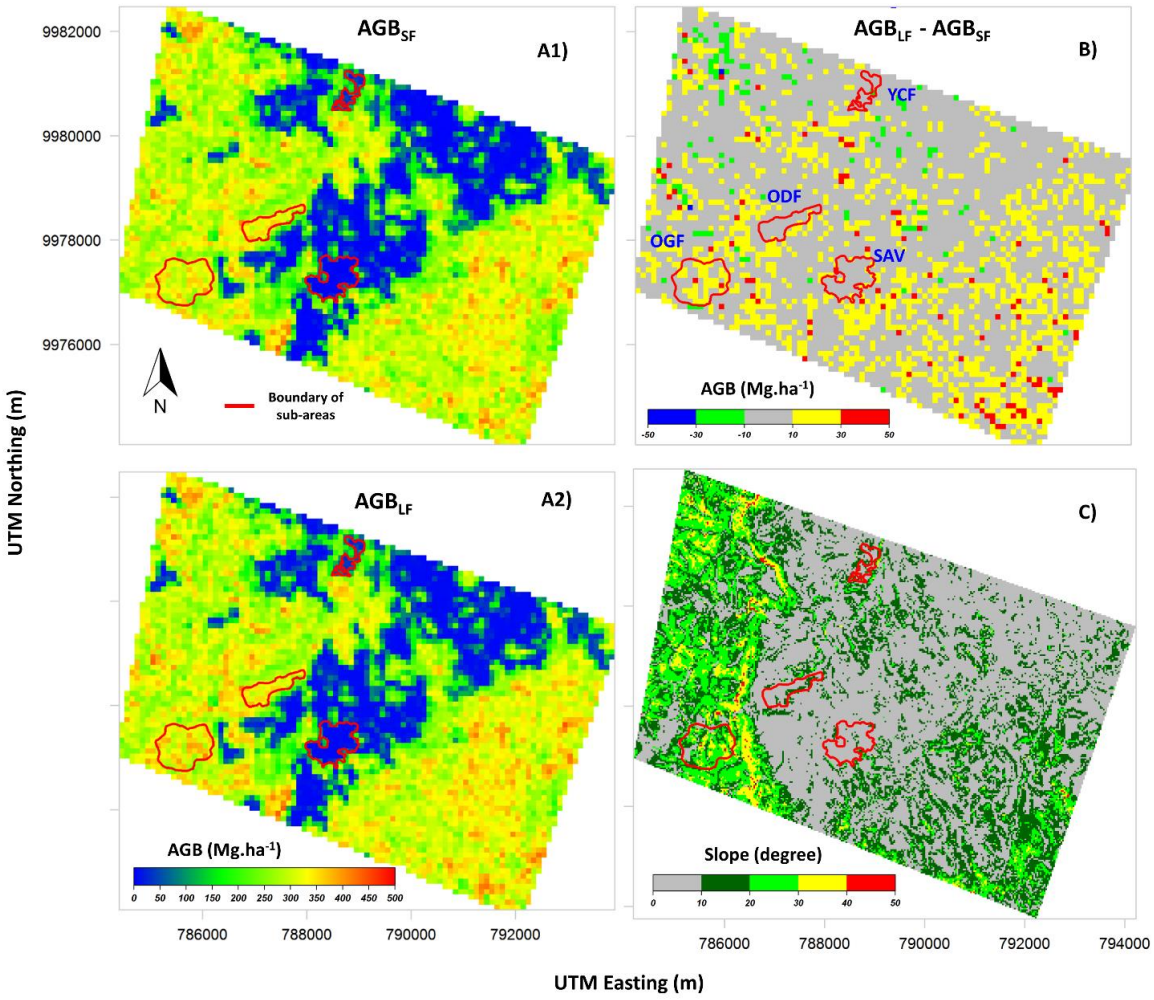

Figure 4.8. Small (a1) and Large (b2) Lidar-footprint derived Aboveground Biomass Estimates at the landscape level. b) The difference in Aboveground Biomass Estimates between SF and LF lidar. (c) slope (degree) map. Mixed old-growth forest (OGF); Monodominant Okoumé forest (ODF); Young colonizing forests of savanna (YCF); and Grassland savanna (SAV).

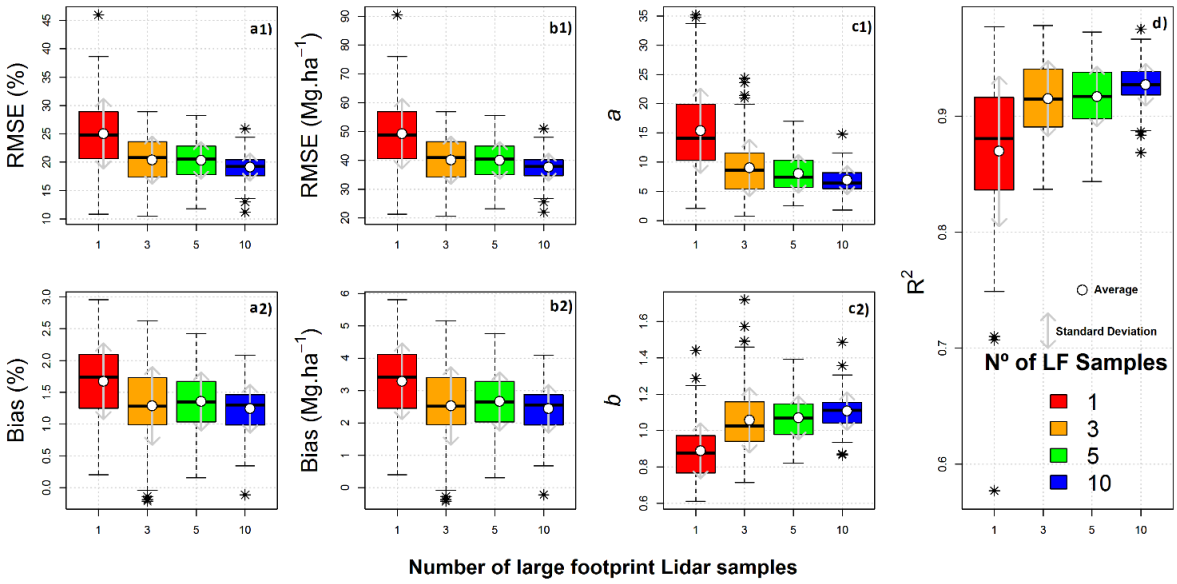

Figure 4.9. LF simulations for AGB modeling at 1-ha. Relative and absolute RMSE and bias (a1-b1; a2-b2). Parameters *a* (c1) and *b* (c2) and R2 (d) of the AGB models.

Conclusion and Future Directions

The research presented in this dissertation contributes significantly to the understanding of how lidar remote sensing can be efficiently applied for predicting and mapping critical forest structural attributes, such as aboveground biomass and volume, at individual tree, plot and landscape levels in both natural forests and industrial forest plantations. Moreover, this dissertation developed a cutting-edge R package for lidar data processing and visualization for forestry applications. Major findings, contributions of this dissertation and future research directions are summarized for each chapter and presented as follows:

In Chapter 1, I developed a novel framework to automatically detect individual trees and evaluate the efficacy of *k*-nearest neighbor (*k*-NN) imputation models for estimating tree attributes in longleaf pine (*Pinus palustris* Mill.) forests. Although basal area estimation accuracy was poor because of the longleaf pine growth habit, individual tree locations, height and volume were estimated with high accuracy, especially in low-canopy-cover conditions; the root mean square distance (RMSD) for tree-level height, basal area, and volume were 2.96%, 58.62%, and 8.19%, respectively. While the methodology developed here shows promising results, further work is needed to refine aspects of the approach to increase accuracy when estimating basal area. Future directions for this research include the combined use of airborne and terrestrial lidar to better describe the structure of individual trees. Besides crown height and crown projected area, additional crown metrics, such as crown volume and surface area, should be computed and tested as new predictors for estimating basal area and other important forest attributres. As Unmanned Aerial Vehicle (UAV) remote sensing technologies and methods improve, there is potential for combining airborne lidar-derived DTM from a previous acquisition with UAV photogrammetry and Structure from Motion (SfM) algorithms for effectively monitoring and mapping forest attributes at the individual tree level in longleaf pine forests in a cost-effective manner.

Chapter 2 presented a framework to predict and map stem total and assortment volumes in industrial *Pinus taeda* L. forest plantations from lidar data and random forest models. The results of this chapter demonstrated that lidar data combined with ramdom

forest models could provide reliable estimates of total, commercial and pulp volumes. For instance, when lidar-dereived estimates of stem volume were compared to reference forest inventory data, the accuracy of plot-level total and assortment volumes were high; the root mean square error (RMSE) of total, commercial and pulp volume estimates were 7.83%, 7.71% and 8.63%, respectively. Accurate estimates of crown attributes at the highest attainable spatial resolution is much desired to increase the efficiency of monitoring and managing *Pinus teada* plantations, therefore future research should focus on estimating forest attribues at the tree level as well. Crown estimates would be highly desired information to assist in common forestry tasks, such as in thinning operations. Also, crown attributes could be used in combination with field data to fit taper models and improve the accuracy of assortment volume estimates. Random forest *k*-NN imputation has been successfully used to predict individual tree height and volume in longleaf pine forest in southeastern USA, as shown in Chapter 1; therefore, lidar and random forest combined into an individual tree framework should be tested to predict stem total and assortment volumes at an individual tree level in *P. taeda* forest plantations as well.

In Chapter 3, the impacts of airborne lidar pulse density on estimating aboveground biomass (AGB) stocks and changes in a selectively logged tropical forest were assessed. The results indicated that estimates of AGB change at the plot level were only slightly affected by pulse density. However, at the landscape level differences in estimated AGB change of >20 $Mg \cdot ha^{-1}$ was observed when pulse density decreased from 12 to 0.2 $pulses \cdot m^{-2}$. The effects of pulse density were more pronounced in areas of steep slope, but when the DTM from high pulse density lidar collected in 2014 was used to derive the forest height from both years, the effects on forest height and the estimated AGB stock and changes did not exceed 20 $Mg \cdot ha^{-1}$. The results of this chapter indicated that AGB change can be monitored in selective logged tropical forests with reasonable accuracy and low cost with low pulse density lidar surveys if a baseline high-quality DTM is available from at least one lidar survey. As forest degradation is one of the most important sources of carbon emissions in the tropics, future research should focus on testing the capability of low pulse density lidar for mapping logging activities with the aim of detecting and measuring forest degradation as well.

Chapter 4 presented a comparison of airborne small-footprint (SF) and large-footprint (LF) lidar retrievals of ground elevation, vegetation height and biomass across a successional tropical forest gradient in central Gabon. The comparison of the two sensors shows that LF lidar waveforms are equivalent to simulated waveforms from SF lidar for retrieving ground elevation (RMSE=0.5 m, bias=0.29 m) and maximum forest height (RMSE=2.99 m; bias=0.24 m). Comparison of gridded LF lidar height with ground plots showed that an unbiased estimate of aboveground biomass at 1-ha can be achieved with a sufficient number of large footprints (> 3). The results of this chapter can be used as the foundation for further research on applying large footpring lidar remote sensing for monitoring and mapping forest structure in tropical forest. Also, the potential for large footprint lidar to estimate forest biomass at the global level will be increased as the Global Ecosystem Dynamics Investigation (GEDI) lidar becomes operational and provides data comparable to existing Land, Vegetation, and Ice Sensor (LVIS) data used in this reseach. Future research should focus on developing and testing new algorithms for detecting ground elevation in a variety of canopy structure and topography conditions, because ground detection is one of the major sources of error when using large footprint lidar-derived metrics to retrieve forest structure and AGB stocks in tropical forest. Moreover, as other upcoming NASA missions, such as National Aeronautics and Space Administration-Indian Space Research Organization Synthetic Aperture Radar (NISAR) and Ice, Cloud and land Elevation Satellite (ICESat - 2) sensors will be soon collecting data sensitive to forest structure, future research should focus on developing and testing multi-sensor data fusion approaches in advance of these missions.

The research presented in this dissertation was carried out in natural and industrial forest plantations located in Brazil, the United States and Gabon. However, the framework and tools developed and presented herein can serve as useful methodologies for application worldwide. I therefore hope that the promising results presented and discussed here will stimulate further research and applications of lidar remote sensing not just in these mentioned countries, but elsewhere as well.

Appendix A. rLiDAR: An R package for reading, processing and visualizing lidar data

Silva, C.A., Crookston, N.L., Hudak, A.T., and Vierling, L. A. 2017. rLiDAR: An R package for reading, processing and visualizing lidar (Light Detection and Ranging) data, version 0.1, accessed Oct. 15 2017, < http://cran.r-roject.org/web/packages/rLiDAR/index.html>.

The R package rLiDAR is an open-source tool for reading, processing and visualizing small sets of airborne lidar data. It was developed in 2014, as part of this Ph.D. dissertation, and made publicly available on the Comprehensive R Archive Network (CRAN) in 2015. The rLiDAR package presents eight functions that allow ecologists, forest managers and scientists to i) import and visualize lidar data (e.g. Figure A1a); ii) smooth, detect and delineate individual trees on the lidar-derived canopy height model (e.g., Figure A1b-d), iii) compute lidar metrics at plot and crown levels (e.g., Figure A1d-g), and iv) plot virtual forest stands (e.g., Figure A1h1-h3). Since we developed the rLiDAR, additional open-source R packages for lidar data processing and visualization have been developed, such as lidR (Roussel et al. 2017) and ForestTools (Plowright 2017). rLiDAR was specifically developed to support the analysis presented in the Chapter 1 of this dissertation, with the goal of providing and testing a new framework for imputing individual tree attributes from field and lidar data in longleaf pine forests. However, the rLiDAR has general applicability to other forests in other ecosystems, and we encourage users to test it broadly.

References

Roussel, J.R, Auty, D., Boissieu., Florian De, and Meador, A. S. 2018. lidR: Airborne LiDAR Data Manipulation and Visualization for Forestry Applications, version 1.4.1, accessed Fev. 15 2018, < https://cran.r-project.org/web/packages/lidR/index.html >.

Plowright, A. ForestTools: Analyzing Remotely Sensed Forest Data, version 0.1.5, accessed Oct. 15 2017, < https://cran.r-project.org/web/packages/ForestTools/index.html>.

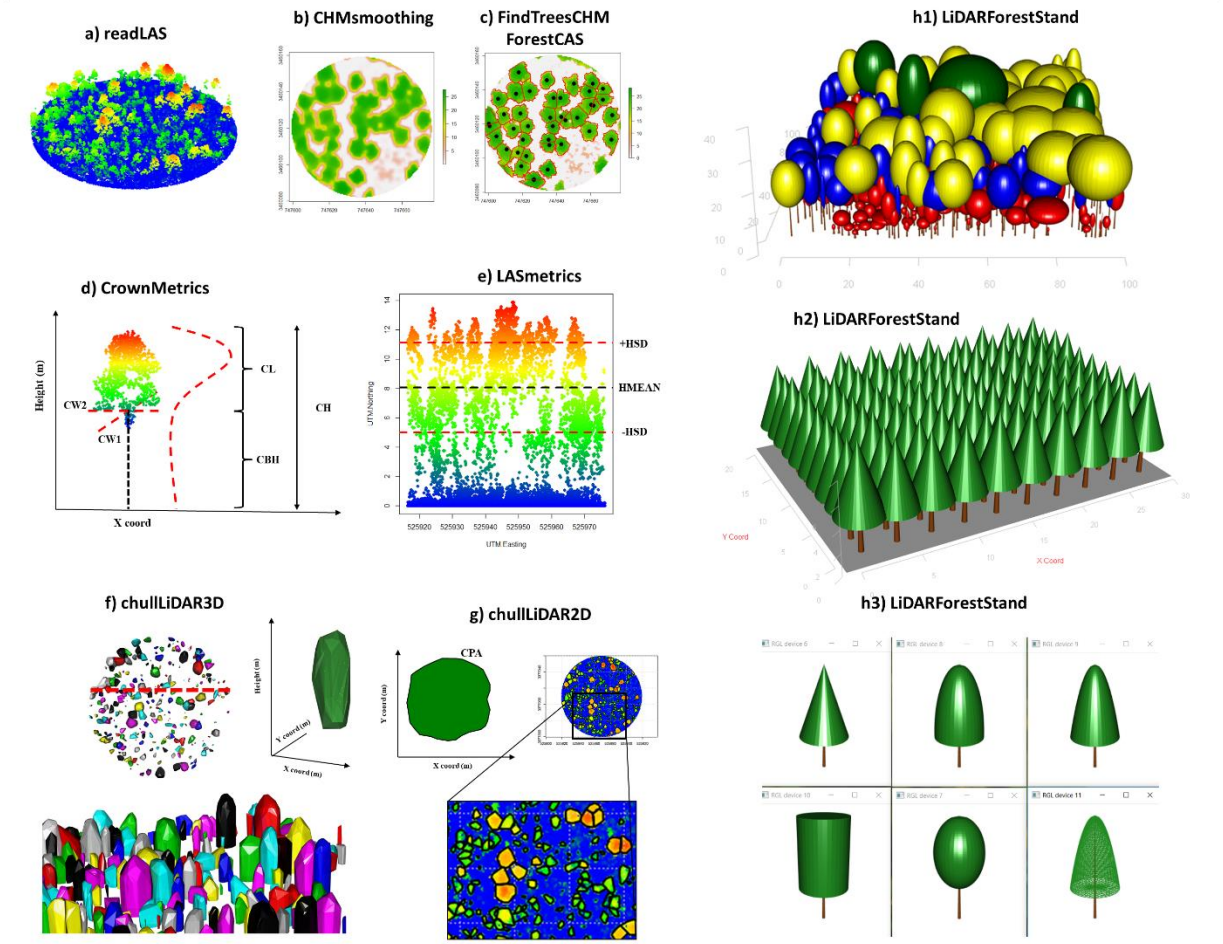

Figure A1. Figure A1. rLiDAR: An R package for reading, processing and visualizing lidar data

Appendix B. Copyright Statements - MDPI Open Access Information and Policy Remote Sensing

All articles published by MDPI are made immediately available worldwide under an open access license. This means: ϖ everyone has free and unlimited access to the full-text of all articles published in MDPI journals, and ϖ everyone is free to re-use the published material if proper accreditation/citation of the original publication is given. ϖ open access publication is supported by the authors' institutes or research funding agencies by payment of a comparatively low Article Processing Charge (APC) for accepted articles

Appendix C. Copyright Statements - Taylor & Francis

Taylor & Francis
Taylor & Francis Group

Our Ref: JB/UJRS/P18/0088

11TH January 2018

Dear Carlos A. Silva

Thank you for your correspondence requesting permission to reproduce the following article published in our journal in your printed thesis and to be posted in your university's repository at the University of Idaho.

MATERIAL REQUESTED: 'Imputation of Individual Longleaf Pine (Pinus palustris Mill.) Tree Attributes from Field and LiDAR Data' by Carlos A. Silva, Andrew T. Hudak, Lee A. Vierling, E. Louise Loudermilk, Joseph J. O'Brien, J. Kevin Hiers, Steve B. Jack, Carlos Gonzalez-Benecke, Heezin Lee, Michael J. Falkowski & Anahita Khosravipour *Canadian Journal of Remote Sensing* Vol 42:5 pp. 554-573 (2016).

We will be pleased to grant permission on the sole condition that you acknowledge the original source of publication and insert a reference to the article on the Journals website:

This is the authors accepted manuscript of an article published as the version of record in Canadian Journal of Remote Sensing on 11th July 2016. http://www.tandfonline.com/ https://doi.org/10.1080/07038992.2016.1196582

Please note that this license does not allow you to post our content on any third-party websites or repositories.

Thank you for your interest in our Journal.

Yours sincerely

Jo Bateman – Permissions Administrator, Journals
Taylor & Francis Group
3 Park Square, Milton Park, Abingdon, Oxon, OX14 4RN, UK.
Tel: +44 (0)20 7017 7617
Fax: +44 (0)20 7017 6336
Web: www.tandfonline.com
e-mail: joanne.bateman@tandf.co.uk

2&4 Park Square, Milton Park, Abingdon, Oxfordshire OX14 4RN
Tel: +44 (0) 20 7017 6000; Fax: +44 (0) 20 7017 6336

www.tandf.co.uk

Registered in England and Wales. Registered Number: 1072954
Registered Office: 5 Howick Place, London, SW10 1WG

an informa business